

Investigations Into Time-Resolved Secretory Protein Quality Control Dynamics

By

Madison Taylor Wright

Dissertation Submitted to the  
Faculty of the  
Graduate School of Vanderbilt University

In partial fulfillment of the requirements

for the degree of

DOCTOR OF PHILOSOPHY

in

Chemistry

December 17<sup>th</sup>, 2022

Nashville, Tennessee

Approved:

Lars Plate, PhD

Renã A. S. Robinson, PhD

Charles Sanders, PhD

Lauren Buchanan, PhD

Copyright © 2022 Madison Taylor Wright

All Rights Reserved

## DEDICATION

To my wife, friends, family and Lord and Savior Jesus Christ, I may have earned this  
PhD myself, but this is ours to share.

## ACKNOWLEDGEMENTS

Without stating the obvious, this work does not exist without the support from my advisor, Dr. Lars Plate. I am thankful for you taking a chance on me, and your suppleness in your mentorship, from rubbing elbows during the early days of my training to allowing me to drive the bus on this project.

Next, I would like to thank my advisors and mentors at Jacksonville State University and The University of Alabama at Birmingham including Dr. Jan Gryko, Dr. Nixon Mwebi, Dr. Brent Helms, and Dr. Sooryanarayana Varambally. Without their guidance during my undergraduate studies, I would not be here today. Dr. Helms ensured I was on track academically, while Dr. Gryko, Dr. Mwebi, and Dr. Varambally introduced me into the world of basic research that has led me to this point.

I am grateful to my committee members for their oversight and guidance in my thesis project and overall growth as a scientist.

I thank Dr. Renã A. S. Robinson and her group for their guidance and access to mass spectrometry resources early in my graduate career. They were pivotal in getting me off the ground with my project.

Many thanks are due to all the scientists I had the opportunity of collaborating with during my time at Vanderbilt. While your work may not make it into my dissertation, I have

learned something from each and every collaboration and side project taken on during my time here.

I would like to thank my sources of funding. I have been supported through multiple grants and fellowships throughout my time at Vanderbilt University including The Vanderbilt Institute of Chemical Biology Research Fellowship, National Institute of General Medical Sciences Chemistry-Biology Interface Training Grant (5T32GM065086-04), National Science Foundation Graduate Research Fellowship Training Program, and National Institute of General Medical Sciences (1R35GM133552).

Finally, I would like to thank my friends, family, and loved ones for their continuous support throughout my scientific career. I thank my parents for continuously supporting me throughout my endeavors while simultaneously having no idea what it is I actually do on a day-to-day basis. A big thank you to my longtime friends the Gingersnaps and Jacksonville State University drumline brotherhood for many years of fellowship and support. A thank you is also well deserved for my chemistry department friends Bailey S. Rose and Nadjali Chung for their support throughout these past 5 years. I owe the biggest thank you to my wife Sydney Jones-Wright as she has stood by my side for 10+ years as my best friend, my biggest support system, and my rock as I have molded into the person I am today.

## TABLE OF CONTENTS

<b>DEDICATION</b> .....	<b>III</b>
<b>ACKNOWLEDGEMENTS</b> .....	<b>IV</b>
<b>LIST OF FIGURES</b> .....	<b>IX</b>
<b>LIST OF ABBREVIATIONS</b> .....	<b>XI</b>
<b>REVEALING FUNCTIONAL INSIGHTS INTO ER PROTEOSTASIS THROUGH PROTEOMICS AND INTERACTOMICS</b> .....	<b>1</b>
1.1 DYNAMICS OF SECRETORY PROTEOSTASIS .....	1
1.2 PROTEOMICS AND INTERACTOMICS TO INVESTIGATE PROTEOSTASIS.....	5
1.3 PROTEOSTASIS NETWORK-CENTRIC INVESTIGATIONS .....	7
1.3.1 <i>ER chaperoning complexes</i> .....	8
1.3.2 <i>ER membrane complex and transmembrane proteins</i> .....	11
1.3.3 <i>ER-associated degradation (ERAD) and ER-phagy</i> .....	12
1.3.4 <i>Adapting ER proteostasis through the Unfolded Protein Response</i> .....	15
1.4 CLIENT-CENTRIC INVESTIGATIONS.....	17
1.4.1 <i>Loss-of-function protein misfolding diseases</i> .....	18
1.4.2 <i>Protein aggregation diseases</i> .....	20
1.4.3 <i>Viral proteostasis clients</i> .....	22
1.5 FUTURE DIRECTIONS AND SCOPE OF DISSERTATION.....	25
1.5.1 <i>Scope of Dissertation</i> .....	26
1.6 REFERENCES.....	27
<b>INTERACTOME PROFILING DEFINES ALTERED PROTEOSTASIS TOPOLOGY ASSOCIATED WITH THYROID DYSHORMONOGENESIS</b> .....	<b>34</b>
2.1 THE PATHOLOGY OF TG-RELATED CONGENITAL HYPOTHYROIDISM.....	34
2.2 DISTINCT THYROGLOBULIN MUTANTS PRESENT COMMON SECRETION DEFECTS .....	37
2.3 DEFINING THE TG PROTEOSTASIS INTERACTOME.....	40
2.4 SECRETION DEFECTS OF TG MUTANTS ARE ASSOCIATED WITH COMMON INCREASES IN PROTEOSTASIS INTERACTIONS.....	43
2.5 CH-ASSOCIATED TG EXHIBITS MUTATION SPECIFIC CHANGES IN ENGAGEMENT WITH THE ER-LECTION CHAPERONE NETWORK .....	47
2.6 PERTURBATION OF N-LINKED GLYCOSYLATION DISTINCTLY IMPACTS A2234D TG.....	50
2.7 DISCUSSION AND CONCLUSIONS.....	52
2.8 ACKNOWLEDGEMENTS .....	58
2.9 EXPERIMENTAL METHODS.....	59
2.9.1 <i>Plasmids and Antibodies</i> .....	59
2.9.2 <i>Cell Culture and Transfections</i> .....	60
2.9.3 <i>Affinity Purification and MS Sample Preparation</i> .....	61
2.9.4 <i>Liquid Chromatography – Tandem Mass Spectrometry</i> .....	62
2.9.5 <i>Experimental Design and Statistical Rationale</i> .....	64
2.9.6 <i>Immunoblotting, SDS-PAGE, and Immunoprecipitation</i> .....	66

2.9.7 Cycloheximide Chase Assay .....	67
2.9.8 <sup>35</sup> S Pulse Chase Assay.....	67
2.9.9 EndoH and PNGaseF Treatment.....	68
2.10 REFERENCES.....	69
<b>TIME-RESOLVED INTERACTOME PROFILING DECONVOLUTES PROTEIN</b>	
<b>QUALITY CONTROL DYNAMICS .....</b>	<b>75</b>
3.1 INTRODUCTION.....	75
3.2 TRIP TEMPORALLY RESOLVES TG INTERACTIONS WITH PQC COMPONENTS .....	78
3.3 TRIP IDENTIFIES ALTERED TEMPORAL DYNAMICS ASSOCIATED WITH TG PROCESSING...	82
3.4 DISCUSSION AND CONCLUSIONS.....	89
3.5 ACKNOWLEDGEMENTS.....	91
3.6 EXPERIMENTAL METHODS.....	91
3.6.1 Plasmid Production and Antibodies .....	92
3.6.2 Cell Line Engineering.....	92
3.6.3 Time-Resolved Interactome Profiling.....	92
3.6.4 Liquid Chromatography – Tandem Mass Spectrometry .....	95
3.6.5 Immunoblotting and SDS-PAGE.....	96
3.6.6 Mass Spectrometry Interactomics and TMT Quantification .....	97
3.6.7 Data and Code Availability.....	98
3.7 REFERENCES.....	98
<b>INVESTIGATING THE FUNCTIONAL IMPLICATIONS OF PROTEIN QUALITY</b>	
<b>CONTROL COMPONENTS ON THYROGLOBULIN PROCESSING .....</b>	<b>104</b>
4.1 INTRODUCTION.....	104
4.2 siRNA SCREENING DECONVOLUTES INTERACTIONS AND KEY REGULATORS OF	
CONSTRUCT SPECIFIC TG PROCESSING.....	106
4.3 TRAFFICKING AND DEGRADATION FACTORS SELECTIVELY REGULATE TG PROCESSING IN	
THYROID CELLS.....	110
4.4 PHARMACOLOGICAL VCP INHIBITION SELECTIVELY RESCUES C1264R TG SECRETION	
.....	113
4.5 PHARMACOLOGICAL VCP INHIBITION IS ASSOCIATED WITH TEMPORAL REMODELING OF	
THE TG INTERACTOME .....	114
4.6 MUTANT TG IS SELECTIVELY ENRICHED WITH THE ER-PHAGY RECEPTOR TEX264....	117
4.7 DISCUSSION AND CONCLUSIONS.....	119
4.8 ACKNOWLEDGEMENTS .....	121
4.9 EXPERIMENTAL METHODS.....	122
4.9.1 Plasmid Production and Antibodies .....	122
4.9.2 Cell Line Engineering.....	122
4.9.3 Immunoblotting and SDS-PAGE.....	123
4.9.4 qRT-PCR .....	124
4.9.5 siRNA Screening Assay.....	125
4.9.6 FRT siRNA Validation Studies .....	125
4.9.7 <sup>35</sup> S Pulse Chase Assay.....	126
4.9.8 VCP Pharmacological Inhibition Studies.....	127

4.9.9 <i>TEX264 &amp; Tg-NLuc Co-Immunoprecipitation Studies</i> .....	128
4.9.10 <i>Mass Spectrometry Interactomics and TMT Quantification</i> .....	129
4.9.11 <i>Data and Code Availability</i> .....	130
4.10 REFERENCES.....	130
<b>CONCLUSIONS AND FUTURE DIRECTIONS</b> .....	<b>134</b>
REFERENCES.....	139
<b>APPENDIX</b> .....	<b>142</b>
SUPPLEMENTARY MATERIALS FOR CHAPTER 2.....	143
SUPPLEMENTARY MATERIALS FOR CHAPTER 3.....	162
SUPPLEMENTARY MATERIALS FOR CHAPTER 4.....	172
CURRICULUM VITAE .....	182



## LIST OF FIGURES

Figure 1.1: Secretory proteostasis and protein quality control is governed by the activity of ER protein folding, trafficking, and degradation pathways .....	2
Figure 1.2: ER protein quality control capacity is monitored by the three branches of the unfolded protein response.....	4
Figure 1.3: Affinity purification – mass spectrometry and tool compounds to elucidate protein-protein interactions.....	6
Figure 2.1: Distinct Tg mutants present secretion defects .....	38
Figure 2.2: Defining the Tg interactome using multiplexed quantitative AP-MS .....	42
Figure 2.3: The secretion defect of Tg mutants is associated with both common and mutant specific changes in proteostasis interactions .....	44
Figure 2.4: Tg mutants are increasingly routed towards ER-associated degradation machineries but not degraded at faster rates.....	46
Figure 2.5: Perturbation of N-linked glycosylation distinctly impacts A2234D Tg .....	49
Figure 2.6: Model for common and mutant-specific proteostasis interactome changes mediating the secretion defect of CH-associated Tg variants.....	54
Figure 3.1: Time-Resolved Interactome Profiling to Identify Interactions with Newly Synthesized Proteins .....	79
Figure 3.2: TRIP Temporally Resolves Tg Interactions with Protein Quality Control Components.....	81
Figure 3.3: TRIP Identifies Altered Temporal Dynamics Associated with Tg Processing .....	84
Figure 4.1: siRNA Screening Deconvolutes Interactions and Key Regulators of Construct Specific Tg Processing .....	108
Figure 4.2: Trafficking and Degradation Factors Selectively Regulate Tg Processing in FRT cells .....	111
Figure 4.3: Pharmacological VCP Inhibition Selectively Rescue C1264R Tg Secretion and is Associated with Interactome Remodeling .....	116

Figure 4.4: Mutant Tg is Selectively Enriched with the ER-phagy Receptor TEX264.. 118

## LIST OF ABBREVIATIONS

<b>Term</b>	<b>Definition</b>
CANX	calnexin
AL	light chain amyloidosis
APEX	ascorbic acid peroxidase
ATF6	activating transcription factor 6
ATL3	alastin GTPase 3
BONCAT	biorthogonal non-canonical amino acid tagging
CALR	calreticulin
CCDC47	coiled-coil domain containing 47
CCPG1	cell cycle progression 1
CF	cystic fibrosis
CFTR	cystic fibrosis transmembrane conductance regulator
CH	congenital hypothyroidism
ChEL	cholinesterase-like domain
CHIP	C-terminus of Hsc70-interacting protein
CHX	cycloheximide
COVID-19	coronavirus disease 19
CRISPR	clustered regularly interspaced short palindromic repeats
CTSZ	cathepsin z
Cu-AAC	copper-catalyzed azide-alkyne cycloaddition
DDOST	dolichyl-diphosphooligosaccharide--protein glycosyltransferase non-catalytic subunit
DENV	denguevirus
DER1	derlin 1
DNAJB11	DnaJ heat shock protein family member B11
DNAJC10	DnaJ heat shock protein family member C10
DNAJC3	DnaJ heat shock protein family member C3
DSP	dithiobis(succinimidyl propionate)
EDEM	ER degradation enhancing alpha-mannosidase
EMC	ER membrane protein complex
EndoH	endoglycosidase H
ER	endoplasmic reticulum
ER-MAP	ER membrane yeast two-hybrid system and affinity purification
ER-phagy	autophagy of the ER
ERAD	ER-associated degradation
ERLAD	ER to lysosome-associated degradation
FAF2	fas associated factor family member 2
FIP200	FAK family kinase-interacting protein of 200 kDa

FOXRED2	RAD-dependent oxidoreductase domain containing 2
FRT	Fischer rat thyroid
GABA	gamma aminobutyric acid
GABARAP	GAMBA type a receptor-associated protein
GANAB	glucosidase II alpha subunit
GO	gene ontology
GUSB	glucuronidase beta
HERP	HRD1-associated membrane protein
HERPUD1	homocysteine inducible ER protein with ubiquitin like domain 1
HILAQ	heavy isotope labeled azidohomoalanine quantification
HRD1	E3 ubiquitin ligase HRD1
Hsp70/40	heat shock protein 70 kDa and 40 kDa chaperone/co-chaperone system
Hsp90	heat shock protein 90
HSP90B1	heat shock protein 90 beta family member 1
HSPA5	heat shock protein family A (Hsp70) member 5
HYOU1	hypoxia up-regulated 1
IO	osteogenesis imperfecta
iPOND	isolation of proteins on nascent DNA
IRE1	ER transmembrane proteins inositol-required enzyme 1
Jem1	DnaJ-like protein of the ER membrane - yeast
JNK	c-Jun N-terminal kinase
LC	light-chain
LC-MS/MS	liquid chromatography - tandem mass spectrometry
LMAN1	lectin mannose binding 1
LUMIER	Luminescence-based Mammalian IntERactome
MAN1B1	mannosidase alpha class 1B member 1
MLEC	malectin
N-glycosylation	asparagine-linked protein glycosylation
NAPA	NSF attachment protein alpha
NCLN	nicalin
NCSTN	nicastrin
NOMO	NODAL modulator
NPLOC4	NPL4 homolog ubiquitin recognition factor
OS9	OS9 endoplasmic reticulum lectin
OST	oligosaccharyl transferase complex
PALM	pulsed azidohomoalanine labeling in mammals
PDIA3	protein disulfide isomerase family A member 3
PDIA4	protein disulfide isomerase family A member 4
PDIA6	protein disulfide isomerase family A member 6

PDIA9	protein disulfide isomerase family A member 9
PERK	protein kinase R-like ER kinase
PGRMC1	progesterone receptor membrane component 1
PN	proteostasis network
PPIB	peptidylprolyl isomerase B
PQC	protein quality control
PTM	post-translation modification
RCN1	reticulocalbin 1
RNF26	ring finger protein 26
RTN	reticulum
SAHA	suberoylanilide hydroxamic acid
SARS-CoV-2	Severe acute respiratory syndrome coronavirus 2
SDF2L1	stromal cell derived factor 2 like 1
SDS-PAGE	sodium dodecyl sulfate - polyacrylamide gel electrophoresis
SEC62	preprotein translocation factor - homolog SEC62
SEC63	preprotein translocation factor - homolog SEC63
SEL1L	SEL1L adaptor subunit of ERAD E3 ubiquitin ligase
SGD	<i>Saccharomyces</i> Genome Database
SILAC	stable isotope labeling using amino acids in cell culture
SPC	signal peptidase complex
SRPR	signal recognition particle receptor
STING	stimulator of interferon gene
STT3A	oligosaccharyl transferase complex catalytic subunit A
STT3B	oligosaccharyl transferase complex catalytic subunit B
T3	triiodothyronine
T4	thyroxine
TAMRA	tetramethylrhodamine
TEX264	testis expressed 264 - ER-phagy receptor
Tg	thyroglobulin
TMT	tandem mass tags
TRAF2	TNF receptor associated factor 2
TRIP	time-resolved interactome profiling
TUX-MS	thiouracil crosslinking mass spectrometry
UBE2G2	ubiquitin conjugating enzyme E2 G2
UGGT1	UDP-glucose glycoprotein glucosyltransferase 1
UPR	unfolded protein response
UPS	ubiquitin proteasome system
VCP	vasolin containing protein
VIR-CLASP	viral cross-linking and solid-phase purification
XBP1(s)	X-box binding protein1 (splice)

ZIKV

zika virus

## Chapter 1

# **Revealing Functional Insights into ER Proteostasis through Proteomics and Interactomics\***

### **1.1 Dynamics of Secretory Proteostasis**

Secretory proteins routed to the endoplasmic reticulum (ER), lysosome, plasma membrane, or extracellular milieu are first folded and processed within the ER<sup>1</sup>. Such proteins account for approximately one third of the proteome. These proteins include prohormones, receptors, and protein transporters amongst others, and are involved in diverse biological processes including signal transduction, protein degradation, cell growth, and metabolism<sup>1</sup>. In the ER, these “clients” encounter sets of chaperones, co-chaperones, folding enzymes, trafficking, and degradation factors that comprise the ER protein homeostasis (proteostasis) network (ER-PN). The ER-PN ensures the trafficking and localization of properly folded clients, while degrading improperly folded, potentially detrimental clients. This process is cumulatively referred to as protein quality control (PQC). PQC requires coordinated and dynamic interactions of client proteins with ER-PN

---

\* This chapter contains material adapted from the published research article: “Revealing functional insights into ER proteostasis through proteomics and interactomics” by Madison T. Wright, & Lars Plate, *Experimental Cell Research* Volume 399, Issue 1, 2021. It has been reproduced with the permission of the publisher and co-authors.

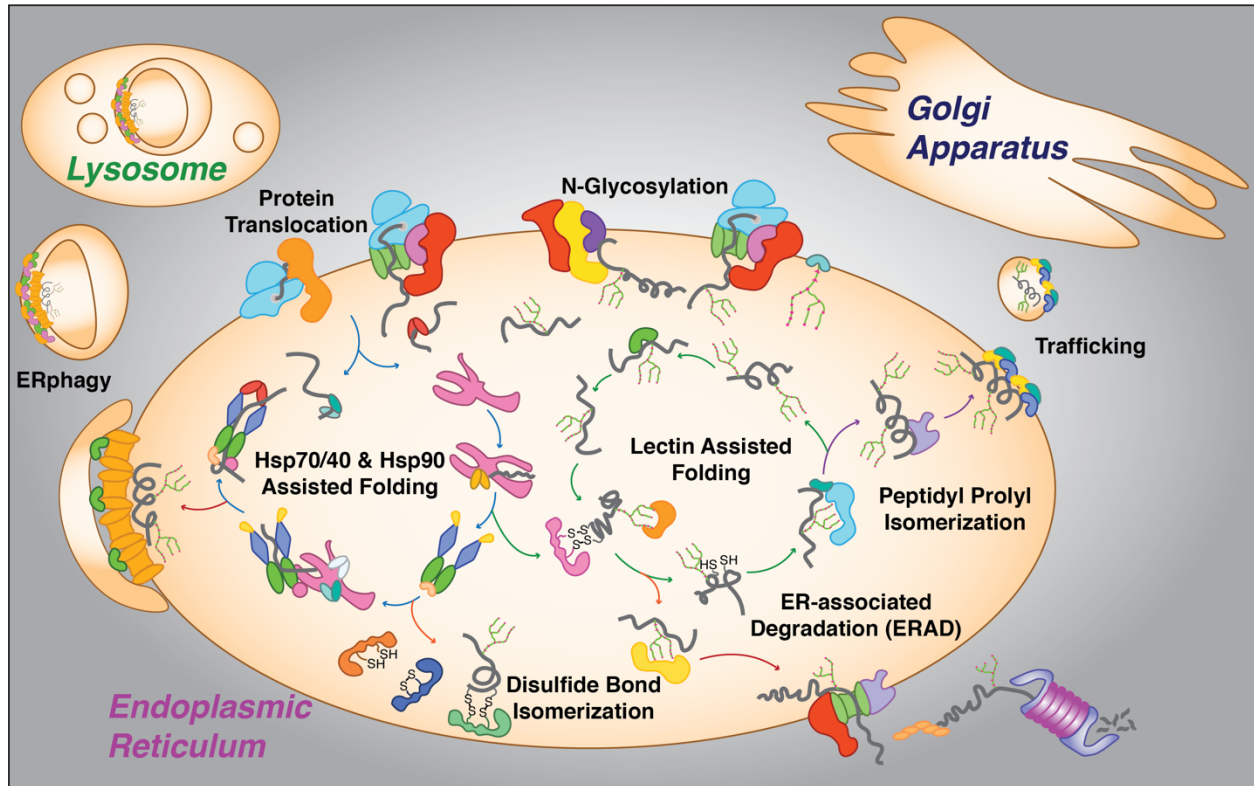


**Figure 1.1: Secretory proteostasis and protein quality control is governed by the activity of ER protein folding, trafficking, and degradation pathways**

Proteins routed for secretory environments cotranslationally enter the ER and engage ER-specific Hsp70/40 and Hsp90 chaperones that aid in client protein folding. Additionally, other folding factors or enzymes such as PDIs, PPIs, and lectin-specific chaperones, may aid in this process. Upon reaching a properly folded confirmation, client proteins are packaged and targeted towards secretory environments through engagement with vesicle trafficking machinery. Client proteins unable to reach their proper conformation are routed towards degradation pathways such ERAD or autophagy (ER-phagy or ERLAD) where clients are degraded by the ubiquitin proteasome system (UPS) or lysosome respectively.

components<sup>1,2</sup>. Polypeptide chains emerging from the ribosome require co-translational engagement with the SEC61 translocon complex to facilitate ER translocation<sup>3,4</sup>. Once the polypeptide chain emerges into the ER, dedicated chaperones such as Hsp70/40s engage with the nascent polypeptide chain until the full protein is translated<sup>5-7</sup>. Post-translational modifications (PTMs), such as glycosylation, later in the folding process can trigger interactions of dedicated chaperones that aid in client-specific processing<sup>8-10</sup>.



Proteins found to reach their properly folded conformation are routed by trafficking factors, such as vesicle coat and packaging machinery, to the proper cellular loci<sup>11</sup>. Conversely, destabilized and therefore potentially detrimental proteins are routed toward degradation pathways requiring dedicated ER-associated degradation (ERAD) or autophagy (ER-phagy) components<sup>12-14</sup> (Figure 1.1).

Insults to the processing of these ER clients or to the ER itself either through genetic, age-related, or environmental perturbations result in imbalances in ER PQC capacity that are linked to several disease states including diabetes, neurodegeneration, amyloidosis, and even cancer<sup>15</sup>. Imbalances in ER PQC capacity can lead to the accumulation of non-native protein species that increase protein folding load and result in ER stress. The protein folding load and status of the ER is constantly monitored by the evolutionarily conserved unfolded protein response (UPR), which consists of three signaling branches regulated by the ER transmembrane proteins inositol-required enzyme 1 (IRE1), activating transcription factor 6 (ATF6), and protein kinase R-like ER kinase (PERK)<sup>16</sup>. When ER stress is encountered, the UPR is activated to adjust protein folding capacity and restore proteostasis [Figure 1.2]. Activation of these branches leads to transcriptional up-regulation of functionally diverse and overlapping gene targets that restore ER proteostasis. These gene targets include ER chaperones, redox enzymes, degradation components and proteins involved in lipid synthesis pathways<sup>17-19</sup>. Additionally, the PERK branch of the UPR transiently inhibits translation to decrease protein folding load. Mechanisms of the UPR and its gene targets have been reviewed in depth previously<sup>16,17</sup>.

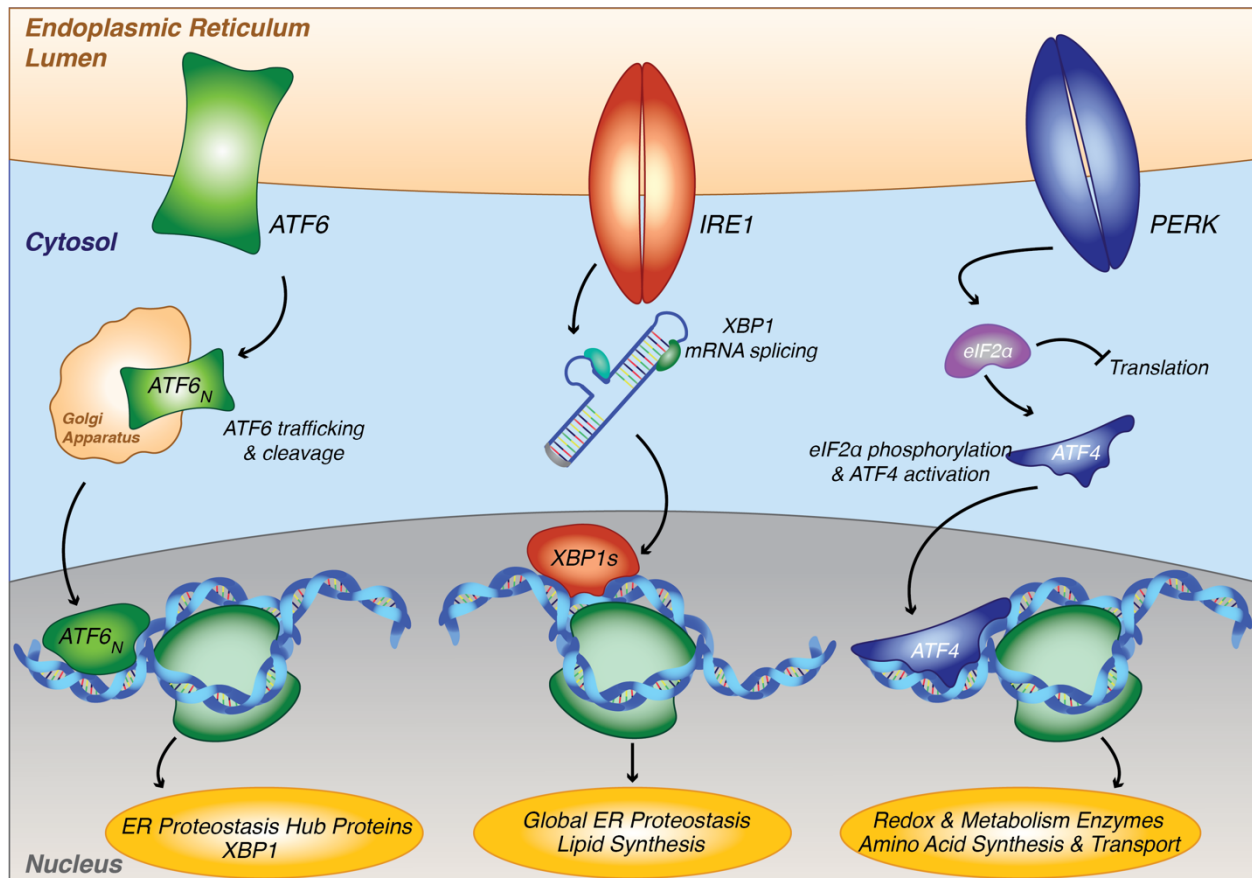


**Figure 1.2: ER protein quality control capacity is monitored by the three branches of the unfolded protein response**

The UPR is regulated by three signaling branches consisting of IRE1, ATF6, and PERK. ER stress leads to PERK activation through dimerization and autophosphorylation, followed by eIF2 $\alpha$  phosphorylation by PERK. Phosphorylation of eIF2 $\alpha$  leads to transient attenuation of protein translation, along with activation of transcription factor ATF4, which transcriptionally upregulates UPR target genes. IRE1 similarly undergoes autophosphorylation and dimerization, which results in splicing of the XBP1 mRNA transcript and the translation of the active XBP1s transcription factor. XBP1s then goes on to upregulate UPR target genes. ATF6 activation by ER stress leads to ATF6 trafficking to the Golgi apparatus, where ATF6 is proteolytically processed to release an active ATF6 transcription factor that can translocate to the nucleus and upregulate UPR gene targets.

## 1.2 Proteomics and Interactomics to Investigate Proteostasis

Mass spectrometry (MS) has become a key technology to characterize changes in protein expression as a result of ER stress and UPR regulations. MS has enabled the identification of protein-protein interactions that facilitate ER PQC, as well as PTMs that play a role in ER PQC<sup>20,21</sup>. In this chapter, we discuss and highlight a number of investigations and techniques involving MS-based proteomics that have been pivotal in investigating mechanisms of ER stress and PQC.

PQC mechanisms are driven by protein-protein interactions with a diverse set of proteostasis factors motivating efforts to identify the critical components. On the one hand, MS has aided in the global profiling of proteostasis components, as well changes during disease states and drug treatments. On the other hand, affinity purification – mass spectrometry (AP-MS) has been the most widely used technique to characterize protein-protein interactions enabling interactomics studies<sup>21</sup>. Additionally, liquid chromatography – tandem mass spectrometry (LC-MS/MS) instrumentation and methods have advanced as a robust system for investigations across sample types, yielding great depth, precision, and throughput in protein identification and quantification<sup>22–24</sup>. In AP-MS, a protein of interest (bait) and interacting proteins (prey) are copurified via affinity bead matrix. After subsequent wash steps to rid the sample of non-specific background, the purified protein

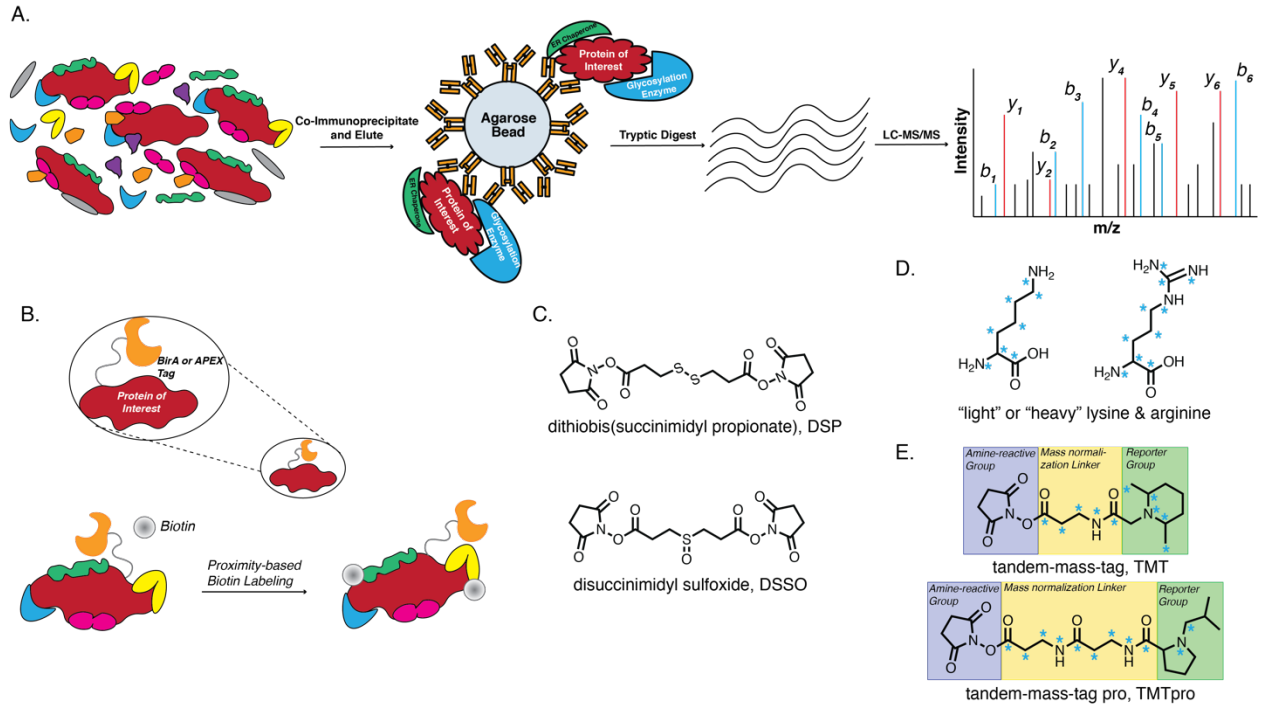


### Figure 1.3: Affinity purification – mass spectrometry and tool compounds to elucidate protein-protein interactions

(A) Schematic detailing a typical AP-MS workflow. Extracted protein samples are subjected to immunoprecipitation or affinity purification, either through direct antibody detection of the protein of interest or other molecules that recognize an epitope tag on the protein of interest.

(B) Proximity labeling MS commonly uses a promiscuous BirA biotin ligase-tagged (as is the case for BioID) or ascorbic acid peroxidase-tagged (in the case of APEX-MS) protein of interest to biotinylate interacting proteins. Biotinylated proteins can then be affinity purified and analyzed via LC-MS/MS to identify interacting partners.

(C) Protein crosslinkers aid in affinity purification of interacting proteins by covalently linking them and can subsequently be used to identify crosslinked peptides in some cases.

(D) Stable isotope labeling with amino acids has aided in quantitative mass spectrometry experiments. Blue asterisks indicate atoms where heavy isotopes can be incorporated.

(E) Isobaric labeling has aided in quantitative mass spectrometry investigation and increased throughput through sample multiplexing. Blue asterisks indicate points where heavy isotopes can be incorporated.

and interaction partners are eluted from the bead matrix, digested using one or multiple proteases, and subsequently analyzed via LC-MS/MS [Figure 1.3A]. A control AP-MS sample, often using an untagged bait or sample lacking the bait all together, is traditionally

used to delineate true interacting proteins from non-specific background bound to the bead matrix during affinity purification. Other methods to investigate interactions take advantage of proximity labeling using a modified biotin ligase (BioID) or ascorbic acid peroxidase (APEX) fused to the bait protein of interest [Figure 1.3B]<sup>25,26</sup>. Exogenously supplied biotin substrates are then activated by the enzymes and covalently modify proteins in close proximity to the bait, where the proximity radius is controlled by the lifetime of the activated substrate. AP-MS experiments may utilize protein crosslinkers to covalently link interacting proteins [Figure 1.3C]. This is particularly useful in the case of studying protein-protein interactions within the ER-PN, as these interactions are often transient (having fast on-off rates) in nature. Furthermore, the identification of crosslinked peptides can provide structural insight into how these interactions take place<sup>27</sup>. Lastly, quantitative methods such as stable isotope labeling with amino acids in cell culture (SILAC) or isobaric labeling such as tandem mass tags have aided in quantifying changes in interaction that take place during ER PQC and disease states [Figure 1.3D and 1.3E]<sup>28-31</sup>. Most of the investigations discussed here utilize AP-MS and have largely been separated into two categories: (1) proteostasis network-centric investigations focused on the topological arrangement and functions of ER-PN components with one another, and (2) client-centric investigations focused on the coordination and engagement of ER-PN components with specific client proteins routed through the ER.

### **1.3 Proteostasis Network-Centric Investigations**

This chapter highlights three subsets of proteostasis-centric investigations: chaperone-assisted protein folding, protein degradation, and UPR activation. These categories are not all-encompassing and could easily be broken down into further subcategories.

### *1.3.1 ER chaperoning complexes*

Chaperone/co-chaperone systems and other protein folding complexes are essential to maintaining ER proteostasis. The Hsp70/40 chaperone system and the calreticulin/calnexin cycle are perhaps the most notable examples<sup>6,10</sup>. In the ER, the lone Hsp70 HSPA5/BiP facilitates protein folding and relies on interactions with many Hsp40/J-Domain containing proteins that can directly bind clients to recruit HSPA5 for protein folding, recruit other factors to aid in ERAD, and additionally regulate the ATPase activity of HSPA5<sup>5,32,33</sup>. In the case of glycoproteins, the ER lectins calreticulin (CALR) and calnexin (CANX) coordinate with the protein disulfide isomerase PDIA3/ERp57 and glucosyltransferase UGGT1, along with other glycan modifying enzymes to facilitate glycoprotein folding<sup>10</sup>.

An early study by Meunier et al. found ER-PN subcomplexes that were hypothesized to be responsible for the processing of ER clients<sup>34</sup>. AP-MS led to the identification of a number of ER components including UGGT1, DNAJB11/ERdj3, PPIB, SDF2L1, HSP90B1/GRP94, CALR, PDIA, PDIA3, PDIA6, besides HSPA5, which had been previously identified. Further characterization of preformed ER-PN complexes detailed novel chaperone engagement and rearrangement, for instance showing that HSPA5,

HSP90B1, DNAJB11, and HYOU1/GRP170 could exist as large complexes even in the absence of a client. Additionally, the authors identified a HSPA5-associated complex including HSP90B1, HYOU1, PDIA6, PPIB, and SDF2L1. Ultimately, this study provided new insight detailing that the formation of ER complexes can concentrate chaperones and folding components onto newly synthesized clients during folding. This was the first investigation to provide evidence for the existence of ER subnetworks from which client proteins are shuttled from one complex to another to facilitate folding.

In subsequent years, a number of studies on global protein-protein interactions in yeast provided further discoveries into ER-PN organization<sup>35,36</sup>. In 2009, Gong et al. published a study of the global landscape of the yeast chaperone network – including all 63 known chaperones<sup>37</sup>. This dataset included a mixture of AP-MS and the *Saccharomyces* Genome Database (SGD) data. As the authors characterized ER chaperones (human homologs denoted in parentheses throughout the rest of the chapter) including, ERj5 (DNAJC10/ERdj5), Hlj1 (DNAJB4), Jem1, Sec63, Scj1 (DNAJC11), Kar2 (HSPA5), and Lhs1 (HYOU1), revealing key ER-PN components and chaperone organization. All identified ER components were found to interact with various cytoplasmic, nuclear, and mitochondrial components. This organelle crosstalk included interactions across organelle-specific Hsp70/40 systems, along with specific ER Hsp40 to cytosolic Hsp104s and prefoldin proteins. Additionally, the “promiscuity” of given proteostasis components as measured by the number of clients they could bind, revealed ER chaperones to be the least promiscuous (most specific), as compared to PN components found in other

organelles. Furthermore, the authors detailed how Scj1/DNAJC11 may play a key role in ER to cytoplasmic and nuclear chaperone communication. On the whole, this work described unseen connectivity between ER chaperone networks and other organelles.

Subsequently, the ER *chaperome* of mammalian cells was further detailed through a combinatorial approach termed ER membrane yeast two-hybrid system and affinity purification (ER-MAP)<sup>38</sup>. Rather than utilizing antibodies that recognized particular ER-PN components, the authors used a unique method of directly functionalizing sepharose matrix with HSPA5, PDIA5, PDIA1, PDIA9/ERp29, PDIA4/ERp72, FKBP13, PPIB, PDIA3, or EDEM1-3 for subsequent AP-MS of ER complexes. They identified subnetworks of interactions within the ER across protein folding classes including HSPA5 with peptidyl prolyl isomerases (PPIs) and protein disulfide isomerases (PDIs), further highlighting the role of HSPA5 as a hub for ER multiprotein complexes<sup>32</sup>. Additionally, ER degradation enhancing alpha mannosidase like proteins (EDEMs) were found to interact with PDIs and other oxidative folding components. Particularly, PDI and PPI interactions were specific and formed exclusive pairs. This was especially the case for PDIA4 and PPIB. Further work revealed the concerted ability of PDIA4 and PPIB interactions to increase the rate of immunoglobulin IgG processing in vitro. These results were particularly revealing as disulfide formation and prolyl isomerization are thought to be the rate-limiting steps of many ER clients<sup>39,40</sup>. Overall the findings uncovered a diverse ER-PN functional landscape and a number of novel interactions between proteostasis



components. The concerted effort of these subnetworks can increase protein folding efficiency, further corroborating results and speculations proposed by Meunier et al<sup>34</sup>.

### *1.3.2 ER membrane complex and transmembrane proteins*

Many transmembrane proteins are implicated in protein folding disease states, for instance cystic fibrosis transmembrane conductance regulator (CFTR), potassium voltage-gated channels, GABA receptors, and Niemann-Pick disease C1 protein (NPC1), and elucidating specific ER-PN and mechanisms responsible for folding of such clients established a key research area<sup>41</sup>. One complex responsible for the processing of transmembrane clients is the ER membrane protein complex (EMC). Since its identification in 2009, multiple investigations have characterized the importance of the EMC<sup>42–45</sup>, yet many questions still remained as to whether the EMC played a direct or indirect role in membrane protein biogenesis, what substrates it acted on, and what role the EMC played during client insertion into the membrane. In 2018, a seminal study by Shutleff et al. tackled these questions<sup>31</sup>. Utilizing SILAC and AP-MS for comparative interactome screening of EMC3, an EMC subunit, the authors identified specialized yeast membrane protein chaperones Sop4 (EMC7) and Gsf2 (EMC6), along with other oxidative folding components, Ero1, and general chaperones Ssa1, Ssb1 (both Hsp70 homologs), and Kar2. A series of knock-out experiments of membrane chaperones Ilm1 and Sop4 revealed the EMC could directly bind transmembrane clients to aid in folding. With interactions between transmembrane clients, membrane protein-specific

chaperones, general chaperones, and the ribosome itself, the EMC acts as a hub for transmembrane protein folding and processing within the ER. Furthermore, using BioID, the authors found that the EMC can interact cotranslationally with clients, showing a specificity for difficult to fold transmembrane proteins such as transporters and ion channels with charged residues within the lipid bilayer. These findings also held true in mammalian cells, ultimately establishing foundational principles for the action of the EMC. Mass spectrometry experiments in further studies were critical for determining that the EMC is needed for membrane insertion and PQC of diverse transmembrane proteins, for instance connexin 32, a gap junction protein disrupted in Charcot-Marie-Tooth disease, as well as sterol homeostasis enzymes<sup>46,47</sup>.

### *1.3.3 ER-associated degradation (ERAD) and ER-phagy*

If folding and trafficking of ER clients fails, degradation of misfolded or damaged clients plays an equally important role in maintaining ER proteostasis<sup>12,14,48</sup>. Additionally, turnover of the ER itself plays a key function in ER homeostasis, acting to remove aggregated clients and damaged ER regions, or alter the size and shape of the ER during stress and recovery<sup>13,14,49</sup>. Much work has been dedicated to elucidating PQC mechanisms associated with the two major degradation pathways associated with the ER: ERAD and ER-phagy.

In 2006, Carvalho et al. characterized a new ERAD pathway for integral membrane proteins, termed ERAD-M<sup>50</sup>. Pathways facilitating ERAD of luminal, or membrane clients

with misfolded or damaged cytosolic domains, termed ERAD-L and ERAD-C respectively, were previously defined<sup>51,52</sup>. While it was clear that different ERAD substrates employed differing routes of degradation, the organization of ERAD machinery within those pathways and whether clients with misfolded transmembrane domains used the same or a different set of ERAD pathways remained unclear. By characterizing the interactomes of yeast ubiquitin ligases involved in ERAD-C and ERAD-L, Doa10 (MARCF6), and Hrd1 (HRD1) respectively, the authors defined the complexes implicated in the given ERAD pathways<sup>50</sup>. The Doa10 complex proved to be relatively simple including Ubc7(UBE2G2), Cdc48 (VCP), Npl4 (NPLOC4), and Ubx2 (FAF2). Hrd1, Hrd3 (SEL1L), Der1 (DER1), and a novel complex component, Usa1 (HERP), formed the majority of the Hrd1 complex. Accessory components including Yos9 (OS-9), Ubx2, and Cdc48, highlighted some overlapping complex components between ERAD-C and ERAD-L pathways. Further characterization revealed that the Hrd1 complex was used to facilitate ERAD-M<sup>50</sup>. Additional work by Christianson, Olzman, et al. meticulously detailed these ERAD complexes in mammalian cells to gain further insight into ERAD subnetworks<sup>53</sup>. The authors defined the major ERAD subnetworks, including SEL1L-HRD1, Gp78, the E3 ubiquitin ligase-26S proteasome, and provided the first identification and characterization of the mammalian EMC. Using model ERAD-L, ERAD-C, and ERAD-M substrates, they were able to detail how these subnetworks utilized adaptive mechanisms to facilitate degradation on a client-specific basis. A recent comprehensive interactome study of 25 poorly characterized ER transmembrane E3 ubiquitin ligases and associated

complexes revealed new insights into the role of RNF26 in controlling STING levels and associated innate immune signaling pathways<sup>54</sup>.

Since it was first characterized, ER-phagy/Reticulophagy (a contraction of the endoplasmic reticulum and macroautophagy) has proven to play a key role in ER protein homeostasis and ER stress<sup>49,55,56</sup>. As such, key regulators and mechanisms of this process have been further studied, and three of the six ER-phagy receptors have been identified and characterized using AP-MS. Grumati et al. performed a comparative interactome screen of reticulon related proteins (RTN1-4) thought to play a role in ER-phagy by recruiting cargo into autophagosome structures<sup>57</sup>. Preliminary work confirmed RTN3 was necessary for ER fragmentation and delivery to the lysosome. The authors found that this class of proteins shared the majority of interacting proteins, yet the full-length isoform of RTN3 was the only one found to act as an autophagy receptor by interacting with GABARAP-L1, an essential protein for autophagosome maturation. Subsequently, Smith et al. used a similar approach and defined the novel interaction of a previously uncharacterized protein, CCPG1, with GABARAP<sup>58</sup>. The authors defined the CCPG1 interactome, leading to the identification of a robust interaction with an additional autophagy component, FIP200. Further characterization showed that CCPG1 expression was regulated by the UPR and drove ER-phagy via distinct interactions with GABARAP and FIP200. In 2019, Chino et al. discovered and characterized the most recently identified ER-phagy receptor, TEX264<sup>59</sup>. Similarly, using comparative interactome screening of LC3B – another protein involved in autophagosome formation, the authors

identified TEX264 as a unique interactor displaying high specificity yet no known role in autophagy. Follow up work characterized the TEX264-LC3B interaction and led to the identification of TEX264 as a major ER-phagy receptor. In two of the three cases presented here, CCPG1 and TEX264, the ER-phagy receptors were either poorly annotated or had no assigned function, highlighting the ability of AP-MS to not only define protein-protein interactions and mechanisms of PQC but discover new or previously unappreciated biological function of those proteins.

#### *1.3.4 Adapting ER proteostasis through the Unfolded Protein Response*

As the dysregulation of the UPR is implicated in a number of disease states and has even emerged as a drug target to combat such diseases, characterizing the regulation and consequences of UPR activation has become major topic of ER PQC investigations<sup>17,60,61</sup>. Studies have determined how UPR activation coordinates the upregulation of ER proteostasis factors to influence PQC mechanisms, and furthermore how the modulation of the UPR can be used to combat such protein folding diseases.

Shoulders et al. engineered a cell line where chemical genetics tools enabled preferential activation of the ATF6 and IRE1/XBP1s arms of the UPR in isolation or in combination [Fig. 2], independent of ER stress<sup>30</sup>. This allowed for the characterization of changes to the ER-PN composition using SILAC-based quantitative proteomics, revealing distinct, and overlapping gene products of each UPR arm that are used to remodel the ER-PN. Particularly, XBP1s activation provided a more concerted impact on many ER proteostasis pathways. This is in line with IRE1-XBP1s signaling being the single UPR

arm conserved from yeast to humans<sup>17,19</sup>. On the contrary, ATF6 specifically upregulated key proteostasis factors in distinct pathways, such as the Hsp70 and Hsp90 chaperones HSPA5 and HSP90B1, disulfide isomerase PDIA4, as well as several degradation factors. At the same time, several other degradation pathways were cooperatively upregulated through both XBP1s and ATF6 arms.

AP-MS studies on the UPR sensors has produced insights into the mechanisms of regulation during ER stress adaptation. For instance, an IRE1 interactome revealed the E3 ubiquitin ligase CHIP to be a key interactor demonstrating that CHIP-mediated K63-linked ubiquitination plays a role in the UPR regulation<sup>62</sup>. This modification was discovered to play a critical role in controlling the pro-apoptotic activation of the TRAF2/JNK pathway and is significantly increased under ER stress<sup>63</sup>. As IRE1 undergoes increased phosphorylation during UPR induction, ubiquitination of IRE1 is similarly elevated. Increased signaling of the IRE1/TRAF2/JNK pathway antagonized cellular senescence. These findings revealed another connection between ER stress and UPR activation to aging<sup>64</sup>. Sepulveda et al. conducted a complementary interactome screening of IRE1 under basal and ER stress conditions to investigate regulatory mechanisms of UPR activation<sup>65</sup>. In this study, the collagen-specific chaperone SERPINH1/Hsp47 stood out as an interactor that potentiated the activation of IRE1. Specifically, the authors found that Hsp47 and HSPA5, often thought of as the major regulator of the UPR, bound to IRE1 with the same affinity<sup>66</sup>. This regulation by Hsp47 held true in *D. melanogaster* and mouse models of ER stress. The authors proposed a model whereby Hsp47 competes

with HSPA5 during UPR activation titrating HSPA5 off from the luminal domain of IRE1 further tuning the IRE1 response of the UPR<sup>65</sup>.

Another investigation probed the role ubiquitination plays in the regulation of translational machinery during ER stress and UPR activation<sup>67</sup>. Higgins, Gendron et al. used quantitative diGly proteomics to characterize the ubiquitin modified proteome (ubiquitylome) under conditions of the ER stressors DTT, tunicamycin, and epoxomicin. The authors found that diGly peptides corresponded with proteins enriched in functions related to mRNA translation and were localized to the cytosolic ribosome. Time-course analysis revealed ubiquitylome remodeling of the 40S ribosome as an early UPR event necessary to inhibit protein translation. Furthermore, authors showed that PERK and eIF2 $\alpha$  phosphorylation were necessary but not sufficient to mount UPR-induced regulatory ubiquitination of the 40S ribosome. Insults to this process resulted in elevated sensitivity to UPR-induced cell death, with this regulatory mechanism holding true in *D. melanogaster* and yeast as well.

#### **1.4 Client-Centric Investigations**

While many investigations have focused on elucidating mechanisms of PQC by investigating subnetworks of the ER-PN, these investigations do not provide an integrated view of how these subnetworks converge to perform the concurrent folding, processing, secretion and degradation of clients routed through the secretory pathway. To address

these questions, MS-based studies have also focused on investigating mechanisms of PQC for protein clients, in particular ones involved in protein misfolding and aggregation disease. These client-centric investigations provide a holistic view of client processing by integrating ER-PN subnetworks and have aided in the development of therapeutic treatment strategies for disease states.

#### *1.4.1 Loss-of-function protein misfolding diseases*

Cystic fibrosis (CF) is one of the most prevalent protein folding diseases caused by loss of function of the chloride ion channel CFTR, responsible for salt homeostasis in polarized epithelial cells<sup>68</sup>. This results in an inability to clear mucus from the respiratory tract and can lead to chronic infection, respiratory failure, and ultimately death. The most prevalent CFTR mutations in CF patients, deletion of phenylalanine 508 ( $\Delta F508$ ), results in improper processing of this ion channel<sup>69</sup>. While  $\Delta F508$  CFTR can be functional as an ion channel if trafficked to the plasma membrane, improper folding, and rapid degradation within the secretory pathway result in a loss of expression at the cell surface. To investigate the molecular mechanisms associated with CFTR processing, Pankow et al. detailed the interactomes of WT and  $\Delta F508$  CFTR<sup>28,70</sup>. Using a comparative AP-MS based interactome analysis, the authors identified 638 total high confidence interactors with 576 and 430 for  $\Delta F508$  and WT CFTR respectively. While some interactions between the two proteins remained the same, the relative abundance of those interactions significantly differed for a number of them. Moreover, 208 and 62 interactors were found



to bind exclusively with  $\Delta F508$  and WT CFTR respectively, highlighting gain of novel interactions as a hallmark of  $\Delta F508$  misprocessing. Furthermore, well-established correction treatment that can restore CFTR biogenesis and trafficking (either by lowering cell culture temperature to 26-30°C, or addition of histone deacetylase inhibitor SAHA) correlated with the abolishment of mutant-specific proteostasis network interactions<sup>71,72</sup>. Many of these interactions were associated with ERAD and heat-shock assisted protein folding, among others. The authors went on to further detail that inhibition of key interactors associated with ER retention, trafficking, and degradation promoted the maturation of  $\Delta F508$  CFTR. Ultimately this study resulted in a comprehensive mapping of the WT and  $\Delta F508$  CFTR interactomes, provided some of the first insight into the molecular mechanisms of temperature correction for  $\Delta F508$  CFTR, and generally detailed disease-specific alterations that take place and may be implicated in other protein misfolding diseases. Follow-up interactomics studies on additional CFTR mutant variants and clinically approved small molecule correctors and potentiators, VX-809 and VX-770 respectively, have expanded our understanding of the role of proteostasis dysregulation in CF<sup>73</sup>. Furthermore, work in the Plate laboratory has characterized the susceptibility and requirements of select CFTR mutations to respond to VX-809 treatment<sup>74</sup>. These studies have established a methodology that can be further expanded to other genetic disorders to implement precision medicine-based approaches for clinical treatment of such diseases.

Collagen proteinopathies such as osteogenesis imperfecta (IO) and Ehlers-Danlos syndrome are caused by divergent missense mutations in collagen that lead to misprocessing and improper protein secretion resulting in weakened connective tissue<sup>74</sup>. AP-MS of collagen I expressed in fibrosarcoma cells was used to define the collagen I PN interactome<sup>75</sup>. Comparative SILAC-based quantitative interactomics identified the non-canonical protein disulfide isomerase PDIA9 as a crucial factor promoting collagen retention under ascorbate-limited conditions, a critical cofactor required for post-translational modifications on collagen<sup>76</sup>. A recent follow-up study characterized the PQC defects of the C1163R variant in the C-pro trimerization domain of collagen  $\alpha 2(I)$  associated with IO resulting in complete loss of secretion<sup>77</sup>. Comparative studies uncovered increased associations with a broad set of proteostasis factors, including HSPA5, HSP90B1, co-chaperones, and several PDIs that pointed to a disruption of disulfide network formation and improper targeting of the collagen mutant to ERAD by Hsp70/40 chaperone networks.

#### *1.4.2 Protein aggregation diseases*

AP-MS studies have also shed light on ER proteostasis defects that promote secretion of gain-of-toxic function protein variants involved in protein aggregation disease, for instance interactions and PQC mechanisms implicated in the processing of amyloidogenic immunoglobulin light chain (LC) protein responsible for light-chain amyloidosis (AL)<sup>29</sup>. Secretion of destabilized LC can result in the formation of toxic extracellular aggregates

leading to systemic organ damage in AL, in particular cardiac amyloidosis<sup>78</sup>. Previous studies showed that selective, stress-independent activation of the ATF6 branch of the UPR preferentially reduced the secretion of destabilized LC (ALLC) while leaving a non-amyloidogenic LC and intact IgGs unscathed<sup>79</sup>. Yet, the molecular mechanisms associated with this selective PQC enhancement were not well characterized. By comparing the proteostasis interactomes of ALLC in the presence of ATF6 activation, XBP1s activation, or both, the authors were able to identify key interactions and thus deduce mechanisms responsible for the decreased secretion of the aggregation prone ALLC. XBP1s activation decreased overall ALLC engagement of ER protein folding components, yet increased routing towards degradation, and only modestly reduced secretion. Conversely, ATF6 activation resulted in increased engagement with a subset of ER proteostasis components with ALLC, particularly HSPA5, HSP90B1, DNAJB11, HYOU1, and PDIA4. The authors further showed that ATF6 activation promoted increased engagement of these ER-PN components with non-amyloidogenic LC, which suggested these increased interactions are independent of client stability. Overexpression of these key ER-PN components showed that the reduction in ALLC secretion is coordinated by ATF6-mediated activation of a cooperative set of proteostasis factors, as overexpression of these individual ER-PN components only partially mimicked the reduction in ALLC secretion found with ATF6 activation<sup>29</sup>. This work highlighted the targeting of proteostasis pathways as a therapeutic intervention for such protein folding and amyloidogenic diseases as it established the mechanism of ATF6-dependent reduction of ALLC secretion<sup>17,80,81</sup>.

### *1.4.3 Viral proteostasis clients*

While many client-centric investigations have focused on protein folding diseases, a number of studies investigating viral host-pathogen interactions involving the ER-PN have also emerged. Hafirassou et al. mapped the interactome of the dengue virus (DENV) non-structural protein 1 (NS1)<sup>82</sup>. DENV, like other flaviviruses, uses the ER membrane for replication by forming invaginations to assemble the replication complex (RC)<sup>83</sup>. NS1 plays a variety of roles during DENV infection, including acting as a cofactor during DENV replication. Furthermore, it is the only viral non-structural protein secreted from infected host-cells, and extracellular NS1 disrupts the glycocalyx of endothelial cells increasing vascular leakage, which is the hallmark of Dengue hemorrhagic fever<sup>84</sup>. Yet, the host factors involved in viral replication and secretion of NS1 were not well characterized. The authors mapped 499, 654, and 438 host-NS1 interactions across Daji, HeLa, and HAP1 cells respectively and found 270 host factors to interact across all three cell lines<sup>82</sup>. The NS1 interactome was enriched in ER components involved in ERAD including SEL1L, AUP1, HM13, and the large majority of the oligosaccharyltransferase (OST) complex. Further investigation into these host components allowed the authors to delineate host restriction factors found to combat viral production, including ER residents NOMO1, NCLN, NCSTN, PGRMC1, MLEC, and RCN1 and host dependency factors found to promote viral production including Sec63, Sec61A1 and other ER translation and translocation components, STT3A, STT3B, DDOST, and other N-glycosylation

components, along with ERAD components previously mentioned. Follow up investigations revealed that glycosylation of NS1 by the OST complex is critical for the folding and stability of the protein, as inhibition of OST complex resulted in decreased DENV infection<sup>82,85</sup>.

A different study by Coyaud et al. used two complementary approaches, AP-MS and BioID to map the Zika virus (ZIKV) interactome<sup>86</sup>. Expressing all 10 ZIKV proteins, the authors found that, similar to the DENV interactome, interacting partners were enriched in ER components. Major ER-localized proteins included members of the signal peptidase complex (SPC), EMC, and the BAT3 complex. The authors also found that ER protein folding components prolyl 4-hydroxylase subunit B (P4HB), the lectin CANX, along with the ER-phagy receptor FAM134B localized into in these capsid protein-associated structures. Ultimately, these findings revealed that the capsid plays a diverse role in remodeling ER membranes. Additionally, NS3 was found to associate with the ubiquitin proteasome system (UPS), the degradation system responsible for clearing a number of proteins from the cell, including ER clients<sup>14</sup>. Overall, 7 of the 10 expressed ZIKV proteins localized or associated with the ER in some way, highlighting their involvement in forming virus-induced membrane structures used for RC formation.

A *tour-de-force* comparative AP-MS study mapped the interactomes of DENV and ZIKV flavivirus proteins across human and mosquito cell lines<sup>87</sup>. This was the first study to perform a systematic comparison of flavivirus-host interactions in primate and vector host

cells. In line with previous studies, the authors found that viral proteins interacted with host components associated with the ER. Specifically, translocon and CANX/CALR cycle ER-PN components were found to have distinct interactions with DENV proteins. Additionally, p62, a key accessory protein required for the degradation of a number of substrates and organelles was also identified, potentially highlighting its involvement in DENV protein turnover, or turnover of the ER itself during DENV infection. Investigations into ZIKV in human and mosquito cells allowed the authors to identify key components across flavivirus strains and cell types that may be viable host-centric therapeutic targets. OST subunits STT3A, STT3B and RPN2 as well as HYOU1 and trafficking component interactions were conserved across DENV and ZIKV and the different cell types. The authors identified the Sec61 translocon and signal recognition particle receptor (SRPR) as the most conserved interactors across all flavivirus strains and cell types, and revealed that cotranslational protein translocation inhibitors nearly abolished viral production, even when cells were treated post-infection. Furthermore, inhibiting protein translocation did not affect cell viability. This suggested that inhibition of the Sec61 translocon may serve as a viable anti-viral target. This work highlighted distinct and conserved host-pathogen interactions across multiple flavivirus species and strains and host cell types, furthermore highlighting the ability of AP-MS to not only identify interactions with ER components but identify potential therapeutic targets. Recently, a similar comprehensive AP-MS interactome characterization of 26 SARS-CoV-2 viral proteins revealed important leads for repurposing existing and approved therapeutics that target the identified host cell interactors for COVID-19 treatment<sup>89–91</sup>.

## 1.5 Future Directions and Scope of Dissertation

Mass spectrometry has clearly proven to be a valuable tool to biological investigations of protein-protein interactions, and as we presented here its impact on elucidating particularly mechanisms of ER stress and PQC. As technology and methodology continues to advance, the scope of mass spectrometry will expand to yield deeper insights into these biological processes. Many underexplored areas of ER stress and PQC still remain, where mass spectrometry would be a well-suited method to make further discoveries. For example, in many of the cases presented here the added complexity of how PTMs on clients and ER-PN components influence mechanisms of PQC are not fully characterized. As a follow up study to the CFTR interactome profiling, Pankow et al. showed that a PTM code on CFTR is altered for  $\Delta F508$  CFTR and this alteration correlated with an inability to properly fold and localize to the plasma membrane<sup>89</sup>. The authors further speculated that similar codes may be present in other transmembrane proteins. PTMs have also been implicated in the stability and activity of ER proteostasis components including HSPA5 and PDI. N-terminal arginylation promotes the degradation of HSPA5 via autophagy through p62 binding<sup>90</sup>. Additionally, AMPylation of HSPA5 plays a key role in its chaperoning activity, particularly during ER stress<sup>91</sup>. A similar regulatory mechanism was recently documented for PDI as it was found that phosphorylation alters PDI oxido-reductase activity to become a “holdase” to attenuate ER stress<sup>92</sup>. How these PTMs on individual proteostasis components regulate the

network of proteostasis subcomplexes and their coordination to mediate proper PQC have yet to be realized.

### *1.5.1 Scope of Dissertation*

Despite technological advances both on the side of instrumentation as well as bioinformatics in mass spectrometry, one of the largest limitations that current mass spectrometry-based methods have when identifying proteostasis interactions, as well as PTMs, is that interactions in the ER are very dynamic and highly transient in nature and identifying these interactions and modifications using current methods only provides a snapshot of the state of the ER at a given time. One could imagine that methods for elucidation of these protein-protein interactions or PTMs in a time-dependent manner would allow for a more complete understanding of ER stress and PQC mechanisms, illuminating previously unseen or poorly understood mechanisms<sup>93</sup>.

The following chapters of this thesis bestow work that addresses the challenge of identifying protein-protein interactions in a time-dependent manner. The first portion covered will focus on utilizing AP-MS methodology to characterize disease-associated interactome changes of a client protein in a protein folding disease. In particular, this work will focus on thyroglobulin (Tg), and destabilized mutations that result in the manifestation of congenital hypothyroidism (CH). Chapter 2 lays out experimental methods and results on the characterization of these changes. Chapter 3 expounds on this work and presents the development of a new quantitative mass spectrometry-based method to temporally



characterize these changes associated with Tg processing and CH-associated Tg mutations. Chapter 4 involves the investigation into the functional implications of such interactions in CH and Tg processing on the whole, and identifies potential pathways that may be attractive for modulation of Tg processing in the context of CH. Chapter 5 will close with an outlook on future directions of the work established here, as well as the broader implications that these and future discoveries will have on the field.

## 1.6 References

1. Braakman, I. & Hebert, D. N. Protein Folding in the Endoplasmic Reticulum. *Cold Spring Harbor Perspectives in Biology* **5**, a013201–a013201 (2013).
2. Balchin, D., Hayer-Hartl, M. & Hartl, F. U. In vivo aspects of protein folding and quality control. *Science (1979)* **353**, aac4354 (2016).
3. Mandon, E. C., Trueman, S. F. & Gilmore, R. Protein Translocation across the Rough Endoplasmic Reticulum. *Cold Spring Harbor Perspectives in Biology* **5**, a013342–a013342 (2013).
4. Voorhees, R. M. & Hegde, R. S. Structure of the Sec61 channel opened by a signal sequence. *Science (1979)* **351**, 88–91 (2016).
5. Vembar, S. S., Jonikas, M. C., Hendershot, L. M., Weissman, J. S. & Brodsky, J. L. J domain co-chaperone specificity defines the role of BiP during protein translocation. *Journal of Biological Chemistry* (2010).
6. Behnke, J., Mann, M. J., Scruggs, F.-L., Feige, M. J. & Hendershot, L. M. Members of the Hsp70 Family Recognize Distinct Types of Sequences to Execute ER Quality Control. *Molecular Cell* **63**, 739–752 (2016).
7. Feige, M. J. & Hendershot, L. M. Quality Control of Integral Membrane Proteins by Assembly-Dependent Membrane Integration. *Molecular Cell* **51**, 297–309 (2013).
8. Ruiz-Canada, C., Kelleher, D. J. & Gilmore, R. Cotranslational and Posttranslational N-Glycosylation of Polypeptides by Distinct Mammalian OST Isoforms. *Cell* (2009).
9. Braunger, K. *et al.* Structural basis for coupling protein transport and N-glycosylation at the mammalian endoplasmic reticulum. *Science (1979)* **360**, 215–219 (2018).
10. Lamriben, L., Graham, J. B., Adams, B. M. & Hebert, D. N. N -Glycan-based ER Molecular Chaperone and Protein Quality Control System: The Calnexin Binding Cycle. *Traffic* **17**, 308–326 (2016).

11. Gomez-Navarro, N. & Miller, E. Protein sorting at the ER–Golgi interface. *Journal of Cell Biology* **215**, 769–778 (2016).
12. Needham, P. G., Guerriero, C. J. & Brodsky, J. L. Chaperoning Endoplasmic Reticulum–Associated Degradation (ERAD) and Protein Conformational Diseases. *Cold Spring Harbor Perspectives in Biology* **11**, a033928 (2019).
13. Schuck, S., Gallagher, C. M. & Walter, P. ER-phagy mediates selective degradation of endoplasmic reticulum independently of the core autophagy machinery. *Journal of Cell Science* **127**, 4078–4088 (2014).
14. Pohl, C. & Dikic, I. Cellular quality control by the ubiquitin-proteasome system and autophagy. *Science (1979)* **366**, 818–822 (2019).
15. Knowles, T. P. J., Vendruscolo, M. & Dobson, C. M. The amyloid state and its association with protein misfolding diseases. *Nature Reviews Molecular Cell Biology* **15**, 384–396 (2014).
16. Karagöz, G. E., Acosta-Alvear, D. & Walter, P. The Unfolded Protein Response: Detecting and Responding to Fluctuations in the Protein-Folding Capacity of the Endoplasmic Reticulum. *Cold Spring Harbor Perspectives in Biology* **11**, a033886 (2019).
17. Plate, L. & Wiseman, R. L. Regulating Secretory Proteostasis through the Unfolded Protein Response: From Function to Therapy. *Trends in Cell Biology* **27**, 722–737 (2017).
18. Grandjean, J. M. D. *et al.* Deconvoluting Stress-Responsive Proteostasis Signaling Pathways for Pharmacologic Activation Using Targeted RNA Sequencing. *ACS Chemical Biology* **14**, 784–795 (2019).
19. Schneider, K. & Bertolotti, A. Surviving protein quality control catastrophes - from cells to organisms. *Journal of Cell Science* **128**, 3861–3869 (2015).
20. Cravatt, B. F., Simon, G. M. & Yates III, J. R. The biological impact of mass-spectrometry-based proteomics. *Nature* **450**, 991–1000 (2007).
21. Bludau, I. & Aebersold, R. Proteomic and interactomic insights into the molecular basis of cell functional diversity. *Nature Reviews Molecular Cell Biology* (2020).
22. Bian, Y. *et al.* Robust, reproducible and quantitative analysis of thousands of proteomes by micro-flow LC–MS/MS. *Nature Communications* **11**, 157 (2020).
23. Rauniyar, N. & Yates, J. R. Isobaric Labeling-Based Relative Quantification in Shotgun Proteomics. *Journal of Proteome Research* **13**, 5293–5309 (2014).
24. Collins, B. C. *et al.* Quantifying protein interaction dynamics by SWATH mass spectrometry: application to the 14-3-3 system. *Nature Methods* **10**, 1246–1253 (2013).
25. Samavarchi-Tehrani, P., Samson, R. & Gingras, A.-C. Proximity Dependent Biotinylation: Key Enzymes and Adaptation to Proteomics Approaches. *Molecular & Cellular Proteomics* **19**, 757–773 (2020).
26. Han, S., Li, J. & Ting, A. Y. Proximity labeling: spatially resolved proteomic mapping for neurobiology. *Current Opinion in Neurobiology* **50**, 17–23 (2018).
27. Leitner, A., Faini, M., Stengel, F. & Aebersold, R. Crosslinking and Mass Spectrometry: An Integrated Technology to Understand the Structure and Function of Molecular Machines. *Trends in Biochemical Sciences* **41**, 20–32 (2016).

28. Pankow, S. *et al.*  $\Delta$ F508 CFTR interactome remodelling promotes rescue of cystic fibrosis. *Nature* **528**, 510–516 (2015).
29. Plate, L. *et al.* Quantitative Interactome Proteomics Reveals a Molecular Basis for ATF6-Dependent Regulation of a Destabilized Amyloidogenic Protein. *Cell Chemical Biology* **26**, 913-925.e4 (2019).
30. Shoulders, M. D. *et al.* Stress-Independent Activation of XBP1s and/or ATF6 Reveals Three Functionally Diverse ER Proteostasis Environments. *Cell Reports* **3**, 1279–1292 (2013).
31. Shurtleff, M. J. *et al.* The ER membrane protein complex interacts cotranslationally to enable biogenesis of multipass membrane proteins. *Elife* **7**, (2018).
32. Pobre, K. F. R., Poet, G. J. & Hendershot, L. M. The endoplasmic reticulum (ER) chaperone BiP is a master regulator of ER functions: Getting by with a little help from ERdj friends. *Journal of Biological Chemistry* **294**, 2098–2108 (2019).
33. Otero, J. H., Lizák, B., Feige, M. J. & Hendershot, L. M. Dissection of Structural and Functional Requirements That Underlie the Interaction of ERdj3 Protein with Substrates in the Endoplasmic Reticulum. *Journal of Biological Chemistry* **289**, 27504–27512 (2014).
34. Meunier, L., Usherwood, Y.-K., Chung, K. T. & Hendershot, L. M. A Subset of Chaperones and Folding Enzymes Form Multiprotein Complexes in Endoplasmic Reticulum to Bind Nascent Proteins. *Molecular Biology of the Cell* **13**, 4456–4469 (2002).
35. Ho, Y. *et al.* Systematic identification of protein complexes in *Saccharomyces cerevisiae* by mass spectrometry. *Nature* **415**, 180–3 (2002).
36. Krogan, N. J. *et al.* Global landscape of protein complexes in the yeast *Saccharomyces cerevisiae*. *Nature* (2006).
37. Gong, Y. *et al.* An atlas of chaperone–protein interactions in *Saccharomyces cerevisiae*: implications to protein folding pathways in the cell. *Molecular Systems Biology* **5**, 275 (2009).
38. Jansen, G. *et al.* An Interaction Map of Endoplasmic Reticulum Chaperones and Foldases. *Molecular & Cellular Proteomics* **11**, 710–723 (2012).
39. Schmidpeter, P. A. M. & Schmid, F. X. Prolyl Isomerization and Its Catalysis in Protein Folding and Protein Function. *Journal of Molecular Biology* **427**, 1609–1631 (2015).
40. Ushioda, R. & Nagata, K. Redox-Mediated Regulatory Mechanisms of Endoplasmic Reticulum Homeostasis. *Cold Spring Harbor Perspectives in Biology* **11**, a033910 (2019).
41. Marinko, J. T. *et al.* Folding and Misfolding of Human Membrane Proteins in Health and Disease: From Single Molecules to Cellular Proteostasis. *Chemical Reviews* **119**, 5537–5606 (2019).
42. Jonikas, M. C. *et al.* Comprehensive Characterization of Genes Required for Protein Folding in the Endoplasmic Reticulum. *Science (1979)* **323**, 1693–1697 (2009).
43. Shen, X. *et al.* EMC6/TMEM93 suppresses glioblastoma proliferation by modulating autophagy. *Cell Death and Disease* (2016).

44. Lahiri, S. *et al.* A Conserved Endoplasmic Reticulum Membrane Protein Complex (EMC) Facilitates Phospholipid Transfer from the ER to Mitochondria. *PLoS Biology* **12**, e1001969 (2014).
45. Guna, A., Volkmar, N., Christianson, J. C. & Hegde, R. S. The ER membrane protein complex is a transmembrane domain insertase. *Science* (1979) **359**, 470–473 (2018).
46. Coelho, J. P. L. *et al.* A network of chaperones prevents and detects failures in membrane protein lipid bilayer integration. *Nature Communications* **10**, 672 (2019).
47. Volkmar, N. *et al.* The ER membrane protein complex promotes biogenesis of sterol-related enzymes maintaining cholesterol homeostasis. *Journal of Cell Science* **132**, jcs223453 (2019).
48. Oikonomou, C. & Hendershot, L. M. Disposing of misfolded ER proteins: A troubled substrate's way out of the ER. *Molecular and Cellular Endocrinology* **500**, 110630 (2020).
49. Fumagalli, F. *et al.* Translocon component Sec62 acts in endoplasmic reticulum turnover during stress recovery. *Nature Cell Biology* **18**, 1173–1184 (2016).
50. Carvalho, P., Goder, V. & Rapoport, T. A. Distinct Ubiquitin-Ligase Complexes Define Convergent Pathways for the Degradation of ER Proteins. *Cell* **126**, 361–373 (2006).
51. Bays, N. W., Gardner, R. G., Seelig, L. P., Joazeiro, C. A. & Hampton, R. Y. Hrd1p/Der3p is a membrane-anchored ubiquitin ligase required for ER-associated degradation. *Nature Cell Biology* **3**, 24–29 (2001).
52. Swanson, R. A conserved ubiquitin ligase of the nuclear envelope/endoplasmic reticulum that functions in both ER-associated and Matalpha 2 repressor degradation. *Genes & Development* **15**, 2660–2674 (2001).
53. Christianson, J. C. *et al.* Defining human ERAD networks through an integrative mapping strategy. *Nature Cell Biology* **14**, 93–105 (2012).
54. Fenech, E. J. *et al.* Interaction mapping of endoplasmic reticulum ubiquitin ligases identifies modulators of innate immune signalling. *Elife* **9**, (2020).
55. Bolender, R. P. & Weibel, E. R. A Morphometric study of the removal of phenobarbital-induced membranes from hepatocytes after cessation of treatment. *The Journal of Cell Biology* **56**, 746–761 (1973).
56. Bernales, S., McDonald, K. L. & Walter, P. Autophagy Counterbalances Endoplasmic Reticulum Expansion during the Unfolded Protein Response. *PLoS Biology* **4**, e423 (2006).
57. Grumati, P. *et al.* Full length RTN3 regulates turnover of tubular endoplasmic reticulum via selective autophagy. *Elife* **6**, (2017).
58. Smith, M. D. *et al.* CCPG1 Is a Non-canonical Autophagy Cargo Receptor Essential for ER-Phagy and Pancreatic ER Proteostasis. *Developmental Cell* **44**, 217–232.e11 (2018).
59. Chino, H., Hatta, T., Natsume, T. & Mizushima, N. Intrinsically Disordered Protein TEX264 Mediates ER-phagy. *Molecular Cell* **74**, 909–921.e6 (2019).

60. Kelly, J. W. Pharmacologic Approaches for Adapting Proteostasis in the Secretory Pathway to Ameliorate Protein Conformational Diseases. *Cold Spring Harbor Perspectives in Biology* a034108 (2019).
61. Hetz, C., Axten, J. M. & Patterson, J. B. Pharmacological targeting of the unfolded protein response for disease intervention. *Nature Chemical Biology* **15**, 764–775 (2019).
62. Zhu, X. *et al.* Ubiquitination of Inositol-requiring Enzyme 1 (IRE1) by the E3 Ligase CHIP Mediates the IRE1/TRAF2/JNK Pathway. *Journal of Biological Chemistry* **289**, 30567–30577 (2014).
63. Urano, F. Coupling of Stress in the ER to Activation of JNK Protein Kinases by Transmembrane Protein Kinase IRE1. *Science (1979)* **287**, 664–666 (2000).
64. Kaushik, S. & Cuervo, A. M. Proteostasis and aging. *Nature Medicine* **21**, 1406–1415 (2015).
65. Sepulveda, D. *et al.* Interactome Screening Identifies the ER Luminal Chaperone Hsp47 as a Regulator of the Unfolded Protein Response Transducer IRE1 $\alpha$ . *Molecular Cell* **69**, 238-252.e7 (2018).
66. Bertolotti, A., Zhang, Y., Hendershot, L. M., Harding, H. P. & Ron, D. Dynamic interaction of BiP and ER stress transducers in the unfolded-protein response. *Nature Cell Biology* **2**, 326–332 (2000).
67. Higgins, R. *et al.* The Unfolded Protein Response Triggers Site-Specific Regulatory Ubiquitylation of 40S Ribosomal Proteins. *Molecular Cell* **59**, 35–49 (2015).
68. Dalemans, W. *et al.* Altered chloride ion channel kinetics associated with the  $\Delta$ F508 cystic fibrosis mutation. *Nature* **354**, 526–528 (1991).
69. World Health Organisation. The molecular genetic epidemiology of cystic fibrosis. *Human Genetics Programme. Chronic Diseases and Health Promotion. World Health Organisation.* (2004).
70. Pankow, S., Bamberger, C., Calzolari, D., Bamberger, A. & Yates, J. R. Deep interactome profiling of membrane proteins by co-interacting protein identification technology. *Nature Protocols* **11**, 2515–2528 (2016).
71. Denning, G. M. *et al.* Processing of mutant cystic fibrosis transmembrane conductance regulator is temperature-sensitive. *Nature* **358**, 761–764 (1992).
72. Hutt, D. M. *et al.* Reduced histone deacetylase 7 activity restores function to misfolded CFTR in cystic fibrosis. *Nature Chemical Biology* **6**, 25–33 (2010).
73. Hutt, D. M., Loguercio, S., Campos, A. R. & Balch, W. E. A Proteomic Variant Approach (ProVarA) for Personalized Medicine of Inherited and Somatic Disease. *Journal of Molecular Biology* **430**, 2951–2973 (2018).
74. McDonald, E. F., Sabusap, C. M. P., Kim, M. & Plate, L. Distinct proteostasis states drive pharmacologic chaperone susceptibility for Cystic Fibrosis Transmembrane Conductance Regulator misfolding mutants. *Molecular Biology of the Cell* (2022).
75. Wong, M. Y. & Shoulders, M. D. Targeting defective proteostasis in the collagenopathies. *Current Opinion in Chemical Biology* **50**, 80–88 (2019).
76. DiChiara, A. S. *et al.* Mapping and Exploring the Collagen-I Proteostasis Network. *ACS Chemical Biology* **11**, 1408–1421 (2016).

77. Myllyharju, J. Prolyl 4-hydroxylases, the key enzymes of collagen biosynthesis. *Matrix Biology* **22**, 15–24 (2003).
78. Doan, N. D. *et al.* Elucidation of proteostasis defects caused by osteogenesis imperfecta mutations in the collagen- $\alpha 2(I)$  C-propeptide domain. *J Biol Chem* (2020).
79. Cohen, A. D. & Comenzo, R. L. Systemic Light-Chain Amyloidosis: Advances in Diagnosis, Prognosis, and Therapy. *Hematology* **2010**, 287–294 (2010).
80. Cooley, C. B. *et al.* Unfolded protein response activation reduces secretion and extracellular aggregation of amyloidogenic immunoglobulin light chain. *Proceedings of the National Academy of Sciences* **111**, 13046–13051 (2014).
81. Plate, L. *et al.* Small molecule proteostasis regulators that reprogram the ER to reduce extracellular protein aggregation. *Elife* **5**, (2016).
82. Cooley, C. B. *et al.* Unfolded protein response activation reduces secretion and extracellular aggregation of amyloidogenic immunoglobulin light chain. *Proceedings of the National Academy of Sciences* **111**, 13046–13051 (2014).
83. Hafirassou, M. L. *et al.* A Global Interactome Map of the Dengue Virus NS1 Identifies Virus Restriction and Dependency Host Factors. *Cell Reports* (2017).
84. Welsch, S. *et al.* Composition and Three-Dimensional Architecture of the Dengue Virus Replication and Assembly Sites. *Cell Host & Microbe* **5**, 365–375 (2009).
85. Puerta-Guardo, H. *et al.* Flavivirus NS1 Triggers Tissue-Specific Vascular Endothelial Dysfunction Reflecting Disease Tropism. *Cell Reports* **26**, 1598-1613.e8 (2019).
86. Puschnik, A. S. *et al.* A Small-Molecule Oligosaccharyltransferase Inhibitor with Pan-flaviviral Activity. *Cell Reports* **21**, 3032–3039 (2017).
87. Coyaud, E. *et al.* Global Interactomics Uncovers Extensive Organellar Targeting by Zika Virus. *Molecular & Cellular Proteomics* **17**, 2242–2255 (2018).
88. Shah, P. S. *et al.* Comparative Flavivirus-Host Protein Interaction Mapping Reveals Mechanisms of Dengue and Zika Virus Pathogenesis. *Cell* **175**, 1931-1945.e18 (2018).
89. Gordon, D. E. *et al.* A SARS-CoV-2 protein interaction map reveals targets for drug repurposing. *Nature* **583**, 459–468 (2020).
90. Davies, J. P., Almasy, K. M., McDonald, E. F. & Plate, L. Comparative Multiplexed Interactomics of SARS-CoV-2 and Homologous Coronavirus Nonstructural Proteins Identifies Unique and Shared Host-Cell Dependencies. *ACS Infectious Diseases* **6**, 3174–3189 (2020).
91. Almasy, K. M., Davies, J. P. & Plate, L. Comparative host interactomes of the SARS-CoV-2 nonstructural protein 3 and human coronavirus homologs. *Molecular and Cellular Proteomics* **20**, 100120 (2021).
92. Pankow, S., Bamberger, C. & Yates, J. R. A posttranslational modification code for CFTR maturation is altered in cystic fibrosis. *Science Signaling* **12**, eaan7984 (2019).
93. Cha-Molstad, H. *et al.* Amino-terminal arginylation targets endoplasmic reticulum chaperone BiP for autophagy through p62 binding. *Nature Cell Biology* (2015).

94. Perera, L. A. *et al.* An oligomeric state-dependent switch in the ER enzyme FICD regulates AMPylation and deAMPylation of BiP. *The EMBO Journal* **38**, (2019).
95. Yu, J. *et al.* Phosphorylation switches protein disulfide isomerase activity to maintain proteostasis and attenuate ER stress. *The EMBO Journal* (2020).
96. Ma, Y. & Yates, J. R. Proteomics and pulse azidohomoalanine labeling of newly synthesized proteins: what are the potential applications? *Expert Review of Proteomics* **15**, 545–554 (2018).

## **Interactome Profiling Defines Altered Proteostasis Topology Associated with Thyroid Dyshormonogenesis\***

### **2.1 The Pathology of Tg-Related Congenital Hypothyroidism**

Thyroid hormone biosynthesis is an intricate and multifaceted process involving a sequence of biochemical reactions<sup>1-4</sup>. Triiodothyronine (T3) and thyroxine (T4) hormones are necessary for normal growth and development in utero and early childhood, and go on to regulate primary metabolism in adulthood<sup>5,6</sup>. Hypothyroidism and dyshormonogenesis stemming from mutations or damage to the biosynthetic components ultimately results in decreased or complete loss in production of T3 and T4. Congenital hypothyroidism (CH) affects approximately 1:2000 to 1:4000 newborns, and if not detected and addressed can lead to severe and permanent neurological damage, including mental retardation<sup>7,8</sup>. A critical gene involved in thyroid hormone biosynthesis and CH pathology is thyroglobulin (Tg), encoding the prohormone protein for T3 and T4. There are 167 documented Tg mutations that impair proper production, folding, or processing leading to dyshormonogenesis<sup>5</sup>. Missense mutations resulting in full-length

---

\* This chapter contains material adapted from the published research article: “Thyroglobulin Interactome Profiling Defines Altered Proteostasis Topology Associated With Thyroid Dyshormonogenesis” by Madison T. Wright, Logan Kouba, & Lars Plate, *Molecular & Cellular Proteomics*, Volume 20, 2021, 100008, ISSN 1535-9476. It has been reproduced with the permission of the publisher and co-authors.



but folding-incompetent Tg disrupt normal protein homeostasis (proteostasis) and lead to decreased or complete loss of Tg protein secretion into the thyroid follicular lumen, a key step in hormone production. Instead, mutant Tg variants accumulate within the endoplasmic reticulum (ER) of thyroid follicular cells<sup>9</sup>.

While many CH-associated folding-incompetent Tg mutations have been documented, the molecular mechanisms of Tg folding and processing controlled by the proteostasis network (PN), consisting of chaperones, co-chaperones, folding enzymes, trafficking factors, and degradation factors, remain incompletely understood. Coordination of these PN components ensures the proper folding, trafficking, and degradation of clients such as Tg through a process cumulatively referred to as protein quality control (PQC)<sup>10-12</sup>. Previous studies have shown that CH-associated Tg mutants exhibit increased interactions with individual PN components including HSPA5, HSP90B1, PDIA3, CANX, and CALR, that aid in folding and processing<sup>13-19</sup>. Nonetheless, it remains unclear how these PN components and their respective subnetworks cooperate to mediate proper Tg folding and secretion. Furthermore, identifying which of these components or subnetworks are implicated in the improper processing of mutant Tg has remained elusive. The current collection of known interactors, identified through traditional immunoprecipitation and immunoblotting strategies, is likely limited as these methods are not conducive to discovery-based investigations. Additionally, little work has focused on characterizing mutation specific changes in PN engagement. No disease modifying therapies currently exist to restore secretion of destabilized Tg, but devising such

strategies would be particularly critical considering the increased prevalence of dysmorphogenesis amongst newborns and complications arising from the current “gold standard” of hormone therapy treatments in the clinic<sup>7,20</sup>. Identifying the complete Tg interactome and defining the molecular mechanisms of altered PN engagement for mutant Tg variants may reveal areas of PQC that can be targeted therapeutically to rescue the secretion of these CH-associated variants. Modulation of individual PN components or entire pathways has shown recent promise as a therapeutic strategy to combat a number of protein folding diseases, including light-chain amyloidosis (AL), transthyretin (TTR) amyloidosis, and polyglutamine (polyQ) associated neuropathies<sup>21-24</sup>.

In this chapter, we present a tandem mass tag-based quantitative interactome proteomics method that allowed us to globally profile several CH-associated mutant Tg variants. Compared to other interactome studies<sup>25-27</sup>, the multiplexing capabilities enable a head-to-head comparative analysis of five distinct protein variants. While chaperone complexes and client recognition for select chaperones have been mapped<sup>28-30</sup>, system-wide investigations into PN processing of individual client proteins are lacking. The current study describes the identification of a comprehensive PN interactome for WT Tg and several secretion deficient mutant variants. Comparison of the PN interactome for the CH-associated mutant variants to WT Tg allowed us to gain mechanistic insights into shared PQC defects that are responsible for the loss of secretion of all destabilized variants. Our data supports a model whereby the destabilized Tg variants are retained

intracellularly through increased interactions with chaperoning and oxidative protein folding pathway components. We also find evidence that Tg mutants are increasingly routed towards ER-associated degradation (ERAD), yet exhibit overall lower engagement with proteasomal degradation machinery. Furthermore, we find mutation specific interactome remodeling with components of N-glycosylation and ER lectin protein folding components. Mutant-specific interaction changes suggest that such Tg variants have distinct imbalances associated with their aberrant folding and processing within the ER, leading to the loss of secretion.

## **2.2 Distinct Thyroglobulin Mutants Present Common Secretion Defects**

Tg is a large 330 kDa multidomain protein consisting of extensive cysteine-rich repeat regions and a C-terminal cholinesterase like domain (ChEL) (Figure 2.1A; Figure A.1A and A.1B)<sup>31</sup>. We focused on a set of single-point mutations that lead to impaired Tg secretion in human CH patients (A2234D and C1264R) and in a mouse model of thyroid hormone deficiency and goiter (L2284P)<sup>16,32,33</sup>. A2234D and L2284P occur in the ChEL domain, which serves as an intramolecular chaperone playing a critical role in Tg folding, dimerization, and secretion<sup>34,35</sup>. Our analysis also included a previously uncharacterized ChEL mutation at a conserved glycine (G2341R), which is located

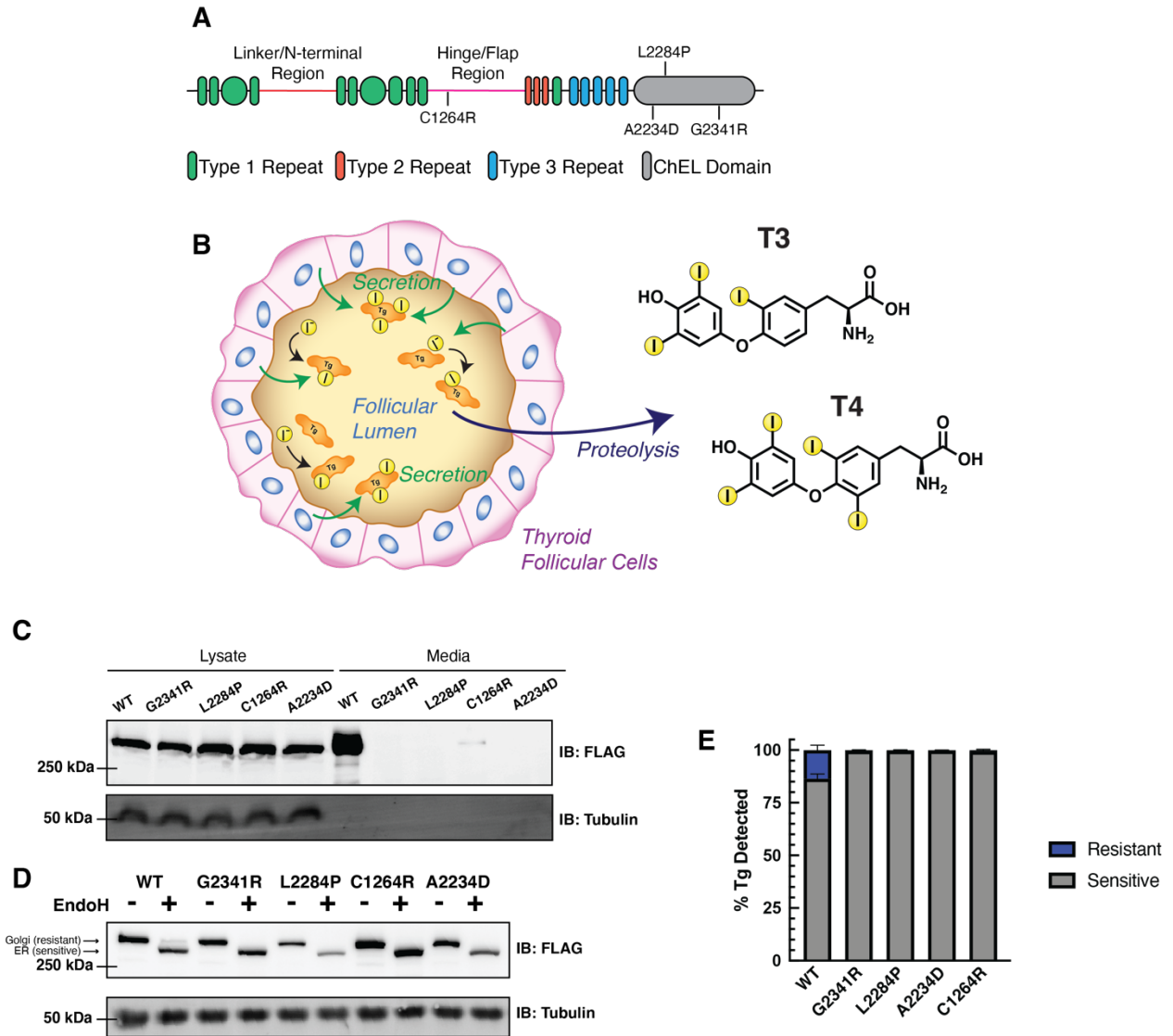


### Figure 2.1: Distinct Tg mutants present secretion defects

(A) Schematic of Tg domain organization consisting of cysteine rich repeats, a linker/N-terminal region, and hinge/flap region followed by a cholinesterase like (ChEL) C-terminal domain.

(B) Schematic detailing Tg processing and subsequent hormone production.

(C) Immunoblot for Flag-tagged Tg expressed in transiently transfected HEK293T cells. All Tg variants are detected in the lysate while only WT is detected in cell culture media.

(D) Western blot for Tg probing EndoH sensitivity to remove high-mannose glycans of ER localized Tg. Golgi associated (resistant) and ER associated (sensitive) bands are indicated by arrows.

(E) Quantification of EndoH sensitivity in (D). All Tg mutants are 100% EndoH sensitive, showing they are retained within the ER and model congenital hypothyroidism.

adjacent to L2284 and A2234. We contrasted the ChEL mutations to the C1264R variant in the hinge/flap region (Figure 2.1A; Figure A.1A – A.1D).

Thyroid hormone production is initiated by the biogenesis and secretion of Tg, which is subsequently iodinated and stored in the thyroid follicular lumen. Once thyrocytes are stimulated, Tg is endocytosed and degraded in the lysosome, leading to the liberation of T3 and T4 hormones (Figure 2.1B). We transiently transfected HEK293T cells with FLAG-tagged expression constructs of either WT or the respective mutant Tg variants. We detected all Tg variants at similar levels in lysate samples, while only WT Tg was detected in the media, confirming the secretion defect of CH mutations (Figure 2.1C). C1264R Tg was occasionally detected at trace amounts in the media indicating low residual secretion (< 1-2% of WT). These results are in accordance with previous Tg studies<sup>16,32,36,37</sup>. WT Tg undergoes extensive glycosylation within the ER prior to being trafficked and further modified in the Golgi apparatus, while the folding-incompetent CH-associated mutations are trapped within the ER preventing Golgi modifications. To investigate Tg localization and glycosylation state we performed EndoH digestions on the transfected HEK293T lysates. All mutants were EndoH sensitive, indicating they had not traversed the medial Golgi apparatus as EndoH specifically cleaves ER associated high-mannose glycans. In contrast, WT Tg separated into two distinct EndoH resistant and EndoH sensitive populations indicating that WT Tg was able to fold within the ER and traverse the secretory pathway (Figure 2.1D and 2.1E). The low level of intracellular EndoH resistant WT Tg indicate that this proteoform gets rapidly secreted. Overall, our results confirm that FLAG epitope tagged Tg constructs do not show altered processing and serve as a useful

model system to probe PQC dynamics for WT and CH-associated, secretion-deficient Tg mutants.

### **2.3 Defining the Tg Proteostasis Interactome**

To identify protein-protein interactions implicated in the aberrant processing of CH-associated mutations, we implemented an affinity purification – mass spectrometry (AP-MS) method coupled with tandem-mass-tag (TMT) labeling to allow for multiplexed identification and quantification of interacting proteins (Figure 2.2A)<sup>38</sup>. Transient interactions between Tg and PN components were captured using the cell-permeable cross-linker dithiobis(succinimidyl propionate) (DSP)<sup>39</sup>. We first sought to define the interactomes for WT Tg and each of the mutant variants (G2341R, L2284P, A2234D, and C1264R). We employed a mock AP using transfection of an untagged WT Tg control construct, or fluorescent proteins (EGFP or tdTomato) to delineate high confidence interactors from background proteins (Figure 2.2A). We further optimized normalization methods and cutoffs to confidently identify interactors pertaining to protein folding, trafficking, and secretion likely to play a role in Tg processing (Figure A.2A and A.2B)<sup>40,41</sup>. We identified interacting proteins for each individual Tg construct (Figure A.2C – A.2H) and defined a cumulative list of 187 confidently identified interactors across all Tg constructs (Figure 2.2B; Figure A.3; Table A.1). We defined this list as the Tg interactome and focused on these proteins for subsequent analyses. Using gene

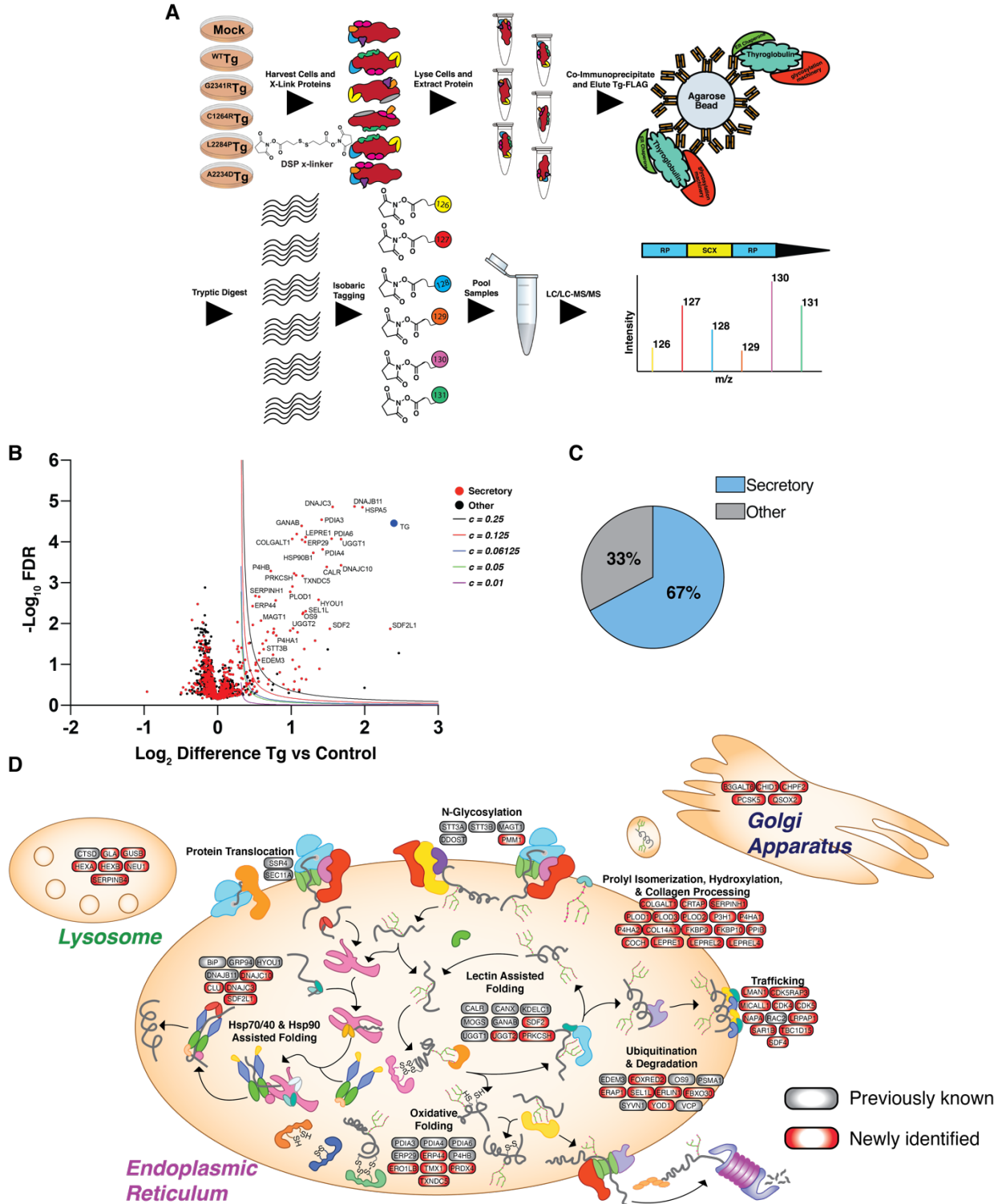


## **Figure 2.2: Defining the Tg interactome using multiplexed quantitative AP-MS**

(A) Schematic detailing the multiplexed quantitative interactomics workflow.

(B) Volcano plot showing TMT enrichment ratios ( $\log_2$  difference all Tg channels versus all mock channels) versus  $-\log_{10}$  false discovery rate (Storey) for coimmunoprecipitated proteins.

(C) Tg interactors are enriched within the secretory pathway.

(D) Schematic detailing newly identified Tg interactors (red) compared to previously published interactors (grey).

ontology (GO) enrichment analysis, 67% of the Tg interactome was enriched in components belonging to PQC within the secretory pathway (Figure 2.2C; Table A.2), including Hsp70/40 and Hsp90 chaperones and co-chaperones, N-glycosylation machinery, glycoprotein folding lectins, components involved in disulfide bond formation, ER-associated degradation (ERAD), as well as lysosomal and Golgi localized proteins<sup>41</sup>. We confirmed that the majority of secretory PQC factors were identified and quantified consistently in the replicate mass spectrometry runs (median identified in 62 % of runs, Figure A.2J).

Our dataset confirms previously known binding partners, such as HSP90B1, HSPA5, PDIA3, CANX, and CALR<sup>13,42</sup>, but it greatly expands the limited list of previous interactors (Figure 2.2D). We identified additional ER Hsp40 co-chaperones, including DNAJC3, DNAJB11, and DNAJC10, that can bind Tg directly and coordinate with the ER Hsp70 chaperone HSPA5 to influence quality control decisions<sup>29,43</sup>. The enrichment in disulfide bond processing components is consistent with a strong dependence on oxidative folding pathways with Tg containing 122 cysteine residues and 61 disulfide bonds<sup>31</sup>. PDIA1, PDIA3, PDIA4, PDIA6 and PDIA9/ERp29 were previously known to associate with Tg<sup>13,14,44</sup>, but we additionally identified PDIA10/ERp44, TXNDC5, and TMX1, among



others (Figure 2.2D). ERAD factors, OS-9, EDEM3, SEL1L, which have been presumed to interact with Tg but not confirmed<sup>4</sup>, along with new factors such as FOXRED2 (Figure 2.2D). Furthermore, we detected previously known and novel interactors involved in glycoprotein folding and processing such as GANAB, LMAN1, UGGT1, as well as other lectins and glycan modifying enzymes. Overall, our analysis validated 28 previously identified Tg interactors and described 160 new PN interactions (Figure 2.2D; Table A.1).

#### **2.4 Secretion Defects of Tg Mutants are Associated with Common Increases in Proteostasis Interactions**

Next, we quantified interaction fold changes for the specific mutants relative to WT Tg to determine what factors may govern the aberrant PQC processing and secretion defects (Figure 2.3A and 2.3B; Figure A.4A and A.4B; Table A.3). Remarkably, when comparing CH-associated mutant interactomes with that of WT, many of the quantified interaction changes were similar across all CH-associated mutants. This held true particularly for factors involved in Hsp70/40 or Hsp90 assisted protein folding, including the Hsp70 and Hsp90 chaperones HSPA5 and HSP90B1 along with co-chaperones DNAJB11 and DNAJC10. We observed similar increases with disulfide/redox-processing enzymes such as protein disulfide isomerases PDIA3, PDIA4, and PDIA6. We validated increased interactions between mutant Tg variants and HSP90B1, HSPA5, PDIA4, PDIA6,

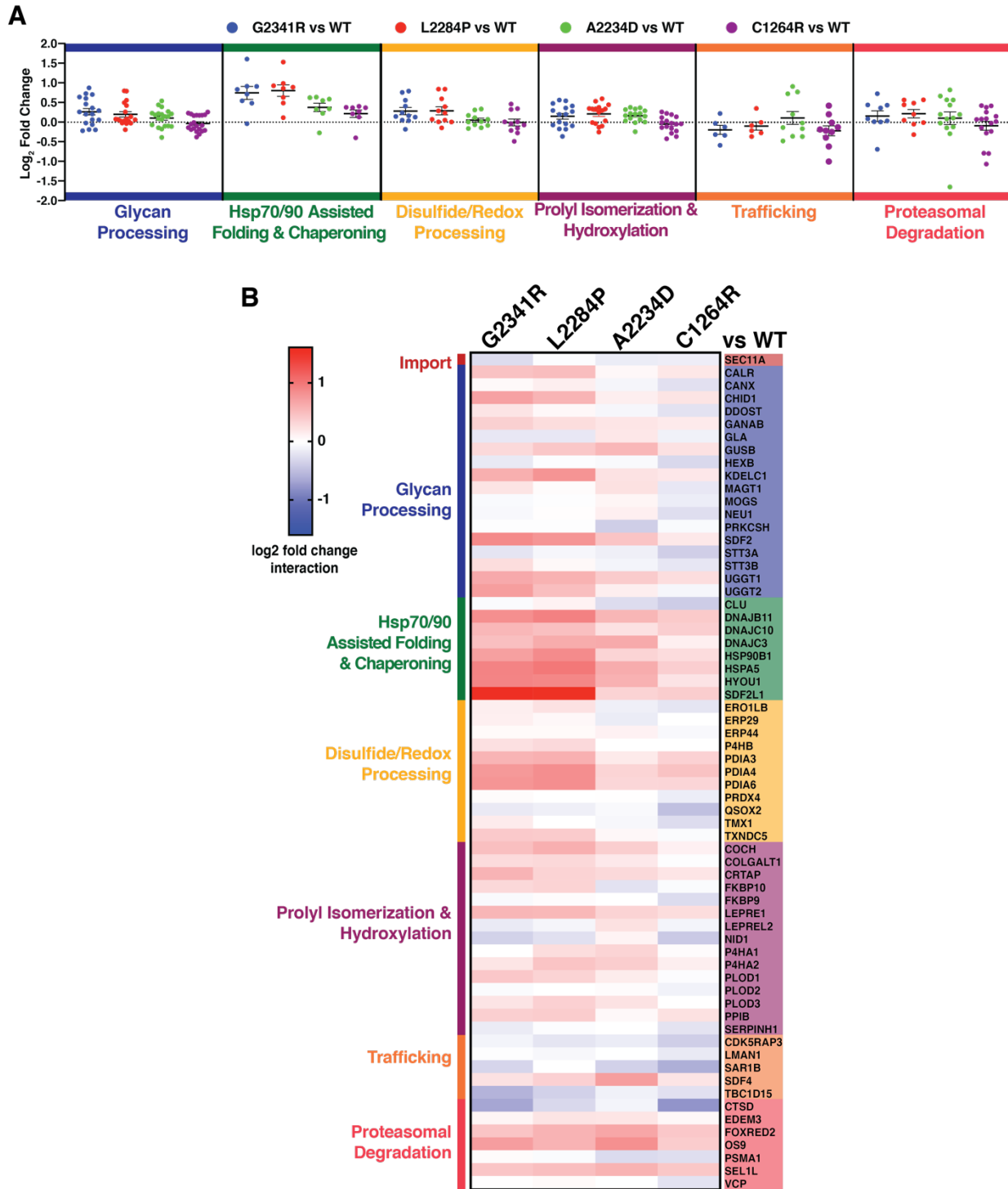


**Figure 2.3: The secretion defect of Tg mutants is associated with both common and mutant specific changes in proteostasis interactions**

(A) Dot plots displaying aggregate interactome changes of proteostasis pathways between the different mutant Tg variants compared to WT.

(B) Heatmap displaying altered interactions of mutant Tg variants with individual proteostasis components.

DNAJC10 by Co-AP followed by quantitative western blot (Figure A.4C – A.4E).

Additionally, the enzymes responsible for marking and directing ER clients for ERAD including EDEM3, FOXRED2, OS9, and SEL1L all showed consistently increased interactions with Tg mutants compared to WT (Figure 2.4A – 2.4D)<sup>45–48</sup>. This observation prompted us to test whether the CH-associated mutant Tg variants are degraded at a higher rate. To monitor potential changes in degradation rates of the Tg constructs we employed a cycloheximide (CHX) chase assay (Figure A.5A). Approximately one third of WT Tg was secreted after 4 hours (Figure A.5B). As previously noted, none of the CH-associated Tg mutants were secreted. When monitoring Tg degradation, all constructs showed similar rates of observed degradation on the scale of 30 – 40% after 4 hours of CHX treatment (Figure 2.4E; Figure A.5B). To ensure that the loss of Tg secretion can be attributed to degradation and does not correspond to aggregated protein, we quantified WT and mutant Tg in the insoluble cell pellet. While a fraction of Tg could be found in the pellet, consistent with prior observation<sup>49,50</sup>, the degree of aggregation remained similar for all variants (Figure A.5C and A.5D). Overall, the degradation rates are consistent with prior studies<sup>51</sup> and indicate that despite increased engagement with ERAD targeting factors, mutant Tg degradation rates are unaffected.

To further investigate why degradation rates remain unchanged for the mutant variants, we next looked at downstream proteostasis factors involved in ERAD after retrotranslocation of proteins into the cytosol. We detected Tg interactions with VCP, the ATPase involved in extracting substrates from the ER, as well as several subunits of the

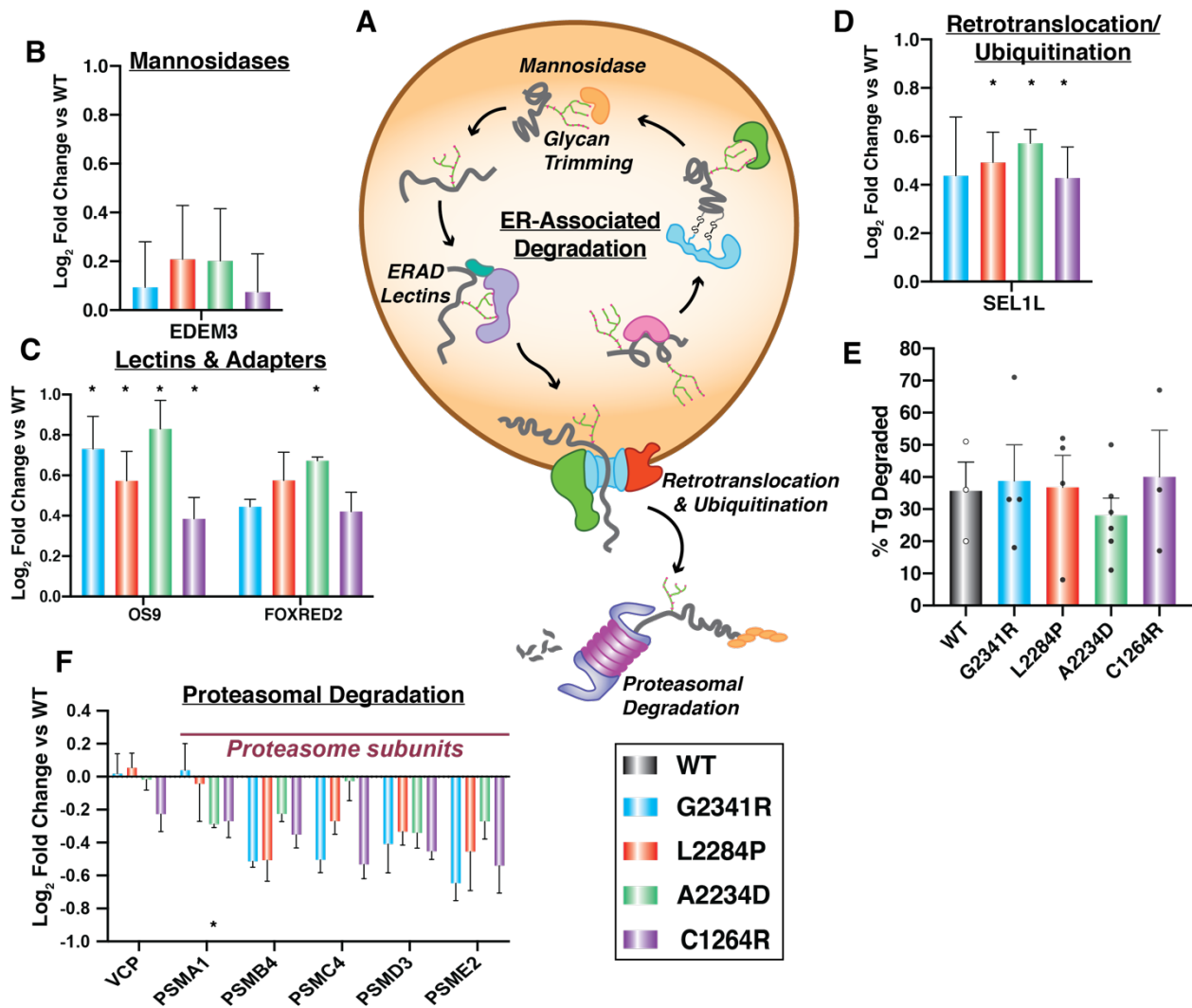


**Figure 2.4: Tg mutants are increasingly routed towards ER-associated degradation machineries but not degraded at faster rates**

(A) Schematic detailing the ERAD pathway for glycoproteins.

(B–D) Interaction changes of Tg mutants compared to WT with individual ERAD factors.

(E) Plot showing the percentage of Tg degraded measured in HEK293<sup>DAX</sup> cells after 4 (F) Interaction changes of Tg mutants compared to WT for cytosolic proteins involved in proteasome-mediated protein degradation.

proteasome (Figure 2.4A and 2. 4F). Interactions between Tg mutant variants and VCP

are mostly unchanged relative to WT, and proteasome subunits were consistently

decreased for all mutants. This reduced engagement of CH-associated Tg mutants with

the degradation machinery may provide an explanation why these variants are not

degraded to a larger extent despite their increased targeting to glycoprotein ERAD

relative to WT.

Overall, the interactomics data suggest that CH-associated mutant Tg display common PQC defects linked to prolonged chaperoning facilitated largely by Hsp70/40, Hsp90, and disulfide/redox folding pathways, as well as increased associations with ER luminal ERAD components. Interestingly, in many cases interaction fold changes were slightly higher for all ChEL domain Tg mutants, G2341R, L2284P, and A2234D than for the C1264R mutant occurring in the hinge/flap region (Figure 2.3B; Table A.3). This parallels our and previous secretion data exhibiting residual C1264R-Tg secretion (Figure 2.1C) and suggests that the Tg PQC defects are more profound when mutations occur in the ChEL domain<sup>37</sup>.

## **2.5 CH-associated Tg Exhibits Mutation Specific Changes in Engagement with the ER-Lectin Chaperone Network**

While identifying common changes in PN interactions across CH-associated mutants provides new insights on conserved Tg processing mechanisms, we wanted to further explore the data to investigate whether any mutation-specific PN interaction changes occurred that may define unique PQC defects associated with each mutation. We detected significant and distinct deviations across CH-associated Tg interactions with PN components involved in N-glycosylation, and the CANX/CALR lectin folding pathway (Figure 2.5A – 2.5E). Interactions with CALR, the soluble paralog of CANX, were significantly increased for G2341R and L2284P relative to WT Tg, but not for C1264R

and A2234D. PDIA3, the protein disulfide isomerase family member known to specifically complex with either CANX or CALR, exhibited similarly increased interactions with G2341R and L2284P<sup>52,53</sup> (Figure 2.5B). Significantly increased interactions for all mutations were also observed for the glucosyltransferase UGGT1, as well as GANAB (Figure 2.5C and 2.5D). GANAB and UGGT1 act as the gatekeepers for glycoprotein folding. As GANAB sequentially cleaves the two innermost glucose residues of the ER associated N-linked oligosaccharide precursor, regulating initial client entry and exit from the CANX/CALR lectin folding pathway, UGGT1 re-glycosylates misfolded ER glycoprotein clients, regulating their re-entry into the CANX/CALR lectin folding pathway (Figure 2.5A)<sup>53,54</sup>.

While the lectin folding pathway is of clear importance, these interactions occur downstream of the oligosaccharyl transferase (OST) complex which facilitates N-glycosylation of proteins<sup>55</sup>. We hypothesized that the observed changes in ER lectin chaperone network engagement could stem from altered engagement with the OST complex. We noticed mutation specific changes in engagement with the two different OST isoforms. In one isoform containing the catalytic STT3A subunit, the OST is largely associated with the translocon and facilitates co-translational glycosylation of ER client proteins<sup>56</sup>. The other OST isoform containing STT3B is largely associated with post-translational glycosylation of ER client proteins<sup>56</sup>. Most CH-associated Tg mutants

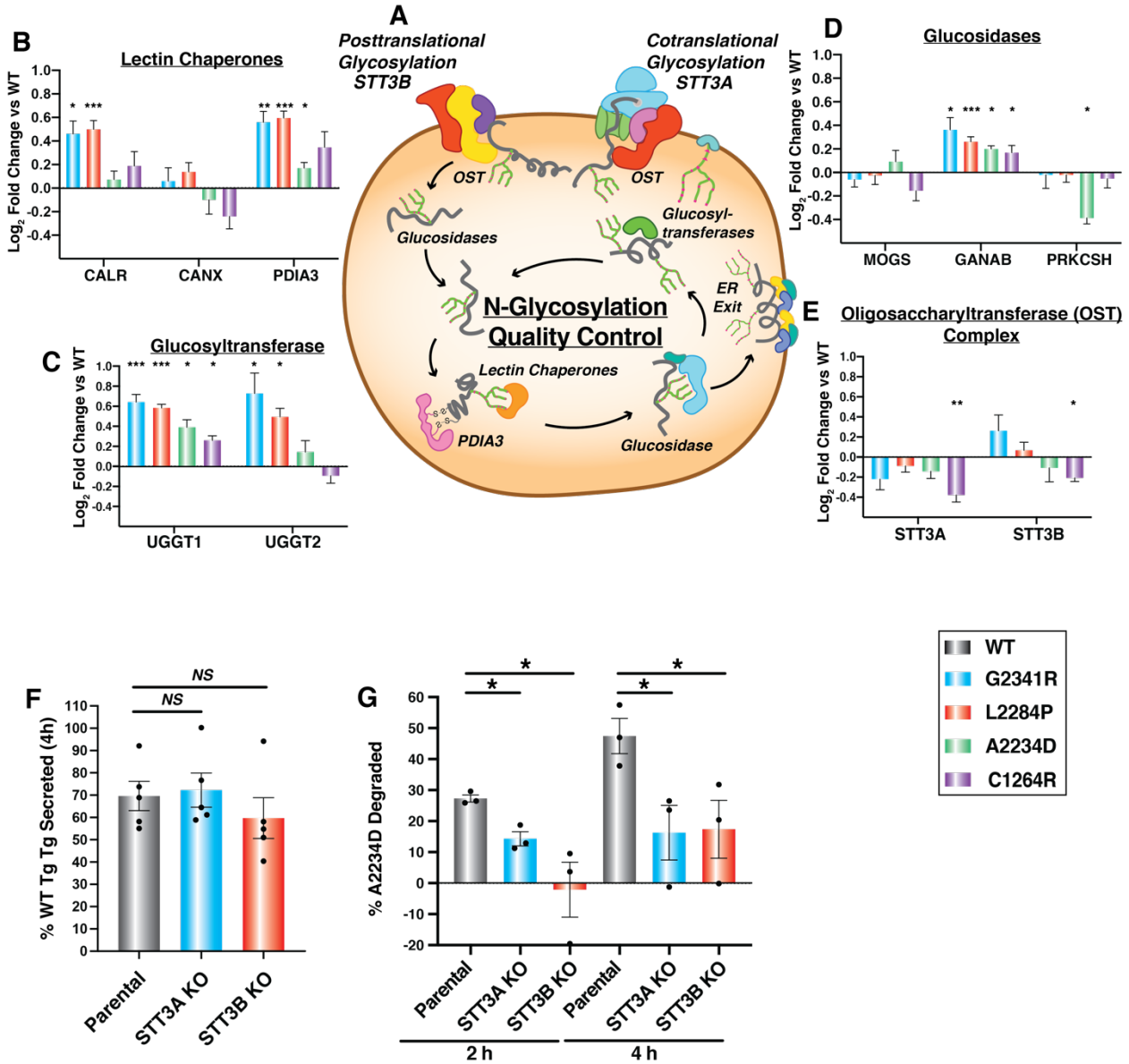


**Figure 2.5: Perturbation of N-linked glycosylation distinctly impacts A2234D Tg**

(A) Schematic detailing the N-glycosylation and lectin-mediated folding pathway.

(B–E) Interaction changes of Tg mutants compared to WT with individual N-glycosylation quality control factors.

(F) Comparison of WT Tg secretion in parental, STT3A, or STT3B KO HEK293T cells.

(G) Comparison of A2234D Tg degradation in parental, STT3A, or STT3B KO HEK293T cells.

showed varying degrees of decreased interactions with the STT3A catalytic subunit relative to WT. In contrast, interaction changes with STT3B were divergent for mutant

variants relative to WT Tg. G2341R and L2284P exhibited modestly increased or unchanged interactions while A2234D and C1264R showed decreased interaction (Figure 2.5E). We confirmed by Co- AP Western blot that A2234D and C1264R displayed decreased interactions with STT3B compared to WT and that these changes were distinct from G2341R and L2284P (Figure A.6A). Overall, our findings reveal mutation specific PQC defects for the different CH-associated Tg mutants and their engagement and processing through the CANX/CALR lectin folding pathway. These changes may stem from subtle differences in engagement with the upstream OST complex, which mediates the entry in the CANX/CALR lectin folding pathway (Figure 2.5A).

## **2.6 Perturbation of N-Linked Glycosylation Distinctly Impacts A2234D Tg**

Tg contains 17 N-glycosylation sites and therefore depends heavily on the lectin-folding pathway, but little investigation has been dedicated to understanding how OST engagement, particularly in the case of CH-associated mutations, may affect downstream Tg processing<sup>4</sup>. Therefore, we chose to focus on elucidating the role of the two different STT3A and STT3B dependent OST isoforms on downstream Tg processing. Individual glycosylation sites on protein clients display varying specificity towards glycosylation by either STT3A, STT3B, or both isoforms of the OST<sup>57</sup>. Specific OST isoform dependencies for Tg N-glycosylation are not well studied, further motivating our investigation into the changes in OST engagement and downstream processing observed for CH-associated mutants. To assess the functional implications of these changes with



OST engagement identified in our dataset, we monitored the effects of isoform-specific knockouts of STT3A or STT3B OST isoforms on Tg secretion and degradation<sup>56–58</sup>. We transfected Tg variants into HEK293T STT3A<sup>-/-</sup> and STT3B<sup>-/-</sup> knockout cell lines and monitored protein levels in the media and the lysate under steady-state conditions. Knockout of either OST subunit did not abolish WT Tg secretion nor rescue secretion of any CH mutants (Figure A.6B).

Next, we followed Tg processing via cycloheximide (CHX) chase assay and <sup>35</sup>S pulse-chase labeling to measure secretion and degradation rates (Figure A.5A; Figure A.6C). STT3A and STT3B knockout led to a small decrease in the WT Tg secretion rates when measured via CHX assay (Figure A.6D and A.6E). We then went on to quantify the degradation of CH-associated mutants (Figure A.6D and A.6F). Given the high variability in degradation measurements using the CHX chase assay, we employed the <sup>35</sup>S pulse-chase labeling workflow to mitigate any complications resulting from inhibiting protein synthesis (Figure A.6G and A.6H). We focused on A2234D Tg as this mutation is proximal to two N-glycosylation sequons found in the ChEL domain known to act as an intramolecular chaperone<sup>15,35</sup>. We hypothesized that A2234D may alter the engagement of these sequons with the OST complex, altering Tg glycosylation and downstream processing. When measured using the <sup>35</sup>S assay, STT3A and STT3B KO cells did not alter WT Tg secretion (Figure 2.5F; Figure A.6G). In contrast, STT3A and STT3B KO cells significantly attenuated degradation for A2234D Tg. The fraction of degraded A2234D Tg recovered from 50% to 20% 4 hours after synthesis (Figure 2.5G; Figure A.6H). In

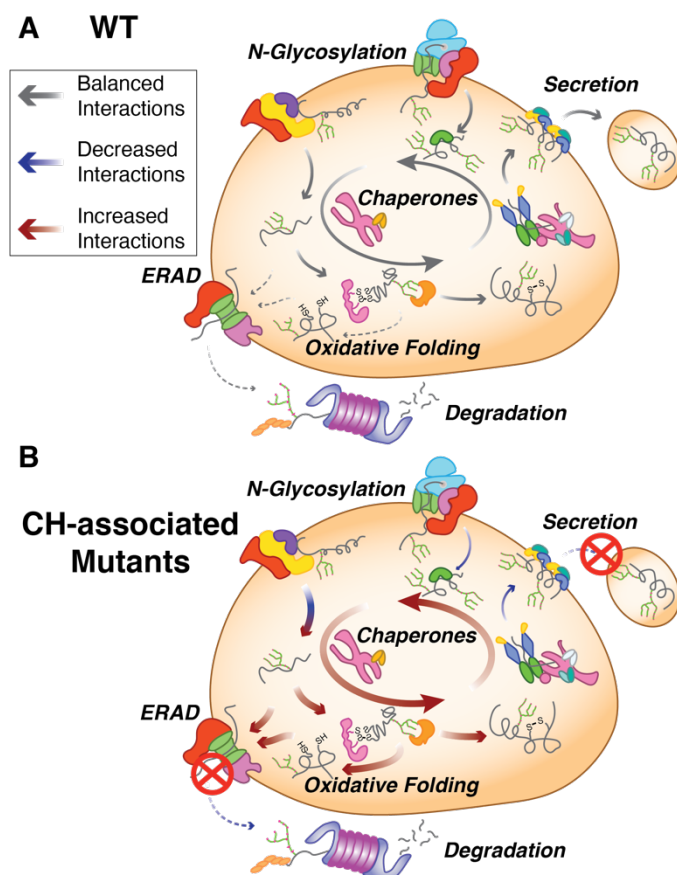
contrast, STT3A or STT3B KOs did not significantly alter WT Tg degradation rates (Figure A.6G and A.6I). These results suggest that in the case of A2234D, engagement with both OST isoforms is necessary for proper entry into the CANX/CALR lectin folding pathway, resulting in degradation initiated by glycoprotein quality control within the ER.

## 2.7 Discussion and Conclusions

Most CH-associated Tg missense mutant variants present with very similar phenotypes resulting in inefficient trafficking and loss of secretion. The majority of the CH mutant variants presented here have been reported to be retained within the ER and interact with canonical PN components. Furthermore, L2284P and C1264R have been reported to activate the unfolded protein response (UPR), which acts to adjust ER quality control capacity in response to ER stress<sup>14,21</sup>. UPR activation has also been speculated but not validated for A2234D<sup>33</sup>. However, there has been little investigation into 1) identifying molecular mechanisms involved in the inefficient folding and trafficking of these mutant proteins, and 2) developing or exploring therapeutic avenues aimed at rescuing the secretion and subsequent hormone production from these mutants<sup>9,13,14,16,33,36,59</sup>. Here we utilized a multiplexed quantitative interactomics platform to describe the PN dependencies of several CH-associated Tg variants with mutations clustering in two different domains of Tg. Our analysis of Tg interactomes reveals common PQC defects that are involved in the loss of Tg secretion, but we also identify unique dependencies that may suggest PQC mechanisms that are specific to individual mutations.

Besides previous documented Tg interactors such as HSPA5, HSP90B1, CANX, CALR, and PDIA3, the quantitative interactomics profiling greatly expand our knowledge of additional cochaperones, lectins, trafficking and degradation factors that influence PQC activity and subsequent Tg processing. Previous work has provided insights on the implications of some of these interactions as HSPA5 overexpression decreases WT Tg secretion<sup>60</sup>. Additionally, our analysis identified a number of Hsp40 co-chaperones, which can direct chaperone pathways to assume pro-folding or pro-degradation roles<sup>29,61</sup>. The iterative binding cycles between Tg with HSPA5 and co-chaperones likely results in overall increased retention of Tg and therefore blocks partitioning of Tg to necessary trafficking components<sup>62</sup>. PDIA4 has also been identified as a key interactor as it has been shown to bind mutant Tg and form coaggregates retained within the ER<sup>13</sup>. We identified increased interaction between PDIA4 and all secretion deficient Tg mutants in this study, but we also identified stronger engagement with many other protein disulfide isomerase protein family members and factors involved in oxidative protein folding. Several PDI family members were previously shown to form transient mixed-disulfide-linked intermediates with Tg, highlighting their involvement in Tg folding<sup>13,14,44</sup>. The increased interactions with these PDIs and additional factors involved in disulfide bond formation may be responsible for intracellular retention and co-aggregation with destabilized Tg variants, which may be mediated through non-resolved mixed-disulfide bond intermediates<sup>13,50</sup>.

Our results show that the CH-associated Tg mutants not only engage many of the chaperoning and oxidative protein folding pathways to a greater extent, but also show altered interactions with ERAD and N-glycosylation components that may be responsible for retention and/or aggregation within the ER (Figure 2.6). Prior work has shown that ERAD of Tg is suppressed upon the inhibition of mannosidase I (MAN1B1)<sup>51</sup>. MAN1B1 is known to trim the outermost alpha-1,2-linked mannose residue of the high-mannose ER-associated glycan, followed by subsequent trimming of inner mannose residues, a key step within the glycoprotein ERAD process<sup>63</sup>. While we did not identify MAN1B1 in our dataset, other mannosidases of the ER degradation enhancing alpha-mannosidase like (EDEM) family associated with ER stress and UPR activation were identified in the current study<sup>64,65</sup>. These factors exhibited predominantly increased interactions with CH-



associated mutants relative to WT Tg, along with accessory proteins such as

**Figure 2.6: Model for common and mutant-specific proteostasis interactome changes mediating the secretion defect of CH-associated Tg variants**

(A) WT Tg processing is facilitated by proper chaperoning, post-translational modification and trafficking is maintains secretion, and subsequent hormone production.

(B) Tg mutant processing exhibits imbalances through increased chaperoning and engagement with oxidative folding enzymes, possibly stemming from altered engagement with the OST complex dominates processing.

SEL1L, FOXRED2, OS-9, and other vital glycoprotein ERAD components<sup>30,45,48</sup>. Considering that mutant Tg variants were not degraded to a greater extent than WT Tg, this increased targeting to ERAD factors seems to be uncoupled from actual proteasomal degradation<sup>66</sup>. Ultimately, Tg must be degraded as indicated by prior work and from our CHX and pulse-chase experiments, possibly through a mixture of ERAD activity and autophagy<sup>13,51</sup>. Consistent with this, we identified a number of lysosomal protein factors (Figure 2.2D; Figure A.7). Consequently, further investigations into the degradation components and pathways facilitating Tg degradation would be of interest to examine, particularly cross talk and timing between ERAD and ER-phagy<sup>12,61,67-69</sup>.

The identification of altered interactions between CH-associated Tg variants and the components of the OST complex involved in protein N-glycosylation provides new insights into the distinct misprocessing defects for individual CH-associated Tg mutants. While the disruptions in OST complex interactions do not completely explain why these Tg mutants are unable to exit the ER, these changes occur for the most upstream enzymes mediating Tg post-translational processing suggesting an important effect. Furthermore, subtle changes in glycosylation patterns could have profound influences on binding of lectin-chaperones, glycan processing enzymes, or lectin-associated oxidoreductases<sup>52-54,70</sup>.

The changes in PN engagement could be a consequence of changes in Tg secondary and tertiary structure of folding intermediates that then lead to altered engagement with

the OST complex. Changes in secondary structure have been loosely predicted for some Tg mutants including extension or reduced stretch of  $\alpha$ -helix or  $\beta$ -sheet structure, along with the formation of a  $\beta$ -sheet<sup>71</sup>. Interestingly, the cryo-EM structure of Tg showed that the three mutations, A2234D, L2284P, and G2341R cluster into a small region of the ChEL domain, suggesting that all three mutations could destabilize the structure at a similar location (Figure A.2B). Despite this co-localization, the ChEL mutants displayed several distinct interactome changes and only A2234D degradation could be rescued by knockout of individual OST isoforms. The same cryo-EM structure also revealed that a glycosylation site at N2013 may play a key role in stabilizing the Tg dimer<sup>31</sup>. Investigations into which OST complex is responsible for N2013 glycosylation and how these ChEL domain mutations may change the glycan occupancy would be of particular interest. On the other hand, the C1264R mutation is localized distantly from the ChEL domain in the hinge/flap region, presumably disrupting a local disulfide bond with C1245 and resulting in structurally distinct folding defects (Figure A.1D). Nonetheless, interaction changes with the PN for C1264R are largely similar to the ChEL domain mutants, albeit to a lower magnitude, highlighting those mutations in distinct regions of the protein can produce common PQC deficiencies that result in loss of protein secretion. Additionally, disulfide bond formation and N-glycosylation are competing reactions within the ER, further complicating Tg processing<sup>72</sup>.

While PQC pathways are unable to facilitate complete folding and secretion of the Tg mutants, folding and processing is clearly attempted prior to degradation taking place. It

may be the case for A2234D Tg, that in the absence of either STT3A or STT3B in the KO cells, proper entry into the lectin-folding cycle is disrupted, ultimately leading to retention within the ER and decreased degradation. The decreased degradation rate may stem from an inability of the PN to recognize A2234D Tg for glycoprotein ERAD due to aberrant glycosylation, or aberrant glycosylation may lead to the preferential aggregation of A2234D Tg, allowing it to escape ERAD<sup>53,61</sup>. Overall, our results highlight that altered proteostasis interactions with Tg variants can have subtle, yet significant functional outcomes that are specific to localization and nature of the destabilizing mutation. The cryo-EM structure of human Tg and future structural studies on mutant Tg variants could enable further insights into what structural changes influence the engagement of proteostasis factors<sup>31</sup>.

The modulation of PN components or entire pathways has shown recent promise as a therapeutic strategy to combat a number of protein folding diseases<sup>21,22,24,73,74</sup>. By using quantitative multiplexed interactome proteomics, we identified specific PN components that may act as therapeutic targets for rescuing Tg secretion. A similar method has been used to investigate the molecular basis of activating transcription factor 6 (ATF6) dependent regulation of immunoglobulin light chain secretion in (AL) amyloidosis<sup>38</sup>. Methods to pharmacologically target the UPR may be further applicable to rescuing Tg secretion. Many of the CH-associated mutations presented here naturally activate the UPR<sup>9,14,33</sup>. Therefore, pharmacologic modulation of UPR activity to regulate the abundance of ER proteostasis factors in a coordinated manner could act to restore mutant

Tg secretion. In the case of amyloidogenic light chain proteins, overexpression of UPR-regulated chaperones, in particular HSPA5 and HSP90B1, was able to reduce the secretion of an aggregation-prone protein variant<sup>23,38</sup>. Similar effects were also observed for a model aggregation-prone polyQ protein as cytosolic heat shock activation attenuated intracellular aggregation, and cellular toxicity<sup>73</sup>. In contrast, the increased surveillance of destabilized Tg variants by chaperoning and oxidative folding pathways are likely directly implicated in the loss of protein secretion. Here, UPR activation potentially further exacerbates the secretion defects for Tg mutants by increasing the abundance of relevant PN components and promoting increased intracellular interactions. Consequently, reducing the engagement between mutant Tg variants and the identified chaperoning, oxidative folding, and ERAD targeting pathways could be a viable strategy to restore mutant Tg secretion<sup>21,75,76</sup>. Our quantitative proteostasis interactome map forms the framework for the identification of single PN components or entire pathways as viable drug targets geared towards rescuing Tg secretion. Future studies directed at disrupting the individual protein interactions or reducing PN capacity in a coordinated manner through pharmacologic inhibition of UPR signaling pathways could reveal the impact on rescue of CH-associated mutant Tg secretion.

## **2.8 Acknowledgements**



We thank Dr Renã Robinson (Vanderbilt University) for the use of mass spectrometry resources and Dr Reid Gilmore (University of Massachusetts Medical Center) for providing STT3A and STT3B knockout cell lines.

This work was funded by the Vanderbilt Institute of Chemical Biology Fellowship, Vanderbilt Chemistry-Biology Interface Training Program (NIGMS, 5T32GM065086), National Science Foundation Graduate Research Fellowship Program (M. T. W.), and an NIGMS R35 award (1R35GM133552). The content is solely the responsibility of the authors and does not necessarily represent the official views of the National Institutes of Health.

M. T. W. and L. P. designed experiments. M. T. W., L. K., and L. P. performed experiments and analyzed data.

## **2.9 Experimental Methods**

### *2.9.1 Plasmids and Antibodies*

FLAG-tagged (FT)-Tg in pcDNA3.1+/C-(K)-DYK plasmid was purchased from Genscript (Clone ID OHu20241). Site-directed mutagenesis was then performed to generate FT-G2341R, FT-L2284P, FT-C1264R, FT-A2234D, and untagged Tg plasmids (Table A.4). Primary antibodies were acquired from commercial sources and used at the indicated

dilutions in immunoblotting buffer (5% bovine serum albumin (BSA) in Tris-buffered saline pH 7.5, 0.1% Tween-20, and 0.1% sodium azide). Mouse monoclonal antibodies were used for the detection of KDEL (1:1000, Enzo Life Sciences, ADI-SPA-827), M2 anti-FLAG (1:1000, Sigma Aldrich, F1804). Polyclonal rabbit antibodies were used to detect HYOU1 (1:1000, GeneTex, GTX102255), PDIA6 (1:1000, GeneTex, 121275) PDIA4 (1:1000, Proteintech, 14712-1-AP) DNAJC10 (1:500, Proteintech, 13101-1-AP), thyroglobulin (1:1000, Proteintech, 21714-1-AP), UGGT1 (1:1000, Proteintech, 14170-1-AP). STT3A (1:2000, Proteintech, 12034-1-AP) and STT3B (1:2000, Proteintech, 15323-1-AP). Secondary antibodies were obtained from commercial sources and used at the indicated dilutions in 5% milk in Tris-buffered saline pH 7.5, 0.1% Tween-20 (TBS-T): Goat anti-mouse Starbright700 (1:10000, Bio-Rad,12004158), Goat anti-rabbit IRDye800 (1:10000, LI-COR, 926-32211), Goat anti-rabbit Starbright520 (1:10000, Bio-Rad,12005869).

### *2.9.2 Cell Culture and Transfections*

HEK293<sup>DAX</sup> cells<sup>77</sup>, HEK293T, and STT3A or STT3A KO HEK293T cells<sup>57</sup> were grown in Dulbecco's modified Eagle's medium (DMEM) supplemented with 10 % fetal bovine serum (FBS), 1% L-glutamine (200mM), 1% penicillin (10,000U) / streptomycin (10,000  $\mu$ g/mL). Cells were transiently transfected with respective FT Tg expression plasmids using a calcium phosphate method.

### *2.9.3 Affinity Purification and MS Sample Preparation*

A fully confluent 10cm tissue culture plate (approximately  $10^7$  cells) was used per condition. Cells were harvested by washing with PBS and incubating with 1mM EDTA in PBS on ice. A cell scraper was then used to dislodge cells. Cells were harvested, washed once with PBS, and treated with 0.5mM dithiobis(succinimidyl propionate) (DSP) (Thermo Scientific, PG82081) in PBS for 30 minutes at room temperature while rotating. Crosslinking was quenched by addition of 100mM Tris pH 7.5 for 15 minutes. Lysates were prepared by lysing in RIPA buffer (50mM Tris pH 7.5, 150mM NaCl, 0.1% SDS, 1% Triton X-100, 0.5% deoxycholate and protease inhibitor cocktail (Roche, 4693159001) and protein concentration was normalized. Cell lysates were then precleared on 4B sepharose beads (Sigma, 4B200) at 4°C for 1 hour while rocking. Precleared lysates were immunoprecipitated with M2 anti-flag agarose resin (Sigma, A2220) or G1 Anti-DYKDDDDK affinity resin (GenScript, L00432) overnight at 4°C while rocking. Resin was washed four times with RIPA buffer, and proteins were eluted twice in 75uL elution buffer (2% SDS, 1mM EDTA, in PBS) by heating at 95°C for 5 minutes. Eluted samples were precipitated in methanol/chloroform, washed three times with methanol, and air dried. Protein pellets were then resuspended in 3uL 1% Rapigest SF Surfactant (Waters, 186002122) followed by the addition of 10uL of 50mM HEPES pH 8.0, and 32.5uL of H<sub>2</sub>O. Samples were reduced with 5mM tris(2-carboxyethyl)phosphine (TCEP) (Sigma, 75259) at room temperature for 30 minutes and alkylated with 10mM iodoacetimide (Sigma, I6125) in the dark at room temperature for 30 minutes. 0.5  $\mu$ g of Trypsin (Promega, V511A

or Thermo Scientific, PI90057) was then added and incubated for 16-18 hours at 37°C, shaking at 700rpm. Peptides were reacted with TMT sixplex reagents (Thermo Fisher, 90066) in 40% v/v acetonitrile and incubated for one hour at room temperature. Reactions were quenched by the addition of ammonium bicarbonate (0.4% w/v final concentration) and incubated for one hour at room temperature. TMT labeled samples for a given experiment were then pooled and acidified with 5% formic acid (Fisher, A117, v/v). Samples were concentrated using a speedvac and resuspended in buffer A (95% water, 4.9% acetonitrile, and 0.1% formic acid, v/v/v). Cleaved Rapigest SF surfactant was removed by centrifugation for 30 minutes at 21,100 x g.

#### *2.9.4 Liquid Chromatography – Tandem Mass Spectrometry*

MudPIT microcolumns were prepared as previously described<sup>78</sup>. Peptide samples were directly loaded onto the columns using a high-pressure chamber. Samples were then desalted for 30 minutes with buffer A (95% water, 4.9% acetonitrile, 0.1% formic acid v/v/v). LC-MS/MS analysis was performed using a Q-Exactive HF (Thermo Fisher) or Exploris480 (Thermo Fisher) mass spectrometer equipped with an Ultimate3000 RSLCnano system (Thermo Fisher). MudPIT experiments were performed with 10 $\mu$ L sequential injections of 0, 10, 30, 60, and 100% buffer C (500mM ammonium acetate in buffer A), followed by a final injection of 90% buffer C with 10% buffer B (99.9% acetonitrile, 0.1% formic acid v/v) and each step followed by a 130 minute gradient from 5% to 80% B with a flow rate of either 300 or 500nL/minute on a 20cm fused silica

microcapillary column (ID 100  $\mu\text{m}$ ) ending with a laser-pulled tip filled with Aqua C18, 3 $\mu\text{m}$ , 100  $\text{\AA}$  resin (Phenomenex). Electrospray ionization (ESI) was performed directly from the analytical column by applying a voltage of 2.0 or 2.2kV with an inlet capillary temperature of 275°C. Using the Q-Exactive HF, data-dependent acquisition of mass spectra was carried out by performing a full scan from 300-1800 m/z with a resolution of 60,000. The top 15 peaks for each full scan were fragmented by HCD using normalized collision energy of 38, 0.7 m/z isolation window, 120 ms maximum injection time, at a resolution of 15,000 scanned from 100 to 1800 m/z and dynamic exclusion set to 60s. Using the Exploris480, data-dependent acquisition of mass spectra was carried out by performing a full scan from 400-1600m/z at a resolution of 120,000. Top-speed data acquisition was used for acquiring MS/MS spectra using a cycle time of 3 seconds, with a normalized collision energy of 36, 0.4m/z isolation window, 120ms maximum injection time, at a resolution of 30,000 with the first mass (m/z) starting at 110. Peptide identification and TMT-based protein quantification was carried out using Proteome Discoverer 2.3 or 2.4. MS/MS spectra were extracted from Thermo Xcalibur .raw file format and searched using SEQUEST against a Uniprot human proteome database (released 03/2014 and containing 20337 entries). The database was curated to remove redundant protein and splice-isoforms, and supplemented with common biological MS contaminants. Searches were carried out using a decoy database of reversed peptide sequences and the following parameters: 10ppm peptide precursor tolerance, 0.02 Da fragment mass tolerance, minimum peptide length of 6 amino acids, trypsin cleavage with a maximum of two missed cleavages, dynamic methionine modification of 15.995 Da

(oxidation), static cysteine modification of 57.0215 Da (carbamidomethylation), and static N-terminal and lysine modifications of 229.1629 Da (TMT sixplex).

### 2.9.5 Experimental Design and Statistical Rationale

A total of 13 6plex TMT LC-MS/MS runs were analyzed for this study. Biological replicate Co-IP samples for the individual Tg variants were spread out across these TMT channels in these 13 batches so that each variant was directly paired against one another at minimum four times. Each run included at least one mock IP control. In total, the analysis included 15 biological replicates for control and WT Tg samples, 12 biological replicates for L2284P and G2341R Tg samples, and 6 biological replicates for A2234D Tg samples. SEQUEST search results were filtered using Percolator to minimize the peptide false discovery rate to 1% and a minimum of two peptides per protein identification. TMT reporter ion intensities were quantified using the Reporter Ion Quantification processing node in Proteome Discoverer 2.3 or 2.4 and summed for peptides belonging to the same protein, including razor peptides.

To identify true interactors from non-specific background TMT intensities first underwent a  $\log_2$  transformation, were then median normalized using the formula:  $I_{n,TMT\alpha}^{norm} =$

$$I_{n,TMT\alpha}^{unnorm} \cdot \frac{\sum_{TMT\gamma}^{TMT\alpha} \mathcal{M}}{\mathcal{M}_{TMT\alpha}}.$$

Here,  $I_{n,TMT\alpha}^{norm}$  and  $I_{n,TMT\alpha}^{unnorm}$  are the unnormalized and normalized TMT

intensities for a given protein  $n$  found in TMT channels  $\alpha$ - $\gamma$ , and  $\mathcal{M}$  is the median TMT intensity value for TMT channels  $\alpha$ - $\gamma$ . TMT ratios were then calculated between respective

Tg AP and control TMT channels using formula:  $\log_2 I_{n,TMT\alpha}^{norm} - \log_2 I_{n,TMT\gamma}^{norm}$  (Supplemental Fig. S1A-B). The mean of  $\log_2$  interaction differences was then calculated across the multiple LC-MS batches consisting of 15 biological replicates for control and WT Tg samples, 12 biological replicates for L2284P and G2341R Tg samples, and 6 biological replicates for A2234D Tg samples. Significance of interaction differences were calculated using a paired, parametric, two tailed t-test of  $\log_2 I_{n,TMT\alpha}^{norm}$ , and multiple testing correction was carried out via FDR estimation<sup>79</sup>. A previously described method was used to designate true interactors from non-specific background<sup>40</sup>. In short, the function  $y = c/(x - x_0)$  was used, where  $c$  = curvature and  $x_0$  = minimum fold change, set as one standard deviation of the  $\log_2$  interaction differences of the respective Tg variant compared to the mock AP. The  $c$  parameter was optimized to separate true interactors from false positives (Fig. S2.1D-S2.1H). Tg interactors were identified for WT and mutant Tg individually. A cumulative list of identified interactors was then used for WT vs mutant Tg comparisons.

To compare WT vs mutant Tg interactors, TMT intensities were first normalized using

formula:  $I_{n,TMT\alpha}^{norm} = I_{n,TMT\alpha}^{unnorm} \cdot \frac{\sum_{TMT\gamma}^{TMT\alpha} I_{Tg}^{unnorm}}{I_{Tg,TMT\alpha}^{unnorm}}$ . Here,  $I_{n,TMT\alpha}^{norm}$  and  $I_{n,TMT\alpha}^{unnorm}$  are the unnormalized

and normalized TMT intensities for a given protein  $n$  found in TMT channels  $\alpha$ - $\gamma$ , and

$I_{Tg}^{unnorm}$  is the unnormalized TMT intensity value for Tg in a given TMT channel  $\alpha$ - $\gamma$ .

Significance of interaction differences was calculated using a paired, parametric, two

tailed t-test of  $\log_2 I_{n,TMT\alpha}^{norm}$ , and multiple testing correction was carried out via FDR

estimation<sup>79</sup>. The dataset used for the mass spectrometry interactome characterization experiments showing protein identification and quantification are included in File A.1.

For pathway enrichment analysis of identified proteins, EnrichR was used and GO Cellular Component 2018 terms were used to differentiate secretory pathway associated proteins from background (Table A.2)<sup>41</sup>. Tg interactors were similarly analyzed using GO Molecular Function 2018 terms. Spectrum and result files are available via ProteomeXchange under identifier PXD019427.

#### *2.9.6 Immunoblotting, SDS-PAGE, and Immunoprecipitation*

Cell lysates were prepared by lysing in RIPA buffer with protease inhibitor cocktail and protein concentrations were normalized. Lysates were then denatured with 1X Laemmli buffer + 100mM DTT and heated at 95°C for 5 minutes before being separated by SDS-PAGE. Samples were transferred onto polyvinylidene difluoride (PVDF) membranes (Millipore) for immunoblotting and blocked in TBS-T. Primary antibodies were incubated either at room temperature for 2 hours, or overnight at 4°C. Membranes were then washed four times with TBS-T and incubated with secondary antibody in 5% non-fat dry milk/TBS-T either at room temperature for 1 hour or overnight at 4°C. Membranes were washed four times with TBS-T and then imaged using a ChemiDoc MP Imaging System (BioRad). Quantification was performed using Image Lab Software (BioRad). For Tg immunoprecipitation, normalized lysates were incubated with M2 anti-flag agarose resin



or G1 Anti-DYKDDDDK affinity resin overnight at 4°C. Resin was then washed four times with RIPA buffer and samples were eluted using 3X Laemmli buffer with 100mM DTT. For immunoblot confirmation of Tg interactors, samples were processed exactly as described above for interactome characterization and proteins were eluted once with elution buffer (2% SDS, 1mM EDTA, in PBS) by heating at 95°C for 5 minutes.

### *2.9.7 Cycloheximide Chase Assay*

Cells transfected with Tg variants were plated onto poly-D-lysine coated wells in 6-well dishes. Cells were washed twice with 2mL of media treated with cycloheximide (50 µg/mL), then chased with 1mL of cycloheximide-treated media and collected at various time points. Cells were harvested by aspirating media, washing cells twice with 2mL of cold PBS and lysing in 1mL RIPA buffer with protease inhibitor cocktail (Roche, 4693159001). Collected media was spun down at 400x g for 5 minutes to pellet any floating cells. Cell lysate and media was subjected to immunoprecipitation with M2 anti-flag agarose resin or G1 Anti-DYKDDDDK affinity resin overnight at 4°C. Resin was then washed four times with RIPA buffer and samples were eluted using 3X Laemmli buffer with 100mM DTT. Eluted samples were separated by SDS-PAGE and transferred to PVDF membrane and probed with primary and secondary antibody as described above.

### *2.9.8 <sup>35</sup>S Pulse Chase Assay*

Cells transfected with Tg variants were plated onto poly-D-lysine coated wells in 6-well dishes. Cells were incubated with methionine and cysteine depleted DMEM supplemented with glutamine, penicillin/streptomycin, and 10% FBS at 37°C for 30 minutes. Cells were then metabolically labeled in DMEM depleted of methionine and cysteine, and supplemented with EasyTag <sup>35</sup>S Protein Labeling Mix (Perkin Elmer, NEG772007MC), glutamine, penicillin/streptomycin, and 10% FBS at 37°C for 30 minutes. Afterward, cells were washed twice with DMEM containing 10 X methionine and cysteine, followed by a burn off period of 30 minutes in normal DMEM. Cells were then chased for the respective time period with normal DMEM, lysed with 500uL of RIPA buffer with protease inhibitor cocktail and 10mM dithiothreitol (DTT). Cell lysates were diluted with 500uL of RIPA buffer with protease inhibitor cocktail and subjected to immunoprecipitation with G1 anti-DYKDDDDK affinity resin overnight at 4°C. After three washes with RIPA buffer protein samples were eluted with 3X Laemmli buffer with 100mM DTT heating at 95°C for 5 minutes. Eluted samples were then separated by SDS-PAGE, gels were dried and exposed on a storage phosphor screen. Radioactive band intensity was then measured using a Typhoon Trio Imager (GE Healthcare) and quantified by densitometry in Image Lab (BioRad).

#### *2.9.9 EndoH and PNGaseF Treatment*

Cells were lysed in either RIPA or TNI (50mM Tris pH 7.5, 250mM NaCl, 1mM EDTA, and 0.5% IGEPAL CA-630) buffer with protease inhibitor cocktail, denatured, and

digested with EndoH or PNGase F per the manufacturer specifications (New England BioLabs).

## 2.10 References

1. Carvalho, D. P. & Dupuy, C. Thyroid hormone biosynthesis and release. *Molecular and Cellular Endocrinology* **458**, 6–15 (2017).
2. Dai, G., Levy, O. & Carrasco, N. Cloning and characterization of the thyroid iodide transporter. *Nature* **379**, 458–460 (1996).
3. Fayadat, L., Niccoli-Sire, P., Lanet, J. & Franc, J.-L. Role of Heme in Intracellular Trafficking of Thyroperoxidase and Involvement of H<sub>2</sub>O<sub>2</sub> Generated at the Apical Surface of Thyroid Cells in Autocatalytic Covalent Heme Binding. *Journal of Biological Chemistry* **274**, 10533–10538 (1999).
4. Di Jeso, B. & Arvan, P. Thyroglobulin From Molecular and Cellular Biology to Clinical Endocrinology. *Endocrine Reviews* **37**, 2–36 (2016).
5. Citterio, C. E., Targovnik, H. M. & Arvan, P. The role of thyroglobulin in thyroid hormonogenesis. *Nature Reviews Endocrinology* **15**, 323–338 (2019).
6. Oetting, A. & Yen, P. M. New insights into thyroid hormone action. *Best Practice & Research Clinical Endocrinology & Metabolism* **21**, 193–208 (2007).
7. Chaker, L., Bianco, A. C., Jonklaas, J. & Peeters, R. P. Hypothyroidism. *The Lancet* **390**, 1550–1562 (2017).
8. Rose, S. R. *et al.* Update of Newborn Screening and Therapy for Congenital Hypothyroidism. *PEDIATRICS* **117**, 2290–2303 (2006).
9. Kim, P. S., Kwon, O. Y. & Arvan, P. An endoplasmic reticulum storage disease causing congenital goiter with hypothyroidism. *The Journal of Cell Biology* **133**, 517–527 (1996).
10. Hartl, F. U., Bracher, A. & Hayer-Hartl, M. Molecular chaperones in protein folding and proteostasis. *Nature* **475**, 324–332 (2011).
11. Balchin, D., Hayer-Hartl, M. & Hartl, F. U. In vivo aspects of protein folding and quality control. *Science* **353**, aac4354 (2016).
12. Sun, Z. & Brodsky, J. L. Protein quality control in the secretory pathway. *Journal of Cell Biology* vol. 218 3171–3187 (2019).
13. Menon, S. *et al.* Oxidoreductase Interactions Include a Role for ERp72 Engagement with Mutant Thyroglobulin from the rdw/rdw Rat Dwarf. *Journal of Biological Chemistry* **282**, 6183–6191 (2007).
14. Baryshev, M. *et al.* Unfolded protein response is involved in the pathology of human congenital hypothyroid goiter and rat non-goitrous congenital hypothyroidism. *J Mol Endocrinol* **32**, 903–20 (2004).

15. Park, Y. & Arvan, P. The Acetylcholinesterase Homology Region Is Essential for Normal Conformational Maturation and Secretion of Thyroglobulin. *Journal of Biological Chemistry* **279**, 17085–17089 (2004).
16. Hishinuma, A. Two Novel Cysteine Substitutions (C1263R and C1995S) of Thyroglobulin Cause a Defect in Intracellular Transport of Thyroglobulin in Patients with Congenital Goiter and the Variant Type of Adenomatous Goiter. *Journal of Clinical Endocrinology & Metabolism* **84**, 1438–1444 (1999).
17. Muresan, Z. & Arvan, P. Thyroglobulin Transport along the Secretory Pathway. *Journal of Biological Chemistry* **272**, 26095–26102 (1997).
18. Di Jeso, B. *et al.* Mixed-Disulfide Folding Intermediates between Thyroglobulin and Endoplasmic Reticulum Resident Oxidoreductases ERp57 and Protein Disulfide Isomerase. *Molecular and Cellular Biology* **25**, 9793–9805 (2005).
19. Kim, P. S. & Arvan, P. Hormonal regulation of thyroglobulin export from the endoplasmic reticulum of cultured thyrocytes. *J Biol Chem* **268**, 4873–9 (1993).
20. Olivieri, A., Fazzini, C. & Medda, E. Multiple Factors Influencing the Incidence of Congenital Hypothyroidism Detected by Neonatal Screening. *Hormone Research in Paediatrics* **83**, 86–93 (2015).
21. Plate, L. & Wiseman, R. L. Regulating Secretory Proteostasis through the Unfolded Protein Response: From Function to Therapy. *Trends in Cell Biology* **27**, 722–737 (2017).
22. Hetz, C., Axten, J. M. & Patterson, J. B. Pharmacological targeting of the unfolded protein response for disease intervention. *Nature Chemical Biology* **15**, 764–775 (2019).
23. Cooley, C. B. *et al.* Unfolded protein response activation reduces secretion and extracellular aggregation of amyloidogenic immunoglobulin light chain. *Proceedings of the National Academy of Sciences* **111**, 13046–13051 (2014).
24. Chen, J. J. *et al.* ATF6 Activation Reduces the Secretion and Extracellular Aggregation of Destabilized Variants of an Amyloidogenic Protein. *Chemistry & Biology* **21**, 1564–1574 (2014).
25. Sardiù, M. E. & Washburn, M. P. Construction of Protein Interaction Networks Based on the Label-Free Quantitative Proteomics. *Methods in Molecular Biology* 71–85 (2011).
26. Pankow, S. *et al.*  $\Delta$ F508 CFTR interactome remodelling promotes rescue of cystic fibrosis. *Nature* **528**, 510–516 (2015).
27. Doan, N.-D., DiChiara, A. S., Del Rosario, A. M., Schiavoni, R. P. & Shoulders, M. D. Mass Spectrometry-Based Proteomics to Define Intracellular Collagen Interactomes. *Methods Mol Biol* **1944**, 95–114 (2019).
28. Taipale, M. *et al.* A Quantitative Chaperone Interaction Network Reveals the Architecture of Cellular Protein Homeostasis Pathways. *Cell* **158**, 434–448 (2014).
29. Behnke, J., Mann, M. J., Scruggs, F.-L., Feige, M. J. & Hendershot, L. M. Members of the Hsp70 Family Recognize Distinct Types of Sequences to Execute ER Quality Control. *Molecular Cell* **63**, 739–752 (2016).
30. Christianson, J. C. *et al.* Defining human ERAD networks through an integrative mapping strategy. *Nature Cell Biology* **14**, 93–105 (2012).

31. Coscia, F. *et al.* The structure of human thyroglobulin. *Nature* **578**, 627–630 (2020).
32. Kim, P. S. *et al.* A single amino acid change in the acetylcholinesterase-like domain of thyroglobulin causes congenital goiter with hypothyroidism in the cog/cog mouse: A model of human endoplasmic reticulum storage diseases. *Proceedings of the National Academy of Sciences* **95**, 9909–9913 (1998).
33. Caputo, M. *et al.* Congenital hypothyroidism with goitre caused by new mutations in the thyroglobulin gene. *Clinical Endocrinology* **67**, 351–357 (2007).
34. Lee, J., Di Jeso, B. & Arvan, P. The cholinesterase-like domain of thyroglobulin functions as an intramolecular chaperone. *Journal of Clinical Investigation* **118**, 2950–2958 (2008).
35. Lee, J., Wang, X., Di Jeso, B. & Arvan, P. The Cholinesterase-like Domain, Essential in Thyroglobulin Trafficking for Thyroid Hormone Synthesis, Is Required for Protein Dimerization. *Journal of Biological Chemistry* **284**, 12752–12761 (2009).
36. Pardo, V. *et al.* The p.A2215D Thyroglobulin Gene Mutation Leads to Deficient Synthesis and Secretion of the Mutated Protein and Congenital Hypothyroidism with Wide Phenotype Variation. *The Journal of Clinical Endocrinology & Metabolism* **94**, 2938–2944 (2009).
37. Lee, J., Di Jeso, B. & Arvan, P. Maturation of Thyroglobulin Protein Region I. *Journal of Biological Chemistry* **286**, 33045–33052 (2011).
38. Plate, L. *et al.* Quantitative Interactome Proteomics Reveals a Molecular Basis for ATF6-Dependent Regulation of a Destabilized Amyloidogenic Protein. *Cell Chemical Biology* **26**, 913-925.e4 (2019).
39. Budayeva, H. G. & Cristea, I. M. A Mass Spectrometry View of Stable and Transient Protein Interactions. *Advances in Experimental Medicine and Biology* 263–282 (2014).
40. Keilhauer, E. C., Hein, M. Y. & Mann, M. Accurate Protein Complex Retrieval by Affinity Enrichment Mass Spectrometry (AE-MS) Rather than Affinity Purification Mass Spectrometry (AP-MS). *Molecular & Cellular Proteomics* **14**, 120–135 (2015).
41. Chen, E. Y. *et al.* Enrichr: interactive and collaborative HTML5 gene list enrichment analysis tool. *BMC Bioinformatics* **14**, 128 (2013).
42. Kim, P. S. & Arvan, P. Calnexin and BiP act as sequential molecular chaperones during thyroglobulin folding in the endoplasmic reticulum. *The Journal of Cell Biology* **128**, 29–38 (1995).
43. Pobre, K. F. R., Poet, G. J. & Hendershot, L. M. The endoplasmic reticulum (ER) chaperone BiP is a master regulator of ER functions: Getting by with a little help from ERdj friends. *Journal of Biological Chemistry* vol. 294 2098–2108 (2019).
44. Di Jeso, B. *et al.* Transient Covalent Interactions of Newly Synthesized Thyroglobulin with Oxidoreductases of the Endoplasmic Reticulum. *Journal of Biological Chemistry* **289**, 11488–11496 (2014).
45. Christianson, J. C., Shaler, T. A., Tyler, R. E. & Kopito, R. R. OS-9 and GRP94 deliver mutant  $\alpha$ 1-antitrypsin to the Hrd1–SEL1L ubiquitin ligase complex for ERAD. *Nature Cell Biology* **10**, 272–282 (2008).

46. Tang, H.-Y., Huang, C.-H., Zhuang, Y.-H., Christianson, J. C. & Chen, X. EDEM2 and OS-9 Are Required for ER-Associated Degradation of Non-Glycosylated Sonic Hedgehog. *PLoS ONE* **9**, e92164 (2014).
47. Hirao, K. *et al.* EDEM3, a soluble EDEM homolog, enhances glycoprotein endoplasmic reticulum-associated degradation and mannose trimming. *Journal of Biological Chemistry* **281**, 9650–9658 (2006).
48. Bernasconi, R., Pertel, T., Luban, J. & Molinari, M. A dual task for the Xbp1-responsive OS-9 variants in the mammalian endoplasmic reticulum: Inhibiting secretion of misfolded protein conformers and enhancing their disposal. *Journal of Biological Chemistry* **283**, 16446–16454 (2008).
49. Kim, P. S., Bole, D. & Arvan, P. Transient aggregation of nascent thyroglobulin in the endoplasmic reticulum: relationship to the molecular chaperone, BiP. *The Journal of Cell Biology* **118**, 541–549 (1992).
50. Kim, P. S., Kim, K. R. & Arvan, P. Disulfide-linked aggregation of thyroglobulin normally occurs during nascent protein folding. *American Journal of Physiology-Cell Physiology* **265**, C704–C711 (1993).
51. Tokunaga, F., Brostrom, C., Koide, T. & Arvan, P. Endoplasmic Reticulum (ER)-associated Degradation of Misfolded N -Linked Glycoproteins Is Suppressed upon Inhibition of ER Mannosidase I. *Journal of Biological Chemistry* **275**, 40757–40764 (2000).
52. Kozlov, G. *et al.* Crystal Structure of the bb' Domains of the Protein Disulfide Isomerase ERp57. *Structure* **14**, 1331–1339 (2006).
53. Lamriben, L., Graham, J. B., Adams, B. M. & Hebert, D. N. N -Glycan-based ER Molecular Chaperone and Protein Quality Control System: The Calnexin Binding Cycle. *Traffic* **17**, 308–326 (2016).
54. Martiniuk, F., Ellenbogen, A. & Hirschhorn, R. Identity of neutral alpha-glucosidase AB and the glycoprotein processing enzyme glucosidase II. Biochemical and genetic studies. *J Biol Chem* **260**, 1238–42 (1985).
55. Braunger, K. *et al.* Structural basis for coupling protein transport and N-glycosylation at the mammalian endoplasmic reticulum. *Science (1979)* **360**, 215–219 (2018).
56. Ruiz-Canada, C., Kelleher, D. J. & Gilmore, R. Cotranslational and Posttranslational N-Glycosylation of Polypeptides by Distinct Mammalian OST Isoforms. *Cell* **136**, 272–283 (2009).
57. Cherepanova, N. A. & Gilmore, R. Mammalian cells lacking either the cotranslational or posttranslational oligosaccharyltransferase complex display substrate-dependent defects in asparagine linked glycosylation. *Scientific Reports* **6**, 1–12 (2016).
58. Kelleher, D. J., Karaoglu, D., Mandon, E. C. & Gilmore, R. Oligosaccharyltransferase Isoforms that Contain Different Catalytic STT3 Subunits Have Distinct Enzymatic Properties. *Molecular Cell* **12**, 101–111 (2003).
59. Kanou, Y. *et al.* Thyroglobulin Gene Mutations Producing Defective Intracellular Transport of Thyroglobulin Are Associated with Increased Thyroidal Type 2

- Iodothyronine Deiodinase Activity. *The Journal of Clinical Endocrinology & Metabolism* **92**, 1451–1457 (2007).
60. Muresan, Z. & Arvan, P. Enhanced Binding to the Molecular Chaperone BiP Slows Thyroglobulin Export from the Endoplasmic Reticulum. *Molecular Endocrinology* **12**, 458–467 (1998).
  61. Oikonomou, C. & Hendershot, L. M. Disposing of misfolded ER proteins: A troubled substrate's way out of the ER. *Molecular and Cellular Endocrinology* **500**, 110630 (2020).
  62. Awad, W., Estrada, I., Shen, Y. & Hendershot, L. M. BiP mutants that are unable to interact with endoplasmic reticulum DnaJ proteins provide insights into interdomain interactions in BiP. *Proceedings of the National Academy of Sciences* **105**, 1164–1169 (2008).
  63. Avezov, E., Frenkel, Z., Ehrlich, M., Herscovics, A. & Lederkremer, G. Z. Endoplasmic Reticulum (ER) Mannosidase I Is Compartmentalized and Required for N -Glycan Trimming to Man 5–6 GlcNAc 2 in Glycoprotein ER-associated Degradation. *Molecular Biology of the Cell* **19**, 216–225 (2008).
  64. Molinari, M., Calanca, V., Galli, C., Lucca, P. & Paganetti, P. Role of EDEM in the Release of Misfolded Glycoproteins from the Calnexin Cycle. *Science (1979)* **299**, 1397–1400 (2003).
  65. Oda, Y., Hosokawa, N., Wada, I. & Nagata, K. EDEM As an Acceptor of Terminally Misfolded Glycoproteins Released from Calnexin. *Science (1979)* **299**, 1394–1397 (2003).
  66. Nakatsukasa, K., Brodsky, J. L. & Kamura, T. A stalled retrotranslocation complex reveals physical linkage between substrate recognition and proteasomal degradation during ER-associated degradation. *Molecular Biology of the Cell* **24**, 1765–1775 (2013).
  67. Schuck, S., Gallagher, C. M. & Walter, P. ER-phagy mediates selective degradation of endoplasmic reticulum independently of the core autophagy machinery. *Journal of Cell Science* **127**, 4078–4088 (2014).
  68. Pohl, C. & Dikic, I. Cellular quality control by the ubiquitin-proteasome system and autophagy. *Science (1979)* **366**, 818–822 (2019).
  69. Carvalho, P., Goder, V. & Rapoport, T. A. Distinct Ubiquitin-Ligase Complexes Define Convergent Pathways for the Degradation of ER Proteins. *Cell* **126**, 361–373 (2006).
  70. Hammond, C., Braakman, I. & Helenius, A. Role of N-linked oligosaccharide recognition, glucose trimming, and calnexin in glycoprotein folding and quality control. *Proceedings of the National Academy of Sciences* **91**, 913–917 (1994).
  71. Pardo, V. *et al.* Phenotypic Variation Among Four Family Members with Congenital Hypothyroidism Caused by Two Distinct Thyroglobulin Gene Mutations. *Thyroid* **18**, 783–786 (2008).
  72. Allen, S., Naim, H. Y. & Bulleid, N. J. Intracellular Folding of Tissue-type Plasminogen Activator. *Journal of Biological Chemistry* **270**, 4797–4804 (1995).

73. Ryno, L. M. *et al.* Characterizing the Altered Cellular Proteome Induced by the Stress-Independent Activation of Heat Shock Factor 1. *ACS Chemical Biology* **9**, 1273–1283 (2014).
74. Plate, L. *et al.* Small molecule proteostasis regulators that reprogram the ER to reduce extracellular protein aggregation. *Elife* **5**, (2016).
75. Gallagher, C. M. & Walter, P. Ceapins inhibit ATF6 $\alpha$  signaling by selectively preventing transport of ATF6 $\alpha$  to the Golgi apparatus during ER stress. *Elife* **5**, (2016).
76. Cross, B. C. S. *et al.* The molecular basis for selective inhibition of unconventional mRNA splicing by an IRE1-binding small molecule. *Proceedings of the National Academy of Sciences* **109**, E869–E878 (2012).
77. Shoulders, M. D. *et al.* Stress-Independent Activation of XBP1s and/or ATF6 Reveals Three Functionally Diverse ER Proteostasis Environments. *Cell Reports* **3**, 1279–1292 (2013).
78. Fonslow, B. R. *et al.* Single-Step Inline Hydroxyapatite Enrichment Facilitates Identification and Quantitation of Phosphopeptides from Mass-Limited Proteomes with MudPIT. *Journal of Proteome Research* **11**, 2697–2709 (2012).
79. Storey, J. D. & Tibshirani, R. Statistical significance for genomewide studies. *Proc Natl Acad Sci U S A* (2003).



## **Time-Resolved Interactome Profiling Deconvolutes Protein Quality Control Dynamics\***

### **3.1 Introduction**

Protein-protein interactions drive functional diversity within cells. As genetic information flows from genome, transcriptome, to proteome and beyond into the realm of the interactome or protein-protein interactions, these stages become closer and closer to the observed phenotypes for cellular processes and pathological states<sup>1</sup>. A prominent area where this is the case is within protein homeostasis (proteostasis). As detailed in Chapter 1, the proteostasis network (PN), consisting of protein folding chaperones, trafficking, and degradation components maintains the integrity of the proteome by ensuring the appropriate trafficking and localization of properly folded proteins while recognizing misfolded, potentially detrimental proteins and routing them for degradation<sup>2-5</sup>. This concerted action by cells is referred to as protein quality control (PQC). Perturbations to these processes through genetic, age-related, or environmental factors manifest in

---

\* This chapter contains material adapted from the submitted research article: “Time-Resolved Interactome Profiling Deconvolutes Secretory Protein Quality Control Dynamics” by Madison T. Wright, Bibek Timalsina, Valeria Garcia Lopez, & Lars Plate. It has been reproduced with the permission of the publisher and co-authors.

several disease states including amyloidosis, neurodegeneration, and cancer amongst others<sup>6-10</sup>.

To comprehend the pathogenesis of these diseases, scientist have dedicated many efforts to identifying and quantifying the protein-protein interactions and subsequent changes in interactions within these biological processes and disease states. Classical experiments used yeast two-hybrid systems and eventually co-immunoprecipitation coupled with western blot analysis<sup>11-13</sup>. More modern approaches have included the Luminescence-based Mammalian IntERactome (LUMIER) assay as well as affinity purification – mass spectrometry (AP-MS)<sup>14-16</sup>.

These methods have led to fruitful discoveries, yet most lack the ability to measure changes over time. While proximity labeling mass spectrometry (BioID and APEX-MS) has been used to spatiotemporally resolve protein-protein interactions, this has only been done to identify interactions after protein maturation<sup>17,18</sup>. Unnatural amino acid incorporation with methods such as biorthogonal non-canonical amino acid tagging (BONCAT), pulsed azidohomoalanine (PALM), or heavy isotope labeled azidohomoalanine (HILAQ) have shown promising results to identify newly synthesized proteins but have not been implemented to focus on a single endogenously expressed protein or group of proteins that is often required for investigating disease context<sup>19-25</sup>.

Similar labeling approaches at the DNA and RNA level are used to temporally resolve nascent DNA-protein and RNA-protein interactions in cell culture and whole organisms. Isolation of proteins on nascent DNA (iPOND) has revealed the timing of DNA-protein interactions during replication and chromatin assembly<sup>26-28</sup>. Similar methods including, thiouracil crosslinking mass spectrometry (TUX-MS) and viral cross-linking and solid-phase purification (VIR-CLASP) are used to study the timing of RNA-protein interactions during viral infection<sup>29,30</sup>. Yet, no methods are available to identify de novo protein-protein interactions of newly synthesized proteins in a client specific manner with temporal resolution.

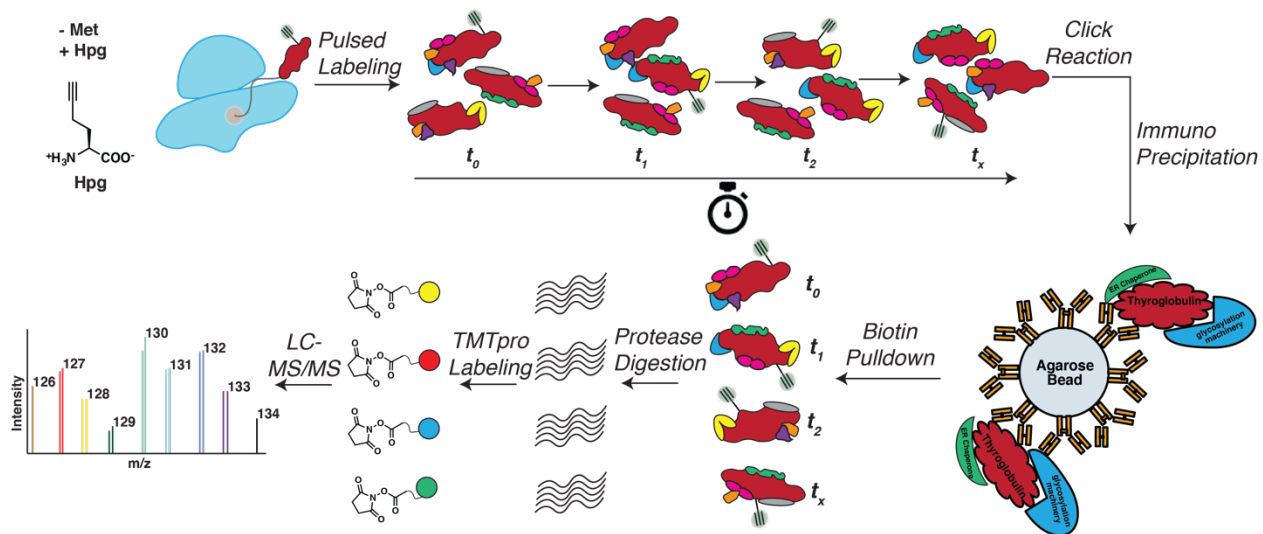
In Chapter 2 we mapped the interactome of the secreted thyroid prohormone thyroglobulin (Tg), comparing the WT protein to secretion defective mutations implicated in congenital hypothyroidism (CH)<sup>8</sup>. Tg is a large, heavily modified, 330 kDa prohormone that is necessary to produce T3 and T4 thyroid specific hormones and relies heavily on distinct interactions with the PN to facilitate folding and eventual secretion<sup>31,32</sup>. Chapter 2 identified topological changes in Tg-PN engagement among CH-associated Tg mutants compared to WT. Although, with the lack of temporal resolution in such investigations it is difficult to discern which changes in interactions are simply correlated with disease pathogenesis and which are responsible for the development of pathogenesis. To address this shortcoming, we developed time-resolved interactome profiling (TRIP) to capture and quantify interactions between Tg and interacting partners throughout the life cycle of the protein. Chapter 3 will detail the development of this method and show how

Tg mutants are characterized by both broad temporal alterations across Hsp70/90 and disulfide/redox processing pathways, and discrete changes with select PN components. Moreover, we find that these changes are correlated with alterations in interactions with degradation components downstream.

### **3.2 TRIP temporally resolves Tg interactions with PQC components**

To develop this method, we envisioned a two-stage enrichment strategy utilizing pulsed biorthogonal unnatural amino acid labeling and functionalization. After pulse labeling with homopropargylglycine (Hpg), samples could be collected across time points throughout the “chase” period<sup>33,34</sup>. After conjugating the Hpg alkyne using copper catalyzed click-chemistry (CuAAC) the protein of interest could be globally captured and enriched using immunoprecipitation. The second enrichment step would then utilize a biotin-streptavidin pulldown to capture the pulse Hpg labeled and Cu-AAC conjugated population, enriching samples into time-resolved fractions for quantitative liquid chromatography – tandem mass spectrometry (LC-MS/MS) analysis with TMTpro multiplexing (Figure 3.1)<sup>35,36</sup>.

We first set out to determine if Tg could tolerate immunoprecipitation after pulse Hpg labeling, dithiobis(succinimidyl propionate) (DSP) crosslinking, and CuAAC conjugation with a trifunctional tetramethylrhodamine (TAMRA)-Azide-Polyethylene Glycol (PEG)-Desthiobiotin probe (Figure 3.2A). In chapter 2 we showed that a c-terminal FLAG-tag is tolerated by Tg and allows efficient capture via immunoprecipitation, while DSP

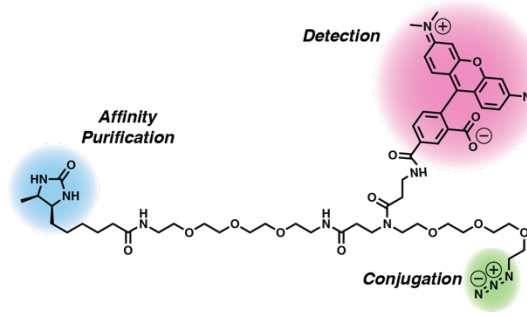
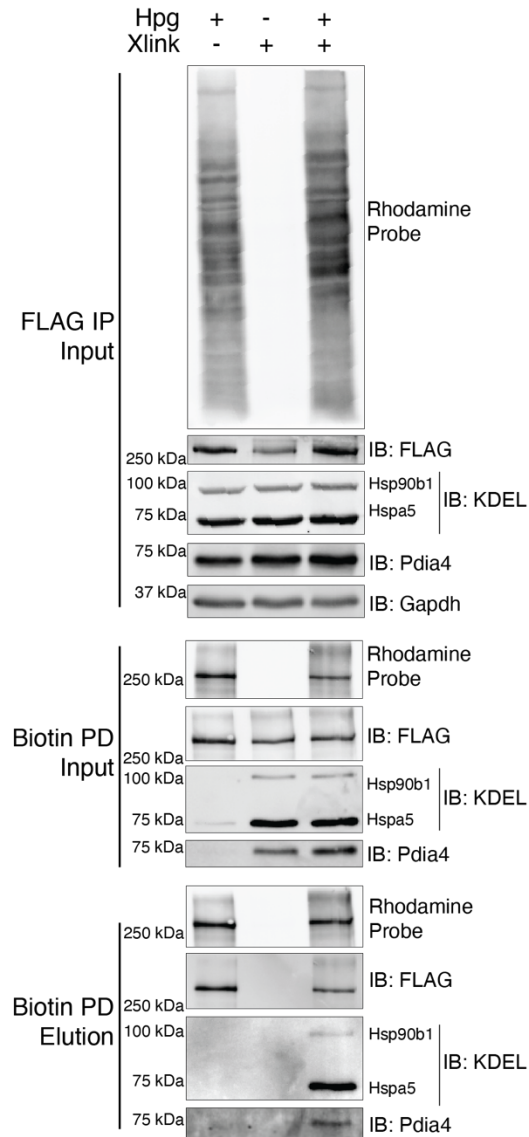
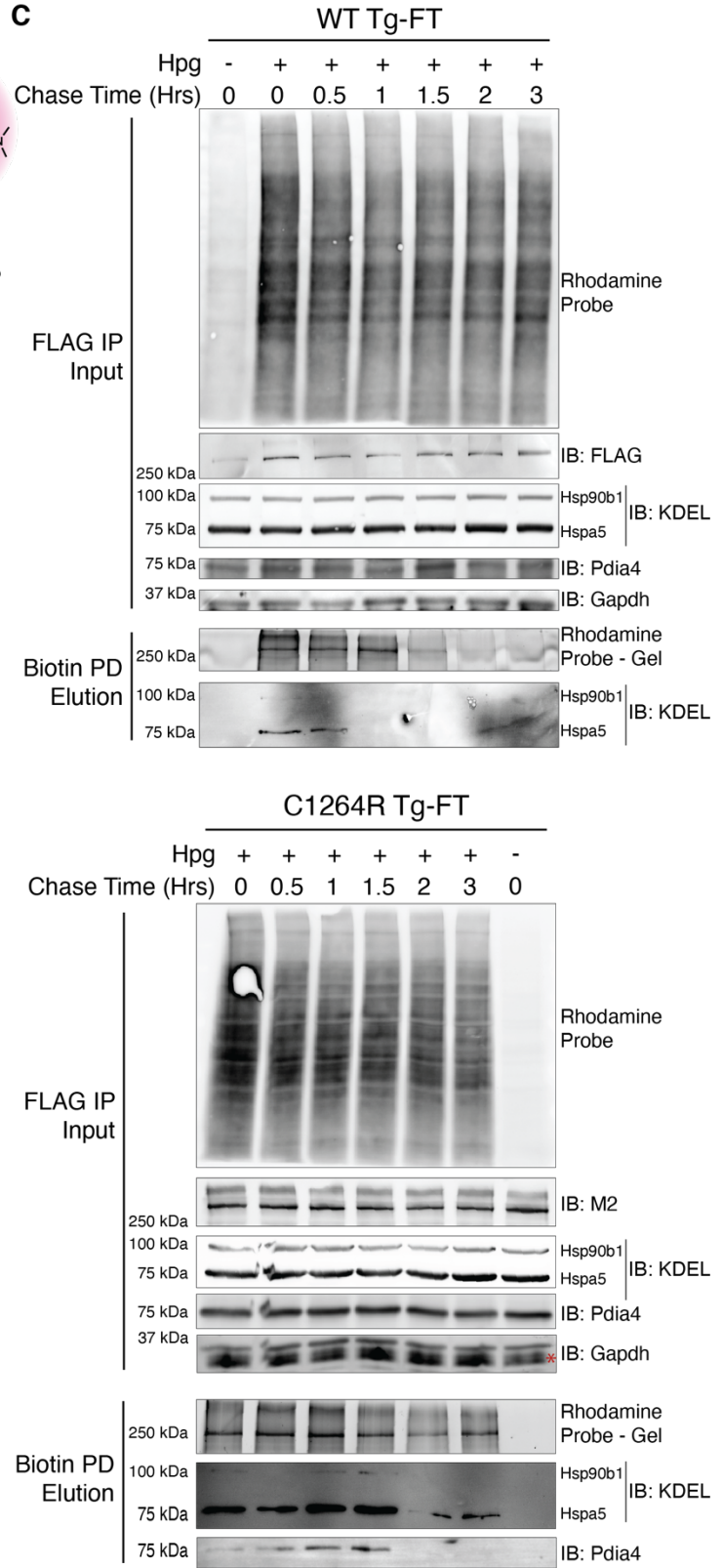


**Figure 3.1: Time-Resolved Interactome Profiling to Identify Interactions with Newly Synthesized Proteins**

Workflow for TRIP protocol including pulsed unnatural amino acid labeling with Hpg, labeled protein functionalization with CuAAC click chemistry, global immunoprecipitation, followed by streptavidin-biotin enrichment into time-resolved fractions, and finally TMTpro multiplexed quantitative proteomics.

crosslinker aids in capturing transient protein-protein interactions that take place during Tg processing<sup>8</sup>. To this end, we pulse labeled Fischer rat thyroid (FRT) cells stabling expressing Tg for 4 hours with Hpg, performed DSP crosslinking, CuAAC, and tested our two-stage enrichment strategy via western blot analysis (Figure 3.2B; Figure B.1A and B.1B).

Labeling with Hpg, crosslinking, and subsequent CuAAC did not significantly affect immunoprecipitation efficiency and allowed for robust purification of Tg and well validated interacting proteins. We benchmarked our TRIP approach by monitoring Tg interactors Hspa5, Hsp90b1, and Pdia4<sup>8,37,38</sup>. Moreover, DSP crosslinking was necessary to capture these interactions after the dual purification and stringent wash

**A****B****C**

### **Figure 3.2: TRIP Temporally Resolves Tg Interactions with Protein Quality Control Components**

(A) Chemical structure of tri-functional probe used for CuAAC conjugation, fluorescence visualization, and enrichment of Hpg pulse-labeled protein.

(B) Western blot analysis of each step of the two-stage purification strategy with continuous Hpg labeling showing (-) crosslinking and (-) Hpg controls. Both Hpg labeling and crosslinking are necessary for efficient capture of interactors with TRIP.

(C) Western blot analysis of Hpg-pulsed and chased WT and C1264R Tg-FT TRIP. Well known Tg interactors show higher enrichment over time with the misfolded C1264R Tg mutant compared to WT.

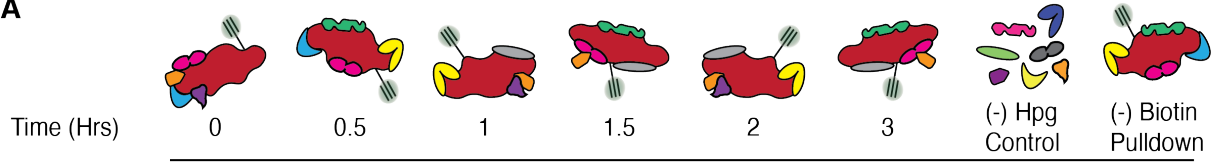
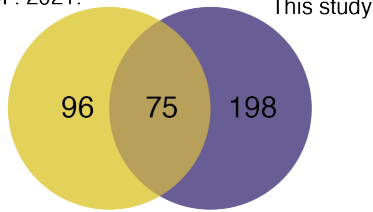
steps (Figure 3.2B). We next wanted to investigate whether TRIP could temporally resolve interactions with these PN components. We pulse labeled cells with Hpg for 1 Hr, followed by a 3 Hr chase and analysis via western blot (Figure 3.2C). For WT Tg we found that engagement with Hspa5 peaked within the first 30 minutes of the chase period and rapidly declined, in line with previous observations, but engagement with Pdia4 was not detectable by western blot analysis<sup>37,39</sup>. To test the ability of TRIP to identify temporal differences in PQC dynamics across Tg constructs we performed TRIP on FRT cells stably expressing C1264R Tg, a known patient-specific mutation implicated in CH<sup>40,41</sup>. Engagement with Hspa5 was highly abundant at the 0 Hr time point and peaked later in the chase period at 2 hours, and then rapidly declined. A similar temporal profile was also observed for Hsp90b1. Additionally, Pdia4 engagement was detectable for C1264R Tg and found to gradually increase throughout the first 1.5 hours of the chase period, before rapidly declining (Figure 3.2C). These data highlight the utility of TRIP to not only identify changes in protein interactions over time but monitor how these interactions may change for a given protein of interest across different disease states. Moreover, these data corroborate our findings from Chapter 2<sup>8</sup>.

### **3.3 TRIP identifies altered temporal dynamics associated with Tg processing**

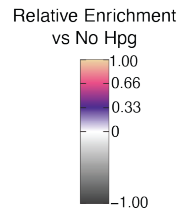
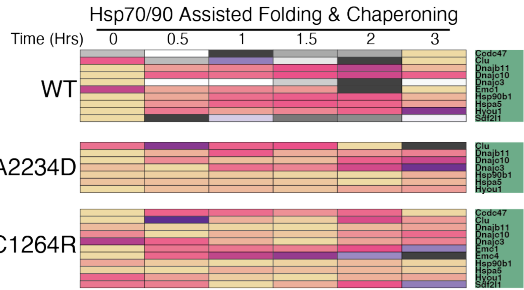
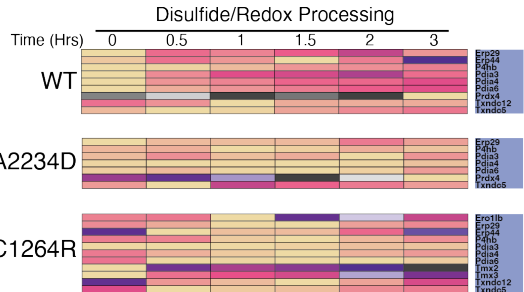
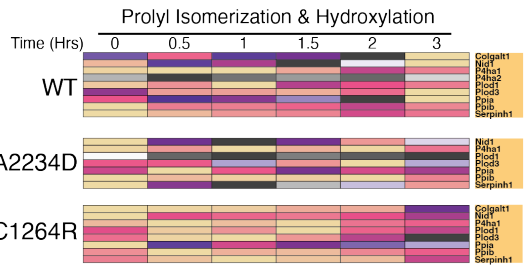
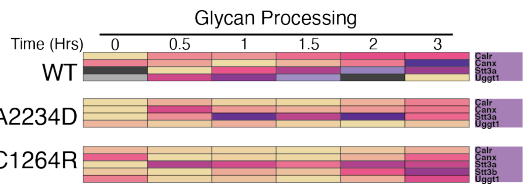
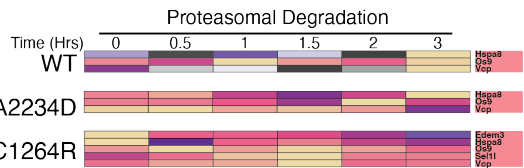
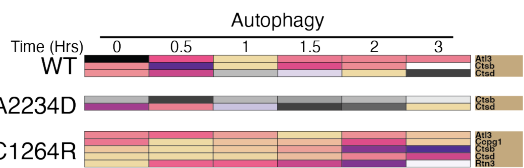
Next, we wanted to benchmark the utility of our TRIP approach to temporally resolve previously identified and novel interactors, as the Tg interactome has not been fully characterized in native tissue. To this end we utilized our TRIP approach in FRT cells stably expressing WT, A2234D, and C1264R Tg. We focused on A2234D and C1264R Tg as they present with distinct defects in Tg processing and structural insults<sup>40,41</sup>.

We utilized a (-) biotin pulldown booster (or carrier) channel with cells that were pulse-labeled with Hpg, underwent CuAAC functionalization, and immunoprecipitation, but did not undergo biotin-streptavidin enrichment. This booster sample acts to 1) aid in increased peptide/protein identification - compared to the much lower abundant chase samples 2) benchmark Tg interactors in FRT cells compared to our previously published dataset<sup>42,43</sup> (Figure 3.3A). When comparing the booster channel to our (-) Hpg samples we were satisfied to see that previously identified Tg interactors were heavily enriched, with most of them being significantly enriched (Figure B.2). The dataset in this study showed appreciable overlap between our previous results identifying 75 of the 171 Tg interactors and identifying 198 new interactors (Figure 3.3B). We noticed several ribosomal and proteasomal subunits, trafficking factors, and lysosomal components that were not identified in our Chapter 2 dataset (Figure B.2). We then took our list of previously identified interactors and PQC components found to

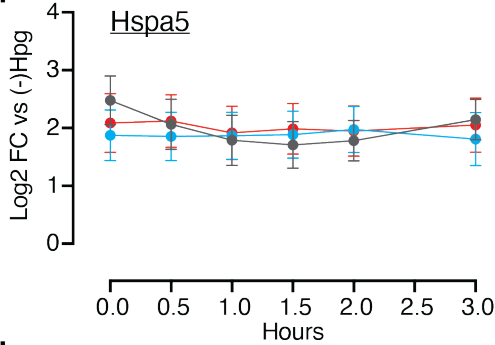
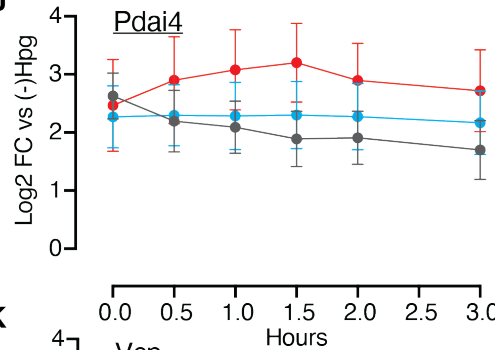
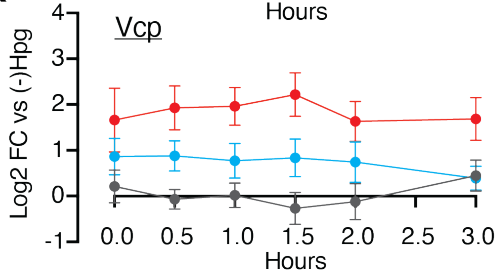


**A****B**Wright et al.  
MCP. 2021.

x2 → 16plex TMTpro

**C****D****E****F****G****H**

● WT ● A2234D ● C1264R

**I****J****K**

### **Figure 3.3: TRIP Identifies Altered Temporal Dynamics Associated with Tg Processing**

(A) TMTpro labeling scheme for TRIP experiments including a (-) Hpg control channel to identify enriched interactors and a (-) Biotin pulldown channel to act as a booster (or carrier).

(B) Venn diagram showing the overlap in proteostasis components identified as Tg interactors in our previous data set compared to this study.

(C-H) Heatmaps showing the relative enrichment for select Tg interactors across proteostasis pathways with WT, A2234D, or C1264R Tg constructs.

(I-K) Plots showing the Log<sub>2</sub> FC enrichment of select Tg interactors compared across constructs.

be enriched in the (-) biotin pulldown samples compared to (-) Hpg and carried these proteins forward to time-resolved analysis utilizing the Hpg-chase samples (Table B.1; File B.1).

After mapping the time-resolved Tg interactome we began to investigate temporal changes in PN dynamics across distinct pathways known to influence Tg processing (Figure B.3; Figure B.4). We found that both A2234D and C1264R exhibited prolonged engagement with components across Hsp70/90 and disulfide processing pathways (Figure 3.3C and 3.3D; Figure B.4). Particularly, A2234D and C1264R showed increased engagement with key components Hspa5, Hsp90b1, Hyou1, Dnajc3, Dnajb11, Dnajc10, and Sdf2l1 throughout the chase period whereas WT engagement peaked at the 0 Hr time point and consistently tapered off for many of these components. More specifically, Dnajc3 and Sdf2l1 were found to only be enriched at the 0 Hr timepoint for WT Tg (Figure 3.3C and 3.3I; Figure B.3). We even noticed altered temporal dynamics for previously unidentified interactors including Emc1 and Emc4 of the ER membrane complex (EMC) as well as Ccdc47, all of which are involved membrane protein processing within the

ER<sup>44-46</sup>. While in the case of WT Tg, Engagement for both Ccdc47 and Emc1 peaked at the end of the chase period, for C1264R this was largely inversed peaking at the 0 Hr time point and slowly tapering off. Nevertheless, it remains unclear why EMC components might engage with luminal Tg during biosynthesis and folding.

Similar trends were observed in the case of disulfide processing components. Pdia3, Pdia4, Pdia6, and Erp29/Pdia9 have all been heavily implicated in Tg processing<sup>37,47-49</sup>. While WT engagement with these components showed similar trends as Hsp70/90 chaperone engagement, peaking at the 0 Hr time point and consistently tapering, mutant engagement remained higher for longer and peaked only at 1-1.5 Hr time points for both A2234D and C1264R (Figure 3.3D and 3.3J). Tg engages with several prolyl isomerization and hydroxylation enzymes. In Chapter 2, changes in mutant vs WT engagement with prolyl isomerization and hydroxylation enzymes were quite small and disparate across constructs. With the utilization of TRIP, we found that previously identified interactors such as Nid1, P4ha1, and Serpinh1 show distinct patterns of altered temporal engagement when comparing mutant Tg to WT Tg (Figure 3.3E).

One area we were particularly interested in investing was the crosstalk and correlation between engagement with glycan processing components and degradation pathways. The glycosylation state of ER clients link to ER-associated degradation (ERAD) has been heavily investigated, whereas newly identified client degradation mechanisms involving autophagy at the ER (ER-phagy) or ER to lysosome-associated degradation (ERLAD)

are beginning to reveal novel degradation pathways for ER clients<sup>50-54</sup>. In Chapter 2 we showed that A2234D and C1264R differ in their engagement with N glycosylation components, particularly the oligosaccharyltransferase (OST) complex, and found that efficient A2234D degradation required both Stt3a and Stt3b catalytic subunits of the OST. Using our TRIP methodology, we wanted to further investigate this differential engagement with glycosylation components that may lead to altered degradation dynamics.

Like our results from Chapter 2, we identified many glycan processing enzymes, lectin chaperones, and several subunits of the OST complex, including Stt3a and Stt3b (Figure 3.3F & Figure B.4). While Stt3a engagement across all constructs showed similar temporal profiles, differences in downstream engagement with lectin chaperones Calr, Canx, and the “gatekeeping” glycosyltransferase Ugg1 were all observed. Calr engagement with WT peaked at the 0 Hr time point and continuously tapered off, while engagement with Canx rose starting at the 0 Hr time point and peaked at 1 Hr before tapering off. Conversely, for A2234D Calr engagement peaked both at the 0 Hr and 1-1.5 Hr time points, while Canx engagement peaked at the 0 Hr time point and tapered off like WT. Conversely, C1264R engagement with both Calr and Canx remained steadily high from 0.5 to 1.5 Hr timepoints with a decrease in engagement not being observed until 2-3 Hr. The staunchest difference we observed for glycan processing components was with Ugg1. Ugg1 regulates glycoprotein engagement and folding through the Canx/Calr cycle by re-glycosylating incompletely folded ER clients, and thus causing clients to reengage

through this lectin chaperone cycle<sup>55</sup>. In the case of WT, we found that Ugg1 engagement is moderate from 0.5-1.5 Hrs and peaks at 3 Hrs. Conversely, Ugg1 engagement with A2234D and C1264R peaked earlier and was much more stable throughout the chase period. This differential engagement with Ugg1 may suggest changes in monitoring of the Tg folded state. Moreover, Canx has been directly linked to emerging mechanisms of ERLAD for glycosylated ER clients (Figure 3.3F)<sup>54,56</sup>.

When monitoring both proteasomal and autophagy degradation pathway components we noticed both differential engagement within and across pathways. For example, the ERAD associated lectin, Os9, and ATPase, Vcp both peaked at the 3 Hr chase time point for WT Tg. With Os9 showing two distinct rises in engagement peaking at both the 1 Hr and 3 Hr time points, while Vcp showed only marginal engagement at the 0 Hr timepoint with no engagement again until the 3 Hr chase time point (Figure 3.3G and 3.3L). Conversely, A2234D exhibited early engagement with Vcp that decreased throughout the chase, yet Os9 showed similar late-stage engagement, like that of WT, which steadily increased throughout the chase before peaking at the 2 Hr time point. For C1264R, we observed additional engagement with the ERAD associated mannosidase EDEM3, that peaked early for the 0 Hr timepoint and steadily decreased overtime, while Os9, Vcp, and engagement with Sel1l, the adaptor subunit for the Hrd1 ERAD E3 ubiquitin ligase all steadily increased before peaking at the 1.5 Hr time point and dropping down through the 2-3 Hr time points (Figure 3.3G)<sup>50,51</sup>.

Our Chapter 2 dataset identified several lysosomal components, yet it was unclear how Tg might be delivered to the lysosomal. Recent work has identified several ER specific receptors that enable selective ER-phagy, and highlighted ER-phagy mechanisms for the clearance of mutant prohormones and other destabilized clients<sup>57,58</sup>. With this in mind, we were intrigued to find that we identified several lysosomal and autophagy related components and observed differential engagement across Tg constructs (Figure 3.3H; Figure B.4). Both WT and C1264R Tg showed appreciable engagement with lysosomal components, while A2234D interactions with these components was sparser. Consistent engagement with several lysosomal cathepsin proteases and glycan trimming enzymes was observed, with the timing being altered from WT to C1264R. We found that engagement with these components peaked for WT at 1 Hr, while for C1264R engagement peaked earlier and remained more stable throughout the chase period (Figure 3.3H & Figure B.4). Yet, the most striking observation was the enrichment of three different ER-phagy receptors, At13, Ccp1, and Rtn3 between WT and C1264R<sup>59-62</sup>. At13 showed similar enrichment patterns between WT and C1264R with engagement rising and peaking at 1-1.5 Hr time points before beginning to taper off. On the other hand, Ccp1 and Rtn3 were found to specifically interact with C1264R, with Rtn3 engagement peaking early and tapering off, while Ccp1 engagement remained much more stable (Figure 3.3H). One striking observation we also made was that EMC interactions for C1264R correlated with Rtn3, Ctsb, and Ctsd engagement. This is particularly interesting as there are few known adaptor or accessory proteins that aid in client specific ER-phagy or ERLAD (Figure 3.3C and 3.3H).

Overall, these data exhibit the ability of our TRIP workflow to assess the temporal dynamics associated with PQC, providing further insight into the dysregulation of interactions within CH dyshormonogenesis. It is worth noting that many interactors, including Canx, Erp29, and Vcp amongst others, previously did not show any appreciable changes in Tg engagement from WT to mutant when using traditional AP-MS methods, yet TRIP was able to identify and highlight these unseen changes over time.

### **3.4 Discussion and Conclusions**

The timing of protein-protein interactions implicated in cellular processes and pathogenic states remains pivotal to our understanding of such states. Nevertheless, the temporal measurement of protein-protein interactions has remained difficult and proven to be a bottleneck for elucidating the mechanistic origin of these disease states. In this chapter, we have presented an approach utilizing a two-stage enrichment strategy to temporally resolve protein-protein interactions implicated in PQC. Our novel TRIP approach will aid in the deconvolution previously established PQC mechanisms for Tg processing while also providing new paradigms within PQC pathways still being characterized.

It is well established that several misfolding prone Tg mutation undergo increased retention and subsequent interactions across several protein quality control pathways. Including Hspa5, Hsp90b1, Hyou1, Pdia3, Pdia4, and Canx amongst others<sup>37,63,64</sup>. Here

we have been able to resolve the timing in which the increased engagement with these components takes place. Our work in Chapter 2 identified unique alterations in the engagement of Tg with glycan processing components and showed how these alterations may lead to variable responses in Tg degradation by altering downstream engagement with ERAD processing components. TRIP has allowed us to further identify and resolve unique temporal changes with these glycan processing components including Stt3b, Canx, Calr, and Ugg1 from WT to mutant Tg. These changes subsequently correlate with altered engagement with ERAD components Edem3, Os9, Sel1l, and Vcp. Moreover, we identified a broader scope of Tg interactors in thyroid tissue, including ER-phagy receptors At13, Ccpg1, and Rtn3. Our data set in Chapter 2 identified several autophagic and lysosomal components, but Tg degradation through ER-phagy or some other lysosome-dependent mechanisms was not established at the time. Identification of these receptors brings about a direct link from Tg processing to ER-phagy or ERLAD as degradation mechanisms. The crosstalk between ERAD, and ER-phagy has long been established<sup>65-67</sup>. Additionally, glycan dependent and independent mechanisms have been established for the degradation of ERAD resistant ER clients<sup>52,68</sup>. This overlap in degradation pathways may be similarly at play in the case of Tg biogenesis and processing, especially for mutants forming difficult to degrade aggregates<sup>37,47,48,69</sup>

Overall, the data presented here further clarifies previous work in understanding Tg processing, an area of research that has remained stagnant, and PQC mechanisms on the whole. Our TRIP approach uniquely provides insights and the ability to form new



hypotheses into novel mechanisms that can be further investigated. For example, areas within this dataset worth further investigation include expounding upon unique changes of select interactors within established pathways for Tg such as Hsp70/90 chaperoning and disulfide/redox processing, along with more unique discoveries within prolyl isomerization and hydroxylation, trafficking, and ribosomal quality control for Tg. With that being said, the data presented in Chapter 3 is still correlative in nature and does not definitively explain the mechanistic origin of the CH protein folding disease state. To achieve this, the functional implications of these interactions must be investigated and characterized. This led us to pursue the work described in Chapter 4, and bolster our findings presented in this chapter.

### **3.5 Acknowledgements**

M.T.W. was supported by the National Science Foundation – Graduate Research Fellowship Program. This work was also funded by an NIGMS R35 award (1R35GM133552). This content is solely the responsibility of the authors and does not necessarily represent the official views of the National Institutes of Health.

M.T.W. and L.P. designed experiments. M.T.W performed TRIP experiments.

### **3.6 Experimental Methods**

### *3.6.1 Plasmid Production and Antibodies*

Tg-FLAG in pcDNA3.1+/C-(K)-DYK plasmid was purchased from Genscript (Clone ID OHu20241). The Tg-FLAG gene was then amplified and assembled with an empty pcDNA5/FRT expression vector using a HiFi DNA assembly kit (New England BioLabs, E2621). This plasmid then underwent site-directed mutagenesis to produce pcDNA5-C1264R-Tg-FLAG, and pcDNA5-A2234D-Tg-FLAG plasmids (Table B.2).

### *3.6.2 Cell Line Engineering*

FRT cells were cultured in Ham's F-12, Coon's Modification (F12) media (Sigma, cat. No. F6636) supplemented with 5% fetal bovine serum (FBS), and 1% penicillin (10,000U) / streptomycin (10,000 µg/mL). To generate FRT flp-Tg-FT cells,  $5 \times 10^5$  cells cultured for 1 day were cotransfected with 2.25 µg flp recombinase pOG44 plasmid and 0.25 µg of FT-Tg pcDNA5 plasmid using Lipofectamine 3000. Cells were then cultured in media containing Hygromycin B (100 µg/mL) to select site specific recombinants. Resistant clonal lines were sorted into single cell colonies using flow cytometry and screened for FT-Tg expression (Figure B.1A and B.1B; Table B.2).

### *3.6.3 Time-Resolved Interactome Profiling*

Fully confluent 15cm tissue culture plates were used. Cells were washed with phosphate buffered saline (PBS) and depleted of methionine by incubating with methionine free Dulbecco's Modified Eagle Medium (DMEM) supplemented with 5% dialyzed fetal bovine serum (FBS), 1% L-glutamine (2mM final concentration), 1% L-cysteine (200  $\mu$ M final concentration), and 1% penicillin (10,000U) / streptomycin (10,000  $\mu$ g/mL) for 30 minutes. Cells were then pulse labeled with Hpg-enriched DMEM supplemented with with 1% Hpg (200 $\mu$ M final concentration), 5% dialyzed FBS, 1% L-glutamine (200mM final concentration), 1% L-cysteine (200 $\mu$ M), and 1% penicillin (10,000U) / streptomycin (10,000  $\mu$ g/mL) for 1 hour. After pulse labeling cells were washed with F12 media containing 10-fold excess methionine (2mM final concentration). Cells were then cultured in normal F12 media supplemented with 5% FBS and chased for the specified time-points. Cells were harvested by washing with PBS and then crosslinking with 0.5mM DSP in PBS at 37°C for 10 minutes. Crosslinking was quenched by the addition of 100mM Tris pH 7.5 at 37°C for 5 minutes. Lysates were prepared by lysing in Radioimmunoprecipitation assay (RIPA) buffer (50mM Tris pH 7.5, 150mM NaCl, 0.1% SDS, 1% Tri-ton X-100, 0.5% deoxycholate) with protease inhibitor cocktail (Roche, 4693159001). Protein concentration was normalized to 1mg/mL using a BCA assay (Thermo Scientific, 23225) and cell lysates underwent click reactions with the addition of 0.8mM copper sulfate (diluted from a 20mM stock in water), 1.6mM BTAA (diluted from a 40mM stock in water), 5mM sodium ascorbate (diluted from a 100mM stock), and 100 $\mu$ M TAMRA-Azide-PEG-Desthiobiotin ligand (diluted from a 5mM stock in DMSO). Samples were allowed to react at 37° for 1 hours while shaking at 750rpm. Cell lysates

were then precleared on 4B sepharose beads (Sigma, 4B200) at 4°C for 1 hour while rocking. Precleared lysates were immunoprecipitated with G1 Anti-DYKDDDDK affinity resin overnight at 4°C while rocking. Resin was washed four times with RIPA buffer, and proteins were eluted twice in 100µL immunoprecipitation elution buffer (2% SDS in PBS) by heating at 95°C for 5 minutes. Eluted samples from FLAG immunoprecipitations were then diluted with PBS to reduce the final SDS concentration to 0.2%. The solutions then underwent streptavidin enrichment with high-capacity streptavidin agarose resin (Pierce, 20359) for 2 hours at room temperature while rotating. The beads were then washed with 1mL each of 1% SDS, 4M Urea, 1M sodium chloride, followed by a final wash with 1% SDS (all wash buffers dissolved in PBS). Samples were then eluted twice with 100µL biotin elution buffer (50mM Biotin in 1% SDS in PBS) by heating at 37°C and shaking at 750rpm for 1 hour. Eluted streptavidin enrichment samples were precipitated in methanol/chloroform, washed three times with methanol, and air dried. Protein pellets were then resuspended in 3uL 1% Rapigest SF Surfactant (Waters, 186002122) followed by the addition of 10uL of 50mM HEPES pH 8.0, and 32.5uL of water. Samples were reduced with 5mM tris(2-carboxyethyl)phosphine (TCEP) (Sigma, 75259) at room temperature for 30 minutes and alkylated with 10mM iodoacetimide (Sigma, I6125) in the dark at room temperature for 30 minutes. Proteins were digested with 0.5 µg of Trypsin/Lys-C protease mix (Pierce, A40007) by incubating for 16-18 hours at 37°C, shaking at 750rpm. Peptides were reacted with TMTpro 16plex reagents (Thermo Fisher, 44520) in 40% v/v acetonitrile and incubated for one hour at room temperature. Reactions were quenched by the addition of ammonium bicarbonate (0.4% w/v final concentration)

and incubated for one hour at room temperature. TMT labeled samples were then pooled and acidified with 5% formic acid (Fisher, A117, v/v). Samples were concentrated using a speedvac and resuspended in buffer A (97% water, 2.9% acetonitrile, and 0.1% formic acid, v/v/v). Cleaved Rapigest SF surfactant was removed by centrifugation for 30 minutes at 21,100 x g.

### *3.6.4 Liquid Chromatography – Tandem Mass Spectrometry*

MudPIT microcolumns were prepared as previously described<sup>71</sup>. Peptide samples were directly loaded onto the columns using a high-pressure chamber. Samples were then desalted for 30 minutes with buffer A (97% water, 2.9% acetonitrile, 0.1% formic acid v/v/v). LC-MS/MS analysis was performed using an Exploris480 (Thermo Fisher) mass spectrometer equipped with an Ultimate3000 RSLCnano system (Thermo Fisher). MudPIT experiments were performed with 10µL sequential injections of 0, 10, 30, 60, and 100% buffer C (500mM ammonium acetate in buffer A), followed by a final injection of 90% buffer C with 10% buffer B (99.9% acetonitrile, 0.1% formic acid v/v) and each step followed by a 140 minute gradient from 4% to 80% B with a flow rate of 500nL/minute on a 20cm fused silica microcapillary column (ID 100 µm) ending with a laser-pulled tip filled with Aqua C18, 3µm, 125 Å resin (Phenomenex). Electrospray ionization (ESI) was performed directly from the analytical column by applying a voltage of 2.2kV with an inlet capillary temperature of 275°C. Data-dependent acquisition of mass spectra was carried out by performing a full scan from 400-1600m/z at a resolution of 120,000. Top-speed

data acquisition was used for acquiring MS/MS spectra using a cycle time of 3 seconds, with a normalized collision energy of 32, 0.4m/z isolation window, automatic maximum injection time and 100% normalized AGC target, at a resolution of 45,000 and a defined first mass (m/z) starting at 110. Peptide identification and TMT-based protein quantification was carried out using Proteome Discoverer 2.4. MS/MS spectra were extracted from Thermo Xcalibur .raw file format and searched using SEQUEST against a Uniprot rat proteome database supplemented with the human thyroglobulin gene (accessed 03/2014 and containing 28860 entries). The database was curated to remove redundant protein and splice-isoforms. Searches were carried out using a decoy database of reversed peptide sequences and the following parameters: 20ppm peptide precursor tolerance, 0.02 Da fragment mass tolerance, minimum peptide length of 6 amino acids, trypsin cleavage with a maximum of two missed cleavages, dynamic methionine modification of +15.995 Da (oxidation), dynamic protein N-terminus +42.011 Da (acetylation), -131.040 (methionine loss), -89.030 (methionine loss + acetylation), static cysteine modification of +57.0215 Da (carbamidomethylation), and static peptide N-terminal and lysine modifications of +304.2071 Da (TMTpro 16plex).

### *3.6.5 Immunoblotting and SDS-PAGE*

Cell lysates were prepared by lysing in RIPA buffer with protease inhibitor cocktail (Roche) and protein concentrations were normalized using a BCA assay (Thermo Scientific). Lysates were then denatured with 1X Laemmli buffer + 100mM DTT and

heated at 95°C for 5 minutes before being separated by SDS-PAGE. Samples were transferred onto poly-vinylidene difluoride (PVDF) membranes (Millipore, IPFL00010) for immunoblotting and blocked using 5% non-fat dry milk dissolved in tris buffered saline with 0.1% Tween-20 (Fisher, BP337-100) (TBS-T). Primary antibodies were incubated either at room temperature for 2 hours, or overnight at 4°C. Membranes were then washed three times with TBS-T and incubated with secondary antibody in 5% non-fat dry milk dissolved in TBS-T either at room temperature for 1 hour or overnight at 4°C. Membranes were washed three times with TBS-T and then imaged using a ChemiDoc MP Imaging System (BioRad). Primary antibodies were acquired from commercial sources and used at the indicated dilutions in immunoblotting buffer (5% bovine serum albumin (BSA) in Tris-buffered saline pH 7.5, 0.1% Tween-20, and 0.1% sodium azide): KDEL (1:1000), M2 anti-FLAG (1:1000), PDIA4 (1:1000), GAPDH (1:1000), hFAB  $\beta$ -Tubulin-Rhodamine (1:10000). Secondary antibodies were obtained from commercial sources and used at the indicated dilutions in 5% milk in Tris-buffered saline pH 7.5, 0.1% Tween-20 (TBS-T): Goat anti-mouse Star-bright700 (1:10000), Goat anti-rabbit IRDye800 (1:10000).

### *3.6.6 Mass Spectrometry Interactomics and TMT Quantification*

To identify Tg interactors (-) biotin pulldown vs(-) Hpg samples were processed using the DEP pipeline<sup>72</sup>. Enriched proteins were determined based on those with a log<sub>2</sub> fold change of  $2\sigma$  and benjamini-hochberg adjusted p-value (false discovery rate) of 0.05. For

pathway enrichment analysis of identified proteins, EnrichR was used and GO Cellular Component and Molecular Function 2018 terms were used to differentiate secretory pathway associated proteins from background<sup>73</sup>. For time resolved analysis, data were processed in R manually. Inconsistencies in the enrichment of Tg bait protein were observed for replicate 5 of WT Tg, and this replicate was excluded from time-resolved analysis. Briefly, TMT abundances across chase samples were normalized to Tg TMT abundance as described previously and compared to (-) Hpg samples for enrichment analysis<sup>8</sup>. All analysis scripts are available as described in the Data and Code Availability section.

### *3.6.7 Data and Code Availability*

The dataset used for the mass spectrometry interactome characterization experiments showing protein identification and quantification are included in File B.1 and B.2. Mass spectrometry spectrum and result files are available via ProteomeXchange under identifier PXD035681. Code used for data analysis and generation of figures is available at [github.com/wrighmt1/2022\\_TRIP](https://github.com/wrighmt1/2022_TRIP).

## **3.7 References**

1. Bludau, I. & Aebersold, R. Proteomic and interactomic insights into the molecular basis of cell functional diversity. *Nature Reviews Molecular Cell Biology* **21**, 327–340 (2020).



2. Karagöz, G. E., Acosta-Alvear, D. & Walter, P. The Unfolded Protein Response: Detecting and Responding to Fluctuations in the Protein-Folding Capacity of the Endoplasmic Reticulum. *Cold Spring Harb Perspect Biol* a033886 (2019).
3. Needham, P. G., Guerriero, C. J. & Brodsky, J. L. Chaperoning Endoplasmic Reticulum-Associated Degradation (ERAD) and Protein Conformational Diseases. *Cold Spring Harb Perspect Biol* a033928 (2019).
4. Behnke, J., Mann, M. J., Scruggs, F.-L., Feige, M. J. & Hendershot, L. M. Members of the Hsp70 Family Recognize Distinct Types of Sequences to Execute ER Quality Control. *Molecular Cell* **63**, 739–752 (2016).
5. Pohl, C. & Dikic, I. Cellular quality control by the ubiquitin-proteasome system and autophagy. *Science* (1979) **366**, 818–822 (2019).
6. Taldone, T. *et al.* A Chemical Biology Approach to the Chaperome in Cancer—HSP90 and Beyond. *Cold Spring Harbor Perspectives in Biology* **12**, a034116 (2020).
7. McDonald, E. F., Sabusap, C. M. P., Kim, M. & Plate, L. Distinct proteostasis states drive pharmacologic chaperone susceptibility for Cystic Fibrosis Transmembrane Conductance Regulator misfolding mutants. *Molecular Biology of the Cell* (2022).
8. Wright, M. T., Kouba, L. & Plate, L. Thyroglobulin Interactome Profiling Defines Altered Proteostasis Topology Associated With Thyroid Dysmorphogenesis. *Molecular & Cellular Proteomics* **20**, 100008 (2021).
9. Kuo, C. C., Chiang, A. W. T., Baghdassarian, H. M. & Lewis, N. E. Dysregulation of the secretory pathway connects Alzheimer’s disease genetics to aggregate formation. *Cell Systems* **12**, 873–884.e4 (2021).
10. Marinko, J. T. *et al.* Glycosylation limits forward trafficking of the tetraspan membrane protein PMP22. *Journal of Biological Chemistry* **296**, (2021).
11. Wright, M. T. & Plate, L. Revealing functional insights into ER proteostasis through proteomics and interactomics. *Experimental Cell Research* **399**, (2021).
12. Rizzolo, K. & Houry, W. A. Multiple functionalities of molecular chaperones revealed through systematic mapping of their interaction networks. *Journal of Biological Chemistry* **294**, 2142–2150 (2019).
13. Rizzolo, K. *et al.* Features of the Chaperone Cellular Network Revealed through Systematic Interaction Mapping. *Cell Reports* **20**, 2735–2748 (2017).
14. Taipale, M. *et al.* Quantitative Analysis of Hsp90-Client Interactions Reveals Principles of Substrate Recognition. *Cell* **150**, 987–1001 (2012).
15. Taipale, M. *et al.* A Quantitative Chaperone Interaction Network Reveals the Architecture of Cellular Protein Homeostasis Pathways. *Cell* **158**, 434–448 (2014).
16. Piette, B. L. *et al.* Comprehensive interactome profiling of the human Hsp70 network highlights functional differentiation of J domains. *Molecular Cell* (2021).
17. Lobingier, B. T. *et al.* An Approach to Spatiotemporally Resolve Protein Interaction Networks in Living Cells. *Cell* **169**, 350–360.e12 (2017).
18. Perez Verdaguer, M. *et al.* Time-resolved proximity labeling of protein networks associated with ligand-activated EGFR. *Cell Reports* **39**, 110950 (2022).
19. Dieterich, D. C., Link, A. J., Graumann, J., Tirrell, D. A. & Schuman, E. M. Selective identification of newly synthesized proteins in mammalian cells using bioorthogonal

- noncanonical amino acid tagging (BONCAT). *Proceedings of the National Academy of Sciences* **103**, 9482–9487 (2006).
20. Bagert, J. D. *et al.* Quantitative, Time-Resolved Proteomic Analysis by Combining Bioorthogonal Noncanonical Amino Acid Tagging and Pulsed Stable Isotope Labeling by Amino Acids in Cell Culture. *Molecular & Cellular Proteomics* **13**, 1352–8 (2014).
  21. Ma, Y., McClatchy, D. B., Barkallah, S., Wood, W. W. & Yates, J. R. Quantitative analysis of newly synthesized proteins. *Nature Protocols* **13**, 1744–1762 (2018).
  22. McClatchy, D. B. *et al.* Pulsed Azidohomoalanine Labeling in Mammals (PALM) Detects Changes in Liver-Specific LKB1 Knockout Mice. *Journal of Proteome Research* **14**, 4815–4822 (2015).
  23. Ma, Y., McClatchy, D. B., Barkallah, S., Wood, W. W. & Yates, J. R. HILAQ: A Novel Strategy for Newly Synthesized Protein Quantification. *Journal of Proteome Research* **16**, 2213–2220 (2017).
  24. Howden, A. J. M. *et al.* QuaNCAT: quantitating proteome dynamics in primary cells. *Nature Methods* **10**, 343–6 (2013).
  25. van Bergen, W., Heck, A. J. R. & Baggelaar, M. P. Recent advancements in mass spectrometry-based tools to investigate newly synthesized proteins. *Current Opinion in Chemical Biology* **66**, (2021).
  26. Cortez, D. Proteomic Analyses of the Eukaryotic Replication Machinery. *Methods in Enzymology* **33–53** (2017).
  27. Sirbu, B. M. *et al.* Analysis of protein dynamics at active, stalled, and collapsed replication forks. *Genes & Development* **25**, 1320–1327 (2011).
  28. Munden, A. *et al.* Identification of replication fork-associated proteins in Drosophila embryos and cultured cells using iPOND coupled to quantitative mass spectrometry. *Scientific Reports* **12**, 1–11 (2022).
  29. Kim, B. *et al.* Discovery of Widespread Host Protein Interactions with the Pre-replicated Genome of CHIKV Using VIR-CLASP. *Molecular Cell* **78**, 624-640.e7 (2020).
  30. Phillips, S. L., Soderblom, E. J., Bradrick, S. S. & Garcia-Blanco, M. A. Identification of Proteins Bound to Dengue Viral RNA In Vivo Reveals New Host Proteins Important for Virus Replication. *mBio* **7**, (2016).
  31. Citterio, C. E., Targovnik, H. M. & Arvan, P. The role of thyroglobulin in thyroid hormonogenesis. *Nature Reviews Endocrinology* **15**, 323–338 (2019).
  32. Coscia, F. *et al.* The structure of human thyroglobulin. *Nature* **578**, 1–4 (2020).
  33. Kiick, K. L., Weberskirch, R. & Tirrell, D. A. Identification of an expanded set of translationally active methionine analogues in Escherichia coli. *FEBS Letters* **502**, 25–30 (2001).
  34. Beatty, K. E. *et al.* Fluorescence Visualization of Newly Synthesized Proteins in Mammalian Cells. *Angewandte Chemie International Edition* **45**, 7364–7367 (2006).
  35. Li, J. *et al.* TMTpro reagents: a set of isobaric labeling mass tags enables simultaneous proteome-wide measurements across 16 samples. *Nature Methods* **17**, 399–404 (2020).

36. Thompson, A. *et al.* TMTpro: Design, Synthesis, and Initial Evaluation of a Proline-Based Isobaric 16-Plex Tandem Mass Tag Reagent Set. *Analytical Chemistry* **91**, 15941–15950 (2019).
37. Menon, S. *et al.* Oxidoreductase Interactions Include a Role for ERp72 Engagement with Mutant Thyroglobulin from the rdw/rdw Rat Dwarf. *Journal of Biological Chemistry* **282**, 6183–6191 (2007).
38. Baryshev, M. *et al.* Unfolded protein response is involved in the pathology of human congenital hypothyroid goiter and rat non-goitrous congenital hypothyroidism. *J Mol Endocrinol* **32**, 903–920.
39. Kim, P. S. & Arvan, P. Calnexin and BiP act as sequential molecular chaperones during thyroglobulin folding in the endoplasmic reticulum. *J Cell Biol* **128**, 29–38 (1995).
40. Hishinuma, A. *et al.* Two Novel Cysteine Substitutions (C1263R and C1995S) of Thyroglobulin Cause a Defect in Intracellular Transport of Thyroglobulin in Patients with Congenital Goiter and the Variant Type of Adenomatous Goiter1. *The Journal of Clinical Endocrinology & Metabolism* **84**, 1438–1444 (1999).
41. Kanou, Y. *et al.* Thyroglobulin Gene Mutations Producing Defective Intracellular Transport of Thyroglobulin Are Associated with Increased Thyroidal Type 2 Iodothyronine Deiodinase Activity. *The Journal of Clinical Endocrinology & Metabolism* **92**, 1451–1457 (2007).
42. Tsai, C.-F. *et al.* An Improved Boosting to Amplify Signal with Isobaric Labeling (iBASIL) Strategy for Precise Quantitative Single-cell Proteomics. *Molecular & Cellular Proteomics* **19**, 828–838 (2020).
43. Petelski, A. A. *et al.* Multiplexed single-cell proteomics using SCoPE2. *Nature Protocols* **16**, 5398–5425 (2021).
44. Chitwood, P. J. & Hegde, R. S. An intramembrane chaperone complex facilitates membrane protein biogenesis. *Nature* **584**, 630–634 (2020).
45. McGilvray, P. T. *et al.* An ER translocon for multi-pass membrane protein biogenesis. *Elife* **9**, 1–43 (2020).
46. Shurtleff, M. J. *et al.* The ER membrane protein complex interacts cotranslationally to enable biogenesis of multipass membrane proteins. *Elife* **7**, (2018).
47. di Jeso, B. *et al.* Mixed-Disulfide Folding Intermediates between Thyroglobulin and Endoplasmic Reticulum Resident Oxidoreductases ERp57 and Protein Disulfide Isomerase. *Molecular and Cellular Biology* **25**, 9793–9805 (2005).
48. di Jeso, B. *et al.* Transient Covalent Interactions of Newly Synthesized Thyroglobulin with Oxidoreductases of the Endoplasmic Reticulum\*. *Journal of Biological Chemistry* **289**, 11488–11496 (2014).
49. Baryshev, M., Sargsyan, E. & Mkrtchian, S. ERp29 is an essential endoplasmic reticulum factor regulating secretion of thyroglobulin. *Biochemical and Biophysical Research Communications* **340**, 617–624 (2006).
50. Christianson, J. C., Shaler, T. A., Tyler, R. E. & Kopito, R. R. OS-9 and GRP94 deliver mutant  $\alpha$ 1-antitrypsin to the Hrd1–SEL1L ubiquitin ligase complex for ERAD. *Nature Cell Biology* **10**, 272–282 (2008).

51. Christianson, J. C. *et al.* Defining human ERAD networks through an integrative mapping strategy. *Nature Cell Biology* **14**, 93–105 (2012).
52. Fregno, I., Fasana, E., Soldà, T., Galli, C. & Molinari, M. N-glycan processing selects ERAD-resistant misfolded proteins for ER-to-lysosome-associated degradation. *The EMBO Journal* e107240 (2021).
53. Chiritoiu, M. *et al.* EDEM1 Drives Misfolded Protein Degradation via ERAD and Exploits ER-Phagy as Back-Up Mechanism When ERAD Is Impaired. *International Journal of Molecular Sciences* **21**, (2020).
54. Fregno, I. *et al.* ER-to-lysosome-associated degradation of proteasome-resistant ATZ polymers occurs via receptor-mediated vesicular transport. *The EMBO Journal* **37**, (2018).
55. Lamriben, L., Graham, J. B., Adams, B. M. & Hebert, D. N. N-Glycan-based ER Molecular Chaperone and Protein Quality Control System: The Calnexin Binding Cycle. *Traffic* **17**, 308–326 (2016).
56. Forrester, A. *et al.* A selective ER-phagy exerts procollagen quality control via a Calnexin-FAM134B complex. *The EMBO Journal* **38**, (2019).
57. Chen, Y. J. *et al.* PGRMC1 acts as a size-selective cargo receptor to drive ER-phagic clearance of mutant prohormones. *Nature Communications* **12**, (2021).
58. Cunningham, C. N. *et al.* Cells Deploy a Two-Pronged Strategy to Rectify Misfolded Proinsulin Aggregates. *Molecular Cell* **75**, 442-456.e4 (2019).
59. Chen, Q. *et al.* ATL3 Is a Tubular ER-Phagy Receptor for GABARAP-Mediated Selective Autophagy. *Curr Biol* **29**, 846-855.e6 (2019).
60. Liang, J. R., Lingeman, E., Ahmed, S. & Corn, J. E. Atlastins remodel the endoplasmic reticulum for selective autophagy. *Journal of Cell Biology* **217**, 3354–3367 (2018).
61. Smith, M. D. *et al.* CCPG1 Is a Non-canonical Autophagy Cargo Receptor Essential for ER-Phagy and Pancreatic ER Proteostasis. *Developmental Cell* **44**, 217-232.e11 (2018).
62. Grumati, P. *et al.* Full length RTN3 regulates turnover of tubular endoplasmic reticulum via selective autophagy. *Elife* **6**, e25555 (2017).
63. Muresan, Z. & Arvan, P. Thyroglobulin transport along the secretory pathway. Investigation of the role of molecular chaperone, GRP94, in protein export from the endoplasmic reticulum. *J Biol Chem* **272**, 26095–102 (1997).
64. Kim, P. S., Kwon, O. Y. & Arvan, P. An endoplasmic reticulum storage disease causing congenital goiter with hypothyroidism. *J Cell Biol* **133**, 517–27 (1996).
65. Pohl, C. & Dikic, I. Cellular quality control by the ubiquitin-proteasome system and autophagy. *Science (1979)* **366**, 818–822 (2019).
66. Khaminets, A. *et al.* Regulation of endoplasmic reticulum turnover by selective autophagy. *Nature* **522**, 354–358 (2015).
67. Molinari, M. ER-phagy responses in yeast, plants, and mammalian cells and their crosstalk with UPR and ERAD. *Developmental Cell* (2021).
68. He, L. *et al.* DNAJB12 and Hsp70 triage arrested intermediates of N1303K-CFTR for endoplasmic reticulum-associated autophagy. *Mol Biol Cell* **32**, 538–553 (2021).

69. Kim, P. S., Kim, K. R. & Arvan, P. Disulfide-linked aggregation of thyroglobulin normally occurs during nascent protein folding. *American Journal of Physiology-Cell Physiology* **265**, C704–C711 (1993).
70. Lang, K. & Chin, J. W. Cellular Incorporation of Unnatural Amino Acids and Bioorthogonal Labeling of Proteins. *Chemical Reviews* **114**, 4764–4806 (2014).
71. Fonslow, B. R. *et al.* Single-step inline hydroxyapatite enrichment facilitates identification and quantitation of phosphopeptides from mass-limited proteomes with MudPIT. *Journal of Proteome Research* **11**, 2697–2709 (2012).
72. Zhang, X. *et al.* Proteome-wide identification of ubiquitin interactions using UblA-MS. *Nature Protocols* **2018** 13:3 **13**, 530–550 (2018).
73. Chen, E. Y. *et al.* Enrichr: interactive and collaborative HTML5 gene list enrichment analysis tool. *BMC Bioinformatics* **14**, 128 (2013).

## **Investigating the Functional Implications of Protein Quality Control Components on Thyroglobulin Processing\***

### **4.1 Introduction**

The functional implications of protein-protein interactions can be difficult to deduce, especially in the case of protein quality control (PQC) mechanisms containing several layers of redundancy across stress response pathways, protein homologs, and multiple unique proteins sharing similar functions<sup>1-4</sup>. As such, studies like those found in Chapters 2 and 3 are often accompanied by functional follow-up or validation to reveal what implications these protein-protein interactions have on the cellular process at hand<sup>5-7</sup>. There have also been several investigations taking a more agnostic approach to investigate these functional consequences by performing network wide genetic screens<sup>8-10</sup>. Such screens often utilize classical RNA interference (RNAi) techniques with small interfering (siRNA) or short hairpin (shRNA), or more modern approaches utilizing CRISPR interference (CRISPRi) or CRISPR knockouts and single guide RNA (sgRNA) to repress or fully delete the expression of a given protein or gene product.

---

\* This chapter contains material adapted from the submitted research article: “Time-Resolved Interactome Profiling Deconvolutes Secretory Protein Quality Control Dynamics” by Madison T. Wright, Bibek Timalsina, Valeria Garcia Lopez, & Lars Plate. It has been reproduced with the permission of the publisher and co-authors.

The goal of these investigations is always to move away from a correlative measurement or understanding of these interactions and towards a more comprehensive understanding of protein function and activity. These validation studies have allowed for identification of both pro-degradation and pro-retention mechanisms implicated not only in ER-associated (ERAD) on the whole, but specific sub pathway mechanisms for luminal and membrane bound substrates with structural insults within the membrane or cytosolic side of the protein interface <sup>11,12</sup>. Similar approaches have also allowed for the discovery and characterization of receptors for autophagy at the ER (ER-phagy) and ER-phagy mechanisms<sup>13-15</sup>. Beyond degradation pathways, these validation studies also allowed for the characterization of the ER membrane protein complex (EMC) to be functionally characterized, revealing roles across protein folding, ERAD, ER-phagy, and lipid transfer, amongst others<sup>16</sup>. Similarly, these studies have been used to characterize disease specific protein functions in cystic fibrosis, Charcot-Marie-Tooth disease, aging and neurodegeneration<sup>5,6,17,18</sup>,

In an effort to compliment and further validate the data presented in Chapters 2 and 3, we sought to develop a screening platform to monitor the functional implications of thyroglobulin (Tg) interactors and other PQC components on the whole. We utilized a nanoluciferase (NLuc)-based Tg secretion assay and performed a primary siRNA screen in HEK293 cells, followed up by further validation in Fischer rat thyroid (FRT) cells. Our siRNA screening platform allowed us to identify several PQC components that modulate

Tg processing, altering retention and secretion. Of note, we find that Vcp and Tex264 are two key regulators of Tg degradation and their inhibition results in rescued secretion of mutant Tg in a mutation specific manner. Furthermore, we find that pharmacological Vcp inhibition recapitulates these results, and Tg constructs are differential enriched with Tex264 in cells. These data corroborate our findings from Chapters 2 and 3 and provide a larger picture of the pathogenicity of congenital hypothyroidism (CH) and dysmorphogenesis.

#### **4.2 siRNA screening deconvolutes interactions and key regulators of construct specific Tg processing**

To investigate and better comprehend the functional implications of Tg interactors and other PQC components we developed an RNA interference (RNAi) screening platform. Moreover, we hoped to identify factors whose modulation may act to rescue mutant Tg secretion. We engineered HEK293 cells to stably express nanoluciferase-tagged Tg constructs (Tg-NLuc) and screened against 167 Tg interactors and related PN components (Figure 4.1A)<sup>19</sup>. The NLuc tag allows us to monitor changes to both intracellular Tg abundance, and Tg secretion rates in a 96-well format for higher throughput. The NLuc-tag did not alter the secretion of WT Tg and maintained the same secretion deficiency observed for CH-associated mutants (Figure C.1). We identified 4 genes whose silencing modulated Tg-NLuc abundance in lysate (Figure 4.1B; Figure C.2). More specifically, silencing of NAPA ( $\alpha$ -SNAP) and LMAN1 were found to increase



WT Tg-NLuc lysate abundance in a construct specific manner.  $\alpha$ -SNAP is a member of the NSF

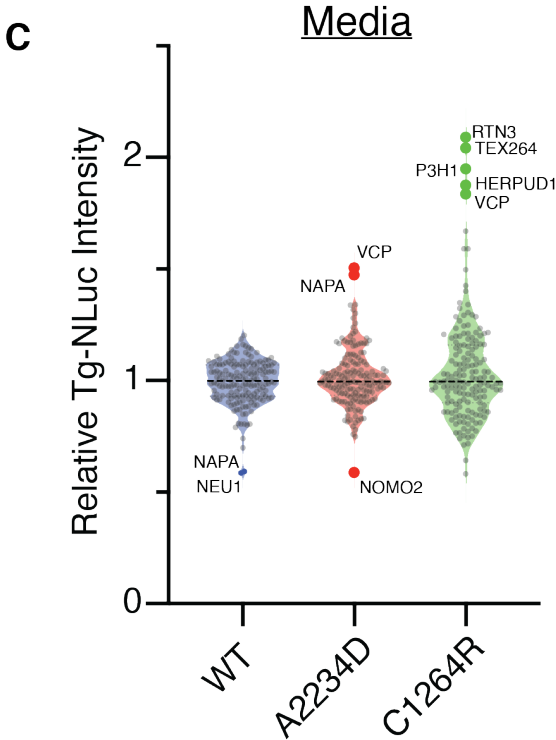
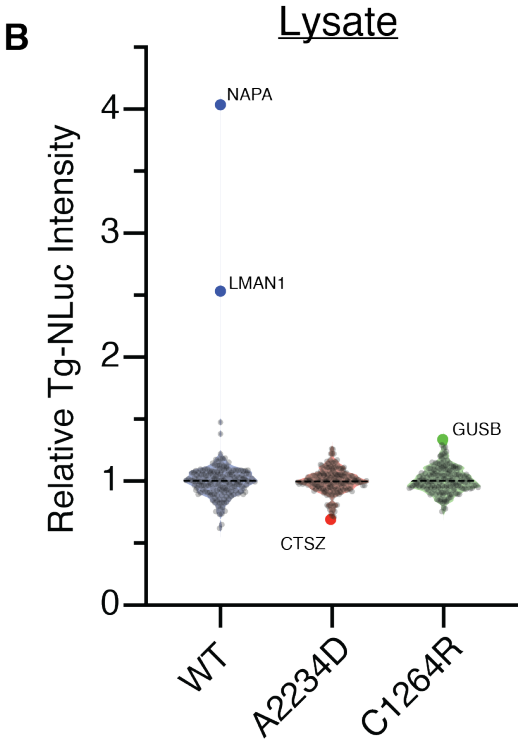
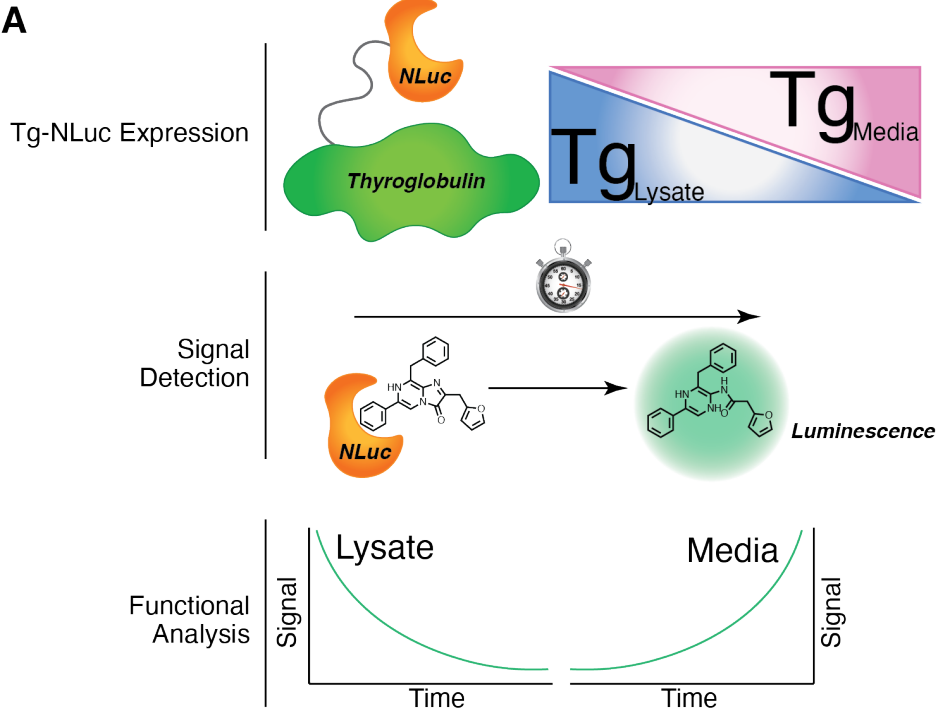


**Figure 4.1: siRNA Screening Deconvolutes Interactions and Key Regulators of Construct Specific Tg Processing**

(A) siRNA screening workflow utilizing NLuc-tagged Tg to monitor lysate and media abundance.

(B) Violin plots of siRNA hits found to alter Tg abundance in lysate. Cutoff criteria for hits were set to those genes that increased or decreased Tg-NLuc abundance in lysate or media by  $3\sigma$ .

(C) Violin plots of siRNA hits found to alter Tg secretion abundance in media. Cutoff criteria for hits were set to those genes that increased or decreased Tg-NLuc abundance in lysate or media by  $3\sigma$ .

attachment protein (SNAP) family and plays a critical role in vesicle fusion and docking,

while LMAN1 is a mannose-specific lectin that functions as a glycoprotein

cargo receptor for ER-to-Golgi transport<sup>17,20,21</sup>. For mutant Tg-NLuc constructs we found

that CTSZ silencing decreased A2234D Tg-NLuc lysate abundance, while GUSB

silencing increased C1264R lysate abundance (Figure 4.1B). CTSZ and GUSB, are both

lysosomal enzymes, with CTSZ acting as a cysteine-protease and GUSB as a hydrolase

targeting polysaccharide structures. CTSZ is commonly involved in protein degradation

and involved in cell signaling, although it is not clear what roll it may play in Tg-NLuc

processing as RNAi leads to decreased lysate abundance<sup>22,23</sup>. Additionally, it is not clear

what roll GUSB may play in the context of Tg-NLuc processing as it is involved in

glycosaminglycan degradation but has not been identified to play a role in the context of

protein processing or degradation<sup>24</sup>.

When monitoring Tg-NLuc secretion we identified 8 genes whose silencing, led to

differential changes in Tg-NLuc secretion (Figure 4.1C; Figure C.2). Silencing of  $\alpha$ -SNAP,

NEU1, and NOMO2 led to a decrease in Tg-NLuc secretion, with  $\alpha$ -SNAP & NEU1

affecting WT, and NOMO2 affecting A2234D in a construct specific manner. Silencing of

$\alpha$ -SNAP leading to a decrease in secretion complements the results we found where WT lysate levels increased with  $\alpha$ -SNAP silencing. NEU1 is a lysosomal enzyme that cleaves terminal sialic acid residues on proteins and lipid species<sup>25,26</sup>. Tg contains terminal sialic residues once it has undergone glycan maturation through the golgi complex, yet it is unclear how silencing of NEU1 might decrease secretion of WT Tg<sup>27</sup>. NOMO2 is one of the three homologs of the NOMO gene with each homolog sharing high amino acid sequence identity and believed to share similar functions with NOMO recently identified as a component of the TMCO1-ribosome complex/translocon involved in membrane protein biogenesis and found to be a close interactor with ER-phagy receptor TEX264<sup>28,29</sup>.

Remarkably, we were able to identify 6 genes whose silencing rescued mutant Tg-NLuc secretion in a construct specific manner.  $\alpha$ -SNAP silencing was able to increase secretion of A2234D Tg-NLuc. This contrast to the reduction in WT secretion may suggest an alternative role for  $\alpha$ -SNAP in regulating mutant Tg processing as other proteins involved in vesicular fusion and trafficking have been implicated in ER-phagy previously<sup>10,30</sup>. Silencing of LEPRE1 (P3H1), an ER-resident prolyl hydroxylase, increased C1264R Tg-NLuc secretion but not WT or A2234D<sup>31</sup>. Silencing of several protein degradation genes robustly increased mutant Tg secretion. VCP silencing increased both A2234D and C1264R Tg-NLuc secretion (Figure 4.1C). As mentioned previously, VCP is largely associated with ERAD but also aids in several diverse cellular functions including the interplay between proteasomal and lysosomal degradation<sup>11,32,33</sup>. HERPUD1, TEX264 and RTN3 silencing increased C1264R secretion in a construct specific manner.

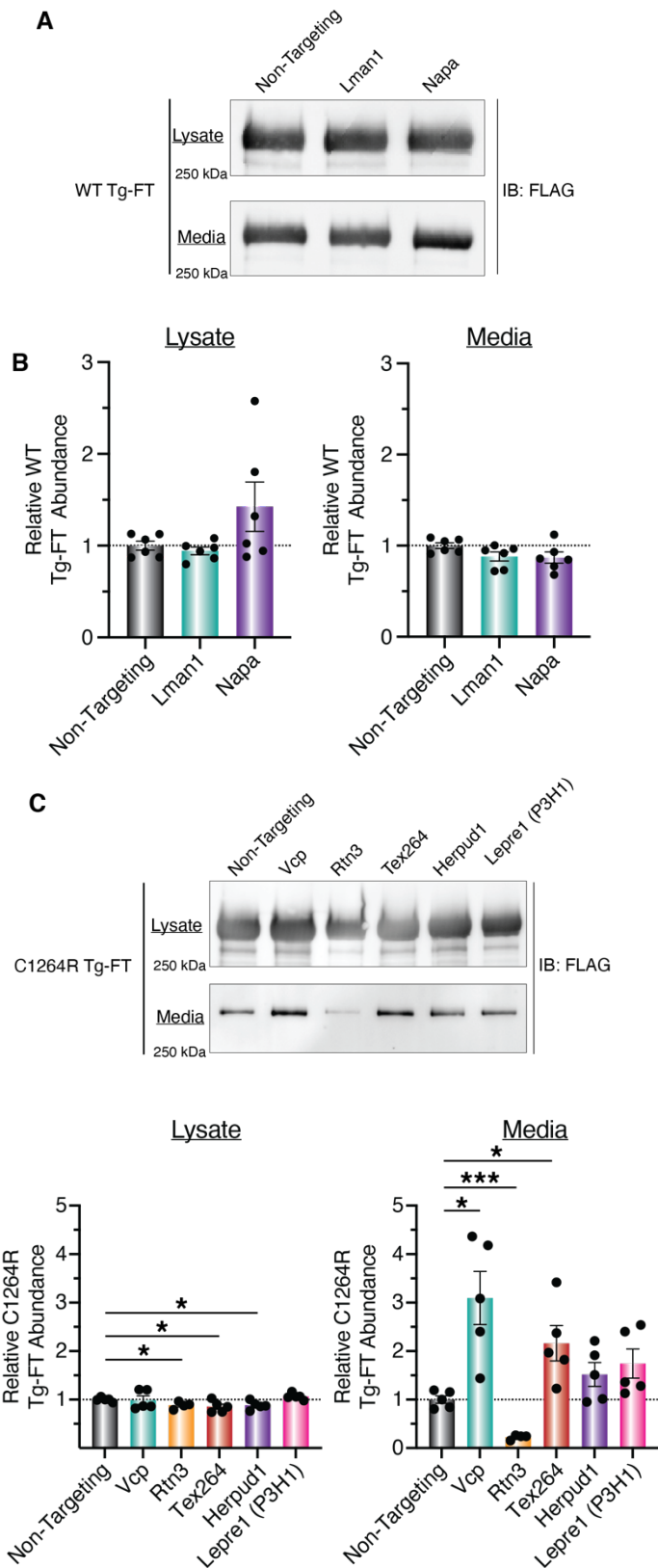
HERPUD1 is a ubiquitin like protein and associates with VCP during ERAD<sup>11,34,35</sup>. The ER-phagy receptors RTN3 and TEX264 localize to sub domains of the ER to facilitate degradation of specific ER clients and organellular regions<sup>15,29,36–39</sup>. Of note, while the ER-phagy receptor CCPG1 was identified in our mass spectrometry dataset, siRNA silencing did not significantly alter Tg abundance in lysate or media, nor did silencing of SEC62 or RETREG1 (FAM134B), two additional ER-phagy receptors found to regulate ER dynamics (Figure C.2).

This is the first study to broadly investigate the functional implications of Tg interactors and other PQC network components on Tg processing through RNAi screening. Particularly, with many of these components being involved in protein degradation our results may suggest that the blockage of degradation pathways can broadly rescue the secretion of A2234D and C1264R mutant Tg, a phenomenon similarly found in other protein folding diseases<sup>40</sup>.

### **4.3 Trafficking and degradation factors selectively regulate Tg processing in Thyroid cells**

We were curious if hits found in our siRNA screen exhibited similar phenotypes in thyroid specific tissue when silenced. We followed-up on the RNAi screening hits in FRT cells stably expressing Tg constructs. We first transfected WT Tg FRT cells with siRNAs

**Figure 4.2: Trafficking and Degradation Factors Selectively Regulate Tg Processing in FRT cells**  
 (A and B) Western blot analysis of WT Tg-FT transfected with respective siRNAs targeting select hits from initial siRNA screening data set. Statistical testing performed using an unpaired student's t-test with Welch's correction.  
 (C and D) Western blot analysis of C1264R Tg-FT transfected with respective siRNAs targeting select hits from initial siRNA screening data set. Statistical testing performed using an unpaired student's t-test with Welch's correction. \* $p < 0.05$ , \*\* $p < 0.005$ , \*\*\* $p < 0.0005$ .



targeting Lman1 and Napa ( $\alpha$ -SNAP) and monitored changes in Tg lysate and media abundance after 8 hours. We found that  $\alpha$ -SNAP silencing led to a 50% increase in WT Tg lysate abundance, while  $\alpha$ -SNAP and Lman1 silencing both led to marginal decreases in WT Tg secretion, with  $\alpha$ -SNAP silencing significantly increasing lysate retention by 15% and decreased secretion by 18% when monitored by  $^{35}\text{S}$  pulse-chase analysis (Figure 4.2A and 4.2B; Figure C.3A and C.3B; & Figure C.4A and C.4B).

Next, we transfected C1264R Tg FRT cells with siRNAs targeting Vcp, Rtn3, Tex264, Herpud1, and Lepre1 (P3H1) and similarly monitored Tg lysate and media abundance. Rtn3, Tex264, and Herpud1 silencing all significantly, yet marginally, decreased C1264R lysate abundance. Vcp and Tex264 silencing significantly increased C1264R secretion by 3-fold and 2-fold respectively, consistent with our results in HEK293T cells. In contrast, silencing of Rtn3 significantly decreased C1264R Tg secretion by 5-fold (Figure 4.2C and 4.2D; Figure C.4C – C.4E), which was the opposite to the increased secretion observed in HEK293T cells. We again turned to  $^{35}\text{S}$  pulse-chase assay to further monitor how the silencing of Tex264 and Vcp affected C1264R Tg processing. We diligently optimized the  $^{35}\text{S}$  assay protocol to detect changes in C1264R processing given 1) adaptive mechanisms upregulating ER chaperones, disulfide processing enzymes, and stress response pathways by thyroid cell lines to combat chronic stress from misfolded Tg accumulation 2) the sensitivity of Tex264 and Vcp function in stress response pathways that is exacerbated by siRNA silencing<sup>29,41,42</sup>. Given these two points, we anticipated that C1264R processing may be difficult to measure via  $^{35}\text{S}$  pulse-chase assay using siRNA

silencing. While the secretion phenotype for C1264R with Tex264 silencing was difficult to observe by <sup>35</sup>S pulse-chase assay, we found that Vcp silencing led to a 16% decrease in degradation, correlating with increased C1264R retention when monitored via <sup>35</sup>S pulse-chase assay (Figure C.4C – C.4F).

#### **4.4 Pharmacological VCP Inhibition Selectively Rescues C1264R Tg Secretion**

To address the conflicting results found with C1264R and siRNA silencing, we sought to investigate whether pharmacological modulation of select Tg processing components could lead to alterations in Tg secretion, particularly rescuing mutant Tg secretion. There are no selective inhibitors currently available for Tex264, but several for Vcp. We performed follow-up experiments using Vcp inhibitors ML-240, CB-5083, and NMS-873 and found treatment with ML-240 was able to significantly increase C1264R Tg secretion in FRT cells, corroborating our siRNA silencing data (Figure 4.3A and 4.3B)<sup>43–45</sup>. Further, Vcp inhibition in FRT cells with ML-240 did not alter C1264R Tg lysate abundance. To investigate whether this rescue of C1264R Tg secretion with ML-240 treatment was specific to C1264R Tg, we also monitored WT Tg abundance and found that ML-240 significantly reduced WT Tg abundance in both lysate and media after 4- & 8-hour treatments (Figure 4.3C and 4.3D).

We hypothesized that ML-240 treatment may differentially regulate Tg degradation and processing in a construct specific manner. We again turned to a <sup>35</sup>S pulse-chase assay to fully characterize Tg degradation and processing dynamics with ML-240 treatment and

found that lysate abundance of C1264R Tg was not significantly changed after 4-hours with ML-240 compared to DMSO treated cells (Figure 4.3E; Figure C.5A and C.5B). This parallels our results with VCP silencing, and ML-240 treatment under steady-state conditions in FRT cells. Excitingly, we found a 10-fold increase in C1264R Tg secretion after 4-hours with ML-240 compared to DMSO treated cells with no significant change in C1264R Tg degradation in the presence of ML-240 compared to DMSO treated cells (Figure 4.3E). Conversely, for WT Tg ML-240 treatment led to a significant increase in lysate abundance after 4 hours compared to DMSO (Figure 4.3F; Figure C.5C and C.5D). This increase in lysate abundance correlated with a strong and significant decrease in WT Tg secretion from 67% to 4% in the presence of ML-240 compared to DMSO treated cells without altering WT degradation.

#### **4.5 Pharmacological VCP Inhibition is Associated with Temporal Remodeling of the Tg Interactome**

We were curious if our TRIP method (see Chapter 3) was capable of capturing changes in interactions across PQC pathways that correlate with the rescued secretion of C1264R Tg, so we utilized our methodology with C1264R Tg in the presence of ML-240 and monitored temporal changes across key PQC pathways. We noticed that both glycan processing and Hsp70/90 chaperoning pathways exhibited broad decreases in C1264R Tg engagement in ML-240 compared to untreated samples (Figure 4.3G and 4.3H; Figure C.5E). Particularly, Canx and Ugg1 engagement tapered off earlier



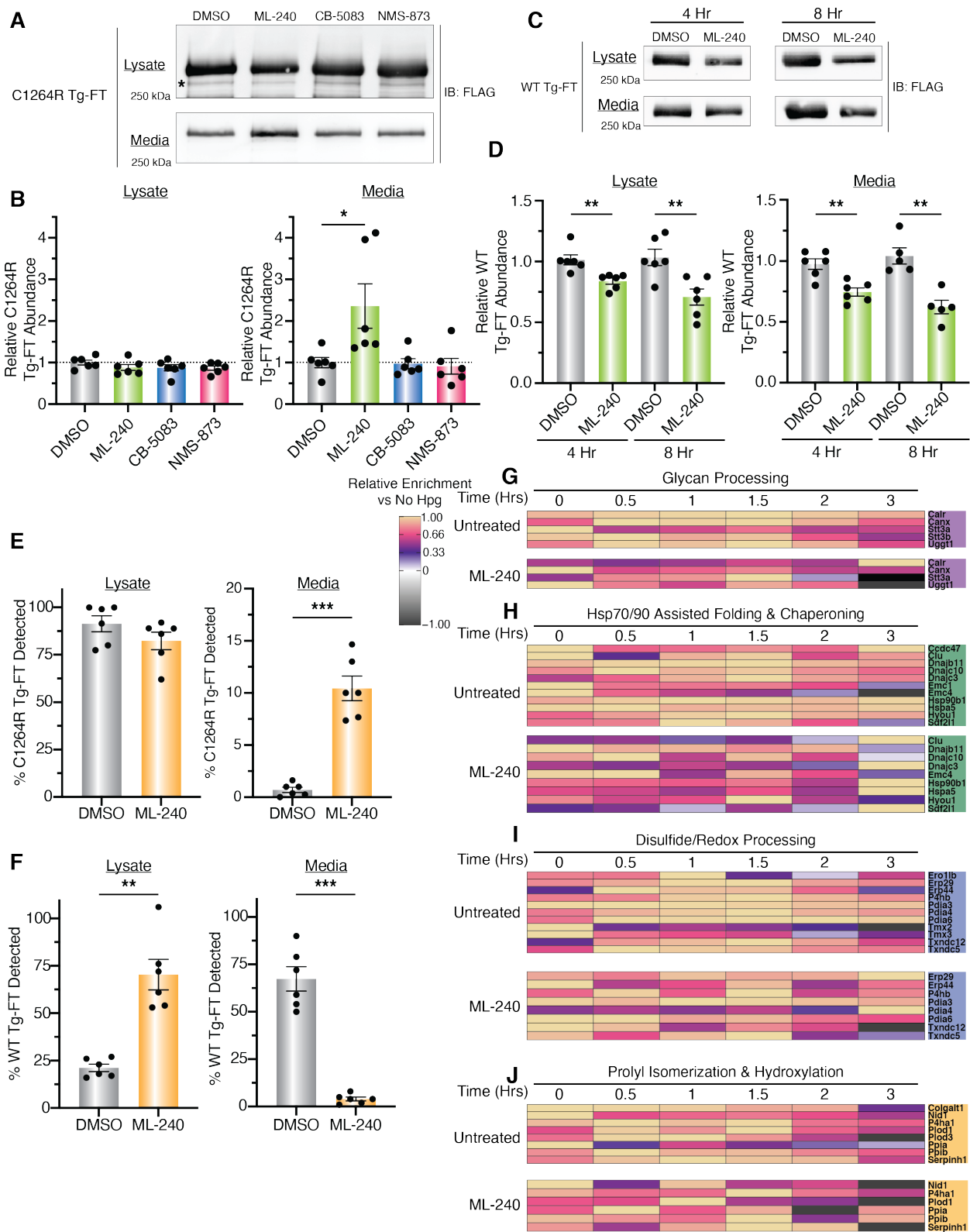


**Figure 4.3: Pharmacological VCP Inhibition Selectively Rescue C1264R Tg Secretion and is Associated with Interactome Remodeling**

(A and B) Western blots analysis of C1264R Tg-FT treated with various VCP inhibitors for 8 hours. Data represented as mean  $\pm$  SEM.

(C and D) Western blots analysis of WT Tg-FT treated with ML-240 for 4 and 8 hours. Data represented as mean  $\pm$  SEM.

(E) 35S Pulse chase analysis of C1264R Tg-FT with ML-240 treatment.

(F) 35S Pulse chase analysis of WT Tg-FT with ML-240 treatment.

(G-J) Heatmaps showing the relative enrichment for select Tg interactors across proteostasis pathways between untreated and ML-240 treated C1264R Tg.

compared to untreated C1264R. For Hsp70/90 chaperones we found that interactors with key components remain relatively steady throughout the chase period before peaking at the 3 Hr chase timepoint (Figure 4.3H). Conversely, C1264R engagement with Dnajb11 and Dnajc10 tapered off and mimic the WT Tg temporal profile.

Interactions with disulfide processing and prolyl isomerization and hydroxylation components exhibited milder changes with ML-240 compared to untreated samples (Figure 4.3I and 4.3J). Erp29/Pdia9 and Pdia3 engagement remained largely unchanged in the presence of ML-240, while Pdia4 engagement remained relatively low

before peaking at the 3 Hr time point with Pdia6 peaking at the 0 Hr time point and tapering off throughout the chase period (Figure 4.3I). Prolyl isomerization and hydroxylation components showed subtle decreases in relative enrichment, with Nid1 and P4ha1 being unchanged. These milder changes for prolyl isomerization components compared to the more drastic glycan processing and Hsp70/90 chaperone changes highlight that extensive early interactome remodeling during N-glycosylation and Hsp70/90 dependent folding could be a key mechanism for the rescue. On the hand, remodeling with disulfide

processing components during secretion rescue of C1264R involves more discrete changes in engagement, and prolyl isomerization and hydroxylation likely only play a minor role during this secretion rescue.

We monitored UPR activation in the presence of ML-240 and found that 3-hour treatment with ML240 led to a significant increase in Dnajb9 transcript expression in both WT Tg and C2164R Tg FRT cells. Interestingly, ML-240 treatment left Hspa5 and Asns expression unchanged in C1264R Tg cells but led to a significant decrease in WT Tg cells (Figure C.5F). While we observed transcriptional upregulation of Dnajb9 after 3 hours of treatment with ML240, this is likely not enough time for proteomic remodeling. Moreover, ML-240 did not significantly alter cell viability after 3 hours, as measured by propidium iodide staining (Figure C.5G-C.5I). Overall, these results suggest that ML-240 can selectively rescue C1264R Tg secretion, and that this rescue is correlated with unique temporal changes in C1264R PN engagement, but not global remodeling of the ER proteostasis network as a result of UPR activation.

#### **4.6 Mutant Tg is Selectively Enriched with the ER-phagy Receptor TEX264**

Intrigued by the finding that TEX264 silencing increased C1264R Tg secretion without affecting WT Tg, we asked whether TEX264 exhibited differential engagement with Tg constructs. We again used HEK293 Tg-NLuc cells and expressed either a fluorescent GFP control, or C-terminal FLAG-tagged ER-phagy receptors SEC62 and TEX264 to

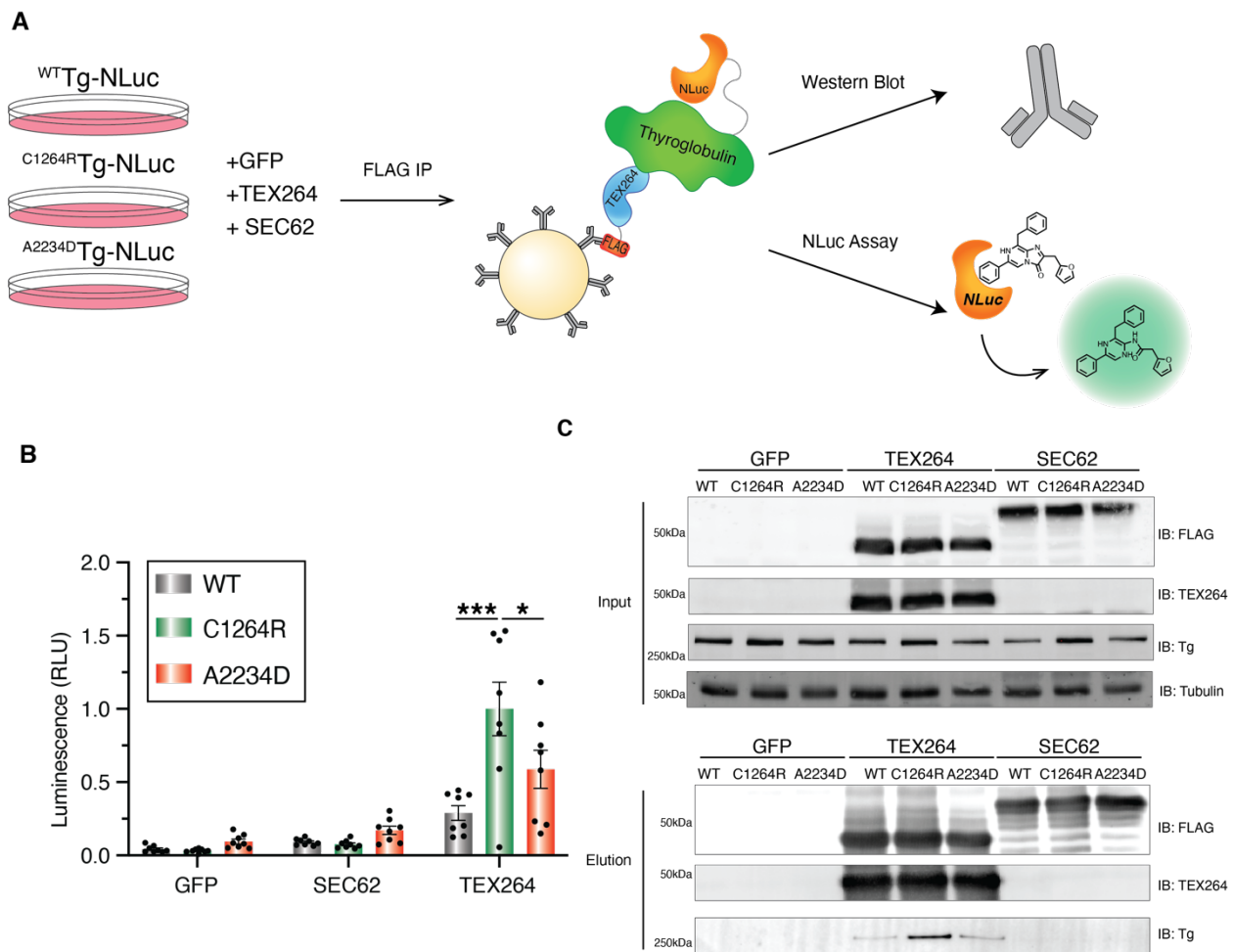


**Figure 4.4: Mutant Tg is Selectively Enriched with the ER-phagy Receptor TEX264**  
 (A) Workflow utilizing western blot and NLuc analysis for identifying TEX264-Tg enrichment.  
 (B) Luminescence data from immunoprecipitation-NLuc analysis. Tg is selectively enriched compared to GFP fluorescent control, or SEC62, with mutant Tg. statistical testing was performed using a one-way ANOVA with post hoc Tukey's multiple testing corrections. \* $p < 0.05$ , \*\* $p < 0.005$ , \*\*\* $p < 0.0005$ .  
 (C) Western blot analysis of immunoprecipitation samples. Tg is selectively enriched compared to GFP fluorescent control, or SEC62, with mutant Tg exhibiting higher enrichment compared to WT.

perform FLAG co-immunoprecipitations (co-IP). We then used the NLuc assay system and western blotting to quantify Tg enrichment in the SEC62 or TEX264 co-IP (Figure 4.4A).

SEC62 silencing did not affect the processing of any Tg constructs in our siRNA screen and therefore should act as negative control (Figure C.2). We found that co-IP of SEC62 did not yield any appreciable enrichment of Tg compared to GFP control when monitored by NLuc assay. Conversely, co-IP of TEX264 resulted in the enrichment of all Tg constructs compared to GFP control when monitored by NLuc assay, with C1264R and A2234D being significantly enriched. C1264R Tg exhibited a roughly 3-fold increase in interactions compared to WT Tg and almost a 2-fold increase compared to A2234D Tg when monitored by NLuc assay (Figure 4.4B). This increase in C1264R enrichment was also observable by western blot analysis (Figure 4.4C).

Together, these data suggest that not only does TEX264 play a role in Tg processing, but CH-associated Tg mutants are selectively targeted to TEX264. Furthermore, these data suggest that ER-phagy should be considered a major degradative pathway in Tg processing, as other studies have mainly focused on Tg degradation through ERAD<sup>46,47</sup>.

## **4.7 Discussion and Conclusions**

Studies into protein-protein interactions often depend on correlative measurements and interpretation when the use of functional screening or investigation is limited or absent. This led us to establish a siRNA screening platform using a NLuc reporter-based assay system to broadly investigate the functional implications of PN protein-protein interactions on Tg processing and PQC. The combination of our novel TRIP approach presented in Chapter 3, coupled with this classical functional screening deconvoluted previously established PQC mechanisms for Tg processing while also providing new paradigms within PQC pathways still being characterized.

With this assay we found the trafficking factor Napa was heavily implicated in WT Tg secretion, as siRNA silencing led to a strong decrease in secretion, coupled with increased retention. Most excitingly, we found that Vcp and Tex264 were implicated in C1264R processing, and siRNA silencing of both factors led to a rescue in C1264R secretion. To expound upon this, we showed that pharmacological Vcp inhibition selectively rescues C1264R secretion compared to WT, and mutant Tg is selectively enriched with Tex264. Both discoveries corroborate our TRIP data from Chapter 3 establishing that Tg mutants undergo differential interactions with degradation pathways compared to WT Tg. Similar phenomena have been observed for the partitioning and differential interactions of other prohormone proteins, such as proinsulin and proopiomelanocortin, and proteasome resistant polymers of alpha1-antitrypsin z. Rtn3 is implicated in this differential engagement and is shown to be selective for these prohormones compared to other ER-phagy receptors<sup>38,39,48</sup>. Furthermore, we used our

TRIP method to monitor the changes in interactions associated with the rescue of C1264R with pharmacological Vcp inhibition. We found that this rescue is correlated with broad temporal changes in interactions across both glycan processing and Hsp70/90 chaperone pathways taking place upstream, while exhibiting more discrete changes with select disulfide/redox processing components and leaving interactions with proly isomerization and hydroxylation components largely unchanged. Mapping these temporal changes with ML-240 treatment and C1264R rescue highlights the capabilities of TRIP to not only resolve protein-protein interactions across disease states but also identify compensatory mechanisms that may take place with drug treatment or other modulating techniques like gene inhibition or activation that can correct disease states.

#### **4.8 Acknowledgements**

M.T.W. was supported by the National Science Foundation – Graduate Research Fellowship Program. This work was also funded by an NIGMS R35 award (1R35GM133552). This content is solely the responsibility of the authors and does not necessarily represent the official views of the National Institutes of Health.

M.T.W. and L.P. designed experiments. M.T.W., and B.T. performed siRNA screening and validation. All authors performed Vcp inhibition experiments. V.G.L performed Tex264 & Tg-NLuc co-immunoprecipitation experiments.

## 4.9 Experimental Methods

### 4.9.1 Plasmid Production and Antibodies

Tg-FLAG in pcDNA3.1+/C-(K)-DYK plasmid was purchased from Genscript (Clone ID OHu20241). The Tg-FLAG gene was then amplified and assembled with an empty pcDNA5/FRT expression vector using a HiFi DNA assembly kit (New England BioLabs, E2621). This plasmid then underwent site-directed mutagenesis to produce pcDNA5-C1264R-Tg-FLAG, and pcDNA5-A2234D-Tg-FLAG plasmids (Table C.1).

An oligonucleotide fragment encoding Nanoluciferase (NLuc) was ordered from Genewiz. To generate pcDNA5/FRT-Tg-NLuc plasmids the Tg gene was amplified from the pcDNA5/FRT-Tg-FLAG plasmid and assembled with the NLuc fragment using a HiFi DNA assembly kit (New England BioLabs). To generate the respective mutant construct plasmids for A2234D and C1264R Tg site directed mutagenesis was performed using a Q5 polymerase (New England BioLabs). All oligonucleotide sequences can be found in Table C.1.

### 4.9.2 Cell Line Engineering

FRT cells were cultured in Ham's F-12, Coon's Modification (F12) media (Sigma, cat. No. F6636) supplemented with 5% fetal bovine serum (FBS), and 1% penicillin (10,000U) / streptomycin (10,000 µg/mL). To generate FRT flp-Tg-FT cells,  $5 \times 10^5$  cells cultured for 1



day were cotransfected with 2.25 µg flp recombinase pOG44 plasmid and 0.25 µg of FT-Tg pcDNA5 plasmid using Lipofectamine 3000. Cells were then cultured in media containing Hygromycin B (100 µg/mL) to select site specific recombinants. Resistant clonal lines were sorted into single cell colonies using flow cytometry and screened for FT-Tg expression (Figure B.1A and B.1B; Table B.2).

HEK293 flp-in cells were cultured in Dulbecco's modified Eagle's medium (DMEM) supplemented with 10 % fetal bovine serum (FBS), 1% L-glutamine (200mM), 1% penicillin (10,000U) / streptomycin (10,000 µg/mL). To generate HEK293 flp-Tg-NLuc cells,  $5 \times 10^5$  cells cultured for 1 day were cotransfected with 2.25 µg flp recombinase pOG44 plasmid and 0.25 µg of NLuc-Tg pcDNA5 plasmid using Lipofectamine 3000. Cells were then cultured in media containing Hygromycin B (100 µg/mL) to select site specific recombinants. Polyclonal lines were screened for Tg-NLuc expression and furimazine substrate turnover (Figure C.1A and C.1B).

#### *4.9.3 Immunoblotting and SDS-PAGE*

Cell lysates were prepared by lysing in RIPA buffer with protease inhibitor cocktail (Roche) and protein concentrations were normalized using a BCA assay (Thermo Scientific). Lysates were then denatured with 1X Laemmli buffer + 100mM DTT and heated at 95°C for 5 minutes before being separated by SDS-PAGE. Samples were transferred onto poly-vinylidene difluoride (PVDF) membranes (Millipore, IPFL00010) for

immunoblotting and blocked using 5% non-fat dry milk dissolved in tris buffered saline with 0.1% Tween-20 (Fisher, BP337-100) (TBS-T). Primary antibodies were incubated either at room temperature for 2 hours, or overnight at 4°C. Membranes were then washed three times with TBS-T and incubated with secondary antibody in 5% non-fat dry milk dissolved in TBS-T either at room temperature for 1 hour or overnight at 4°C. Membranes were washed three times with TBS-T and then imaged using a ChemiDoc MP Imaging System (BioRad). Primary antibodies were acquired from commercial sources and used at the indicated dilutions in immunoblotting buffer (5% bovine serum albumin (BSA) in Tris-buffered saline pH 7.5, 0.1% Tween-20, and 0.1% sodium azide): M2 anti-FLAG (1:1000) and thyroglobulin (1:1000). Secondary antibodies were obtained from commercial sources and used at the indicated dilutions in 5% milk in Tris-buffered saline pH 7.5, 0.1% Tween-20 (TBS-T): Goat anti-mouse Starbright700 (1:10000), Goat anti-rabbit IRDye800 (1:10000).

#### *4.9.4 qRT-PCR*

RNA was prepared from cell pellets using the Quick-RNA miniprep kit (Zymo Research). cDNA was synthesized from 500ng total cellular RNA using random primers (IDT), oligo-dT primers (IDT), and M-MLV reverse transcriptase (Promega). qPCR analysis was performed using iTaq Universal SYBR Green Supermix (Bio-Rad) combined with primers for genes of interest and reactions were run in 96-well plates on a Bio-Rad CFX qPCR instrument. Data analysis was then carried out in CFX Maestro (Bio-Rad).

#### *4.9.5 siRNA Screening Assay*

Proteins previously identified as Tg interactors, and other key proteostasis network components were selected and targeted using an siGENOME SMARTpool siRNA library (Dharmacon) <sup>49</sup>. HEK293 cells stably expressing Tg-NLuc constructs were seeded into 96-well plates at  $2.5 \times 10^4$  cells/well and transfected using DharmaFECT 1 following the DharmaFECT1 protocol (Dharmacon) with a 25nM siRNA concentration. Approximately 36 hours after transfection, cells were washed with PBS and replenished with fresh DMEM media. After 4 hours, Tg-NLuc abundance in the lysate and media were measured using the nano-glo luciferase assay system according to the manufactures protocol (Promega). Four controls were included for the experiments including a non-targeting siRNA control, a siGLO fluorescent control to monitor transfection efficiency, a vehicle control containing transfection reagents but lacking any siRNAs, and a lethal TOX control. Data was median normalized across individual 96-well plates <sup>50</sup>. Data represents two independent experiments for WT-NLuc and A2234D-NLuc, and three independent experiments for C1264R NLuc. Cutoff criteria for hits were set to those genes that increased or decreased Tg-NLuc abundance in lysate or media by  $3\sigma$ .

#### *4.9.6 FRT siRNA Validation Studies*

For siRNA silencing follow-up experiments, Tg FRT cells were seeded into 6-well dishes at  $6.0 \times 10^5$  cells/well transfected using DharmaFECT 1 following the DharmaFECT protocol (Dharmacon) with 25nM siRNA concentration. Approximately 36 hours after transfection, cells were washed with PBS and harvested for qRT-PCR or immunoblotting analysis. siRNA target transcript levels were normalized to GAPDH as a loading control. To monitor the effects of siRNA KD on Tg secretion in FRT cells, approximately 36 hours after transfection cells were washed with PBS and replenished with fresh DMEM media. After 4 hours in the case of WT Tg, and 8 hours in the case of C1264R or A2234D Tg cells and media samples were harvested. Cells were lysed with 1mL of RIPA with protease inhibitor cocktail (Roche), and lysate and media samples were subjected to immunoprecipitation with G1 Anti-DYKDDDDK affinity resin overnight at 4°C while rocking. After three washes with RIPA buffer, protein samples were eluted with 3× Laemmli buffer with 100 mM DTT heating at 95°C for 5 min. Immunoblot quantification was performed using Image Lab Software (BioRad)

#### *4.9.7 <sup>35</sup>S Pulse Chase Assay*

Confluent 6-well dishes of FRT cells (approximately  $1 \times 10^6$ /well) were metabolically labeled in DMEM depleted of methionine and cysteine and supplemented with EasyTag <sup>35</sup>S Protein Labeling Mix (Perkin Elmer, NEG772007MC), glutamine, penicillin/streptomycin, and 10% FBS at 37° C for 30 minutes. Afterward, cells were washed twice with F12 media containing 10X methionine and cysteine, followed by a burn

off period of 10 minutes in normal F12 media. Cells were then chased for the respective time periods with normal F12 media, lysed with 500uL of RIPA buffer with protease inhibitor cocktail (Roche) and 10 mM DTT. Cell lysates were diluted with 500uL of RIPA buffer with protease inhibitor cocktail (Roche) and subjected to immunoprecipitation with G1 anti-DYKDDDDK affinity resin overnight at 4° C. After three washes with RIPA buffer, protein samples were eluted with 3x Laemmli buffer with 100 mM DTT heating at 95°C for 5 min. Eluted samples were then separated by SDS-PAGE, and gels were dried and exposed on a storage phosphor screen. Radioactive band intensity was then measured using a Typhoon Trio Imager (GE Healthcare) and quantified by densitometry in Image Lab (BioRad).

#### *4.9.8 VCP Pharmacological Inhibition Studies*

For follow-up experiment with VCP inhibitors, confluent 6-well dishes of C1264R Tg FRT cells were washed with PBS and had fresh F12 media added supplemented with ML-240 (10µM), CB-5083 (5µM), NMS-873 (10µM), or vehicle (0.1% DMSO) and incubated for 8 hours. For WT cells, confluent 6-well dishes were similarly used, washed with PBS and had fresh F12 media added supplemented with ML-240 (10µM) or vehicle (0.1% DMSO) and incubated for 4 or 8 hours. Cells were lysed with 1mL of RIPA with protease inhibitor cocktail (Roche), and lysate and media samples were subjected to immunoprecipitation with G1 Anti-DYKDDDDK affinity resin overnight at 4°C while rocking. After three washes with RIPA buffer, protein samples were eluted with 3x Laemmli buffer with 100 mM DTT

heating at 95°C for 5 min. Immunoblot quantification was performed using Image Lab Software (BioRad).

For TRIP analysis coupled with ML-240 treatment, C1264R Tg FRT cells were processed as described above with ML-240 (10 $\mu$ M) supplemented in Hpg-pulse media and throughout the chase period.

Viability with ML-240 was monitored using propidium iodide staining. Briefly, cells were treated with either ML-240 (10 $\mu$ M) or vehicle (0.1% DMSO) for 4 hours before being harvested and stained with propidium iodide (1 $\mu$ g/mL) at room temperature for 15 minutes in the dark. Cell permeabilized with 0.2% Triton were used as a positive staining control. Data analysis was then carried out in FlowJo (BD Biosciences).

#### *4.9.9 TEX264 & Tg-NLuc Co-Immunoprecipitation Studies*

HEK293 flp-Tg-NLuc cells were cultured at 1.0x10<sup>5</sup> cells/well in 12-well tissue culture dishes for 1 day and transfected with either a fluorescent control, c-terminal FLAG-tag TEX264, or c-terminal FLAG-tag SEC62 using a calcium phosphate method. Confluent plates were harvested by lysing with 300 $\mu$ L of TNI buffer (50mM Tris pH 7.5, 150 mM NaCl, 0.5% IGEPAL CA-630 (Sigma-Aldrich)) and protease inhibitor (Roche). Lysates were sonicated for 10 minutes at room temperature and normalized using BCA Assay (Thermo Scientific). Cell lysates were then precleared on 4B sepharose beads (Sigma,

4B200) at 4°C for 1 hour while rocking, then immunoprecipitated with G1 Anti-DYKDDDDK affinity resin overnight at 4°C while rocking. Resin was washed four times with TNI buffer and resuspended in 250 µL of TNI buffer. 50 µL aliquots were taken and measured using the nano-glo luciferase assay system according to the manufactures protocol (Promega). For differential enrichment, statistical analysis was performed in Prism 9 (GraphPad) using a one-way ANOVA with post hoc Tukey's multiple testing corrections.

For western blot analysis HEK293 flp-Tg-NLuc  $1.0 \times 10^6$  cells/dish in 10 cm tissue culture dishes for 1 day and transfected with either a fluorescent control, TEX264, or SEC62 using a calcium phosphate method. Cells were collected and lysed using 300 µL of TNI buffer with protease inhibitor (Roche) sonicated at room temperature for 10 minutes. Lysates were normalized, precleared, and immunoprecipitated as described above. Proteins were eluted using 6X Laemmli buffer + 100mM DTT, separated by SDS-PAGE and transferred to PVDF membrane (Millipore) for immunoblotting.

#### *4.9.10 Mass Spectrometry Interactomics and TMT Quantification*

Tg interactors identified and characterized in Chapter 3 were used for TRIP analysis. For pathway enrichment analysis of identified proteins, EnrichR was used and GO Cellular Component and Molecular Function 2018 terms were used to differentiate secretory pathway associated proteins from background<sup>52</sup>. For time resolved analysis, data were

processed in R manually. Briefly, TMT abundances across chase samples were normalized to Tg TMT abundance as described previously and compared to (-) Hpg samples for enrichment analysis<sup>49</sup>. Analysis scripts are available as described in the Data and Code Availability section.

#### 4.9.11 Data and Code Availability

The dataset used for siRNA screening characterization showing Tg-NLuc luminescence quantification are included in File C.1. The dataset used for the mass spectrometry interactome characterization experiments with ML-240 treatment showing protein identification and quantification are included in File C.2. Mass spectrometry spectrum and result files are available via ProteomeXchange under identifier PXD035681. Code used for data analysis and generation of figures is available at [github.com/wrighmt1/2022\\_TRIP](https://github.com/wrighmt1/2022_TRIP).

#### 4.10 References

1. Wright, M. T. & Plate, L. Revealing functional insights into ER proteostasis through proteomics and interactomics. *Experimental Cell Research* **399**, (2021).
2. Bludau, I. & Aebersold, R. Proteomic and interactomic insights into the molecular basis of cell functional diversity. *Nature Reviews Molecular Cell Biology* **21**, 327–340 (2020).
3. Karagöz, G. E., Acosta-Alvear, D. & Walter, P. The Unfolded Protein Response: Detecting and Responding to Fluctuations in the Protein-Folding Capacity of the Endoplasmic Reticulum. *Cold Spring Harb Perspect Biol* a033886 (2019).
4. Braakman, I. & Hebert, D. N. Protein Folding in the Endoplasmic Reticulum. *Cold Spring Harbor Perspectives in Biology* **5**, a013201–a013201 (2013).



5. Pankow, S. *et al.*  $\Delta$ F508 CFTR interactome remodelling promotes rescue of cystic fibrosis. *Nature* **528**, 510–516 (2015).
6. Pankow, S., Bamberger, C. & Yates, J. R. A posttranslational modification code for CFTR maturation is altered in cystic fibrosis. *Science Signaling* (2019).
7. Hafirassou, M. L. *et al.* A Global Interactome Map of the Dengue Virus NS1 Identifies Virus Restriction and Dependency Host Factors. *Cell Reports* **21**, 3900–3913 (2017).
8. Guisbert, E., Czyz, D. M., Richter, K., McMullen, P. D. & Morimoto, R. I. Identification of a Tissue-Selective Heat Shock Response Regulatory Network. *PLoS Genetics* **9**, (2013).
9. Silva, M. C. *et al.* A genetic screening strategy identifies novel regulators of the proteostasis network. *PLoS Genetics* **7**, (2011).
10. Liang, J. R. *et al.* A Genome-wide ER-phagy Screen Highlights Key Roles of Mitochondrial Metabolism and ER-Resident UFMylation. *Cell* **180**, 1160-1177.e20 (2020).
11. Christianson, J. C. *et al.* Defining human ERAD networks through an integrative mapping strategy. *Nature Cell Biology* **14**, 93–105 (2012).
12. Sun, Z., Guerriero, C. J. & Brodsky, J. L. Substrate ubiquitination retains misfolded membrane proteins in the endoplasmic reticulum for degradation. *Cell Reports* **36**, (2021).
13. Liu, D. *et al.* ER-phagy requires the assembly of actin at sites of contact between the cortical ER and endocytic pits. *Proc Natl Acad Sci U S A* **119**, (2022).
14. Chen, S. *et al.* Vps13 is required for the packaging of the ER into autophagosomes during ER-phagy. *Proc Natl Acad Sci U S A* **117**, 18530–18539 (2020).
15. Chino, H., Hatta, T., Natsume, T. & Mizushima, N. Intrinsically Disordered Protein TEX264 Mediates ER-phagy. *Molecular Cell* **74**, 909-921.e6 (2019).
16. Shurtleff, M. J. *et al.* The ER membrane protein complex interacts cotranslationally to enable biogenesis of multipass membrane proteins. *Elife* **7**, (2018).
17. Marinko, J. T. *et al.* Glycosylation limits forward trafficking of the tetraspan membrane protein PMP22. *Journal of Biological Chemistry* **296**, (2021).
18. Brehme, M. *et al.* A Chaperome Subnetwork Safeguards Proteostasis in Aging and Neurodegenerative Disease. *Cell Reports* **9**, 1135–1150 (2014).
19. England, C. G., Ehlerding, E. B. & Cai, W. NanoLuc: A Small Luciferase Is Brightening Up the Field of Bioluminescence. *Bioconjugate Chemistry* **27**, 1175–1187 (2016).
20. Song, H., Orr, A., Duan, M., Merz, A. J. & Wickner, W. Sec17/Sec18 act twice, enhancing membrane fusion and then disassembling cis-SNARE complexes. *Elife* **6**, (2017).
21. Zhao, C., Slevin, J. T. & Whiteheart, S. W. Cellular functions of NSF: Not just SNAPs and SNAREs. *FEBS Letters* **581**, 2140–2149 (2007).
22. Kos, J., Jevnikar, Z. & Obermajer, N. The role of cathepsin X in cell signaling. *Cell Adhesion & Migration* **3**, 164–166 (2009).

23. Bhutani, N., Piccirillo, R., Hourez, R., Venkatraman, P. & Goldberg, A. L. Cathepsins L and Z Are Critical in Degrading Polyglutamine-containing Proteins within Lysosomes. *Journal of Biological Chemistry* **287**, 17471–17482 (2012).
24. Naz, H. *et al.* Human  $\beta$ -Glucuronidase: Structure, Function, and Application in Enzyme Replacement Therapy. <https://home.liebertpub.com/rej> **16**, 352–363 (2013).
25. Ryuzono, S. *et al.* Lysosomal localization of Japanese medaka (*Oryzias latipes*) Neu1 sialidase and its highly conserved enzymatic profiles with human. *Gene* **575**, 513–523 (2016).
26. Pshezhetsky, A. v. & Hinek, A. Where catabolism meets signalling: neuraminidase 1 as a modulator of cell receptors. *Glycoconjugate Journal* **28**, 441–452 (2011).
27. Citterio, C. E., Targovnik, H. M. & Arvan, P. The role of thyroglobulin in thyroid hormonogenesis. *Nature Reviews Endocrinology* **15**, 323–338 (2019).
28. McGilvray, P. T. *et al.* An ER translocon for multi-pass membrane protein biogenesis. *Elife* **9**, 1–43 (2020).
29. An, H. *et al.* TEX264 Is an Endoplasmic Reticulum-Resident ATG8-Interacting Protein Critical for ER Remodeling during Nutrient Stress. *Molecular Cell* **74**, 891–908.e10 (2019).
30. Cui, Y. *et al.* A COPII subunit acts with an autophagy receptor to target endoplasmic reticulum for degradation. *Science* (1979) **365**, 53–60 (2019).
31. Vranka, J. A., Sakai, L. Y. & Bächinger, H. P. Prolyl 3-Hydroxylase 1, Enzyme Characterization and Identification of a Novel Family of Enzymes. *Journal of Biological Chemistry* **279**, 23615–23621 (2004).
32. Hill, S. M. *et al.* VCP/p97 regulates Beclin-1-dependent autophagy initiation. *Nature Chemical Biology* **17**, 448–455 (2021).
33. Christianson, J. C., Shaler, T. A., Tyler, R. E. & Kopito, R. R. OS-9 and GRP94 deliver mutant  $\alpha$ 1-antitrypsin to the Hrd1–SEL1L ubiquitin ligase complex for ERAD. *Nature Cell Biology* **10**, 272–282 (2008).
34. Needham, P. G., Guerriero, C. J. & Brodsky, J. L. Chaperoning Endoplasmic Reticulum-Associated Degradation (ERAD) and Protein Conformational Diseases. *Cold Spring Harb Perspect Biol* a033928 (2019).
35. Okuda-Shimizu, Y. & Hendershot, L. M. Characterization of an ERAD pathway for nonglycosylated BiP substrates, which require Herp. *Mol Cell* **28**, 544–554 (2007).
36. Fielden, J., Popović, M. & Ramadan, K. TEX264 at the intersection of autophagy and DNA repair. *Autophagy* **18**, 40 (2022).
37. Grumati, P. *et al.* Full length RTN3 regulates turnover of tubular endoplasmic reticulum via selective autophagy. *Elife* **6**, e25555 (2017).
38. Chen, Y. J. *et al.* PGRMC1 acts as a size-selective cargo receptor to drive ER-phagic clearance of mutant prohormones. *Nature Communications* **12**, (2021).
39. Cunningham, C. N. *et al.* Cells Deploy a Two-Pronged Strategy to Rectify Misfolded Proinsulin Aggregates. *Molecular Cell* **75**, 442–456.e4 (2019).
40. Vij, N., Fang, S. & Zeitlin, P. L. Selective inhibition of endoplasmic reticulum-associated degradation rescues DeltaF508-cystic fibrosis transmembrane

- regulator and suppresses interleukin-8 levels: therapeutic implications. *J Biol Chem* **281**, 17369–17378 (2006).
41. Morishita, Y. *et al.* Thyrocyte cell survival and adaptation to chronic endoplasmic reticulum stress due to misfolded thyroglobulin. *Journal of Biological Chemistry* **295**, 6876–6887 (2020).
  42. Gwon, Y. *et al.* Ubiquitination of G3BP1 mediates stress granule disassembly in a context-specific manner. *Science (1979)* **372**, (2021).
  43. Chou, T. F., Li, K., Frankowski, K. J., Schoenen, F. J. & Deshaies, R. J. Structure–Activity Relationship Study Reveals ML240 and ML241 as Potent and Selective Inhibitors of p97 ATPase. *ChemMedChem* **8**, 297–312 (2013).
  44. Chou, T. F. *et al.* Specific Inhibition of p97/VCP ATPase and Kinetic Analysis Demonstrate Interaction between D1 and D2 ATPase Domains. *Journal of Molecular Biology* **426**, 2886–2899 (2014).
  45. Zhou, H. J. *et al.* Discovery of a First-in-Class, Potent, Selective, and Orally Bioavailable Inhibitor of the p97 AAA ATPase (CB-5083). *Journal of Medicinal Chemistry* **58**, 9480–9497 (2015).
  46. Tokunaga, F., Brostrom, C., Koide, T. & Arvan, P. Endoplasmic reticulum (ER)-associated degradation of misfolded N-linked glycoproteins is suppressed upon inhibition of ER mannosidase I. *Journal of Biological Chemistry* **275**, 40757–40764 (2000).
  47. Menon, S. *et al.* Oxidoreductase Interactions Include a Role for ERp72 Engagement with Mutant Thyroglobulin from the rdw/rdw Rat Dwarf. *Journal of Biological Chemistry* **282**, 6183–6191 (2007).
  48. Fregno, I. *et al.* ER-to-lysosome-associated degradation of proteasome-resistant ATZ polymers occurs via receptor-mediated vesicular transport. *The EMBO Journal* **37**, (2018).
  49. Wright, M. T., Kouba, L. & Plate, L. Thyroglobulin Interactome Profiling Defines Altered Proteostasis Topology Associated With Thyroid Dysmorphogenesis. *Molecular & Cellular Proteomics* **20**, 100008 (2021).
  50. Chung, N. *et al.* Median Absolute Deviation to Improve Hit Selection for Genome-Scale RNAi Screens. *Journal of Biomolecular Screening* **13**, 149–158 (2008).
  51. Zhang, X. *et al.* Proteome-wide identification of ubiquitin interactions using UblA-MS. *Nature Protocols* **13**:3 **13**, 530–550 (2018).
  52. Chen, E. Y. *et al.* Enrichr: interactive and collaborative HTML5 gene list enrichment analysis tool. *BMC Bioinformatics* **14**, 128 (2013).

### **Conclusions and Future Directions**

Genetic variations in the thyroglobulin (Tg) gene have been extensively studied, with 167 documented mutations that lead to congenital hypothyroidism (CH). Furthermore, the expression, folding, processing, and degradation of several of these mutations has been further characterized for years<sup>1-4</sup>. Although, this area of research has become stagnant in recent years. Previous work often relied on characterizing the implications of a single protein at a time, compared to the systems biology level approach presented in Chapters 2-4. Chapters 2-4 have answered several questions into the pathology of Tg misfolding and CH, while also bringing about new questions within CH-associated Tg mutations and protein quality control (PQC) overall.

In Chapter 2, we performed an in-depth characterization of the protein-protein interactions (interactome) associated with Tg folding, processing, and degradation. This was the first work to extensively characterize the Tg interactome and broadly assess changes in proteostasis network (PN) interactions associated with mutant Tg dyshormonogenesis. This provided a dataset that revealed several areas worth further exploration into the processing of Tg. For example, investigations into the role in which post-translational modifications play in Tg folding, processing, and secretion would be fruitful. We revealed that one CH-associated mutation, A2234D, requires expression of both

oligosaccharyltransferase (OST) catalytic subunits involved in N-glycosylation for efficient degradation of Tg. Tg undergoes extensive post translation modifications (PTMs) in addition to N-glycosylation, including disulfide bond formation, phosphorylation, and sulfation<sup>5</sup>. While it is clear that PTMs play a pivotal role in the processing of thousands of proteins through the secretory pathway, in the case of Tg it remains unclear what the implications are for individual PTMs throughout the Tg structure<sup>6-8</sup>. Investigating this through the systematic mapping of the “PTM code” using MS, as it has been described elsewhere, in the presence of PQC pathway inhibitors or mutated sites of PTM modification could add details necessary to further understand the paradigm of Tg folding, processing, and secretory PQC. Tg peptides that have been modified through phosphorylation, different glycosylation states, or different cysteine redox states can be enriched and analyzed via AP-MS. Furthermore, just as clients undergo PTMs during folding and processing, PN component’s activity and localization are similarly controlled through PTMs. Yet the implications for many of these PTMs on PN components is still poorly characterized<sup>9-12</sup>.

With the completion of the study in Chapter 2, one of the most pressing areas of further investigation was understanding the timing of PN interactions for Tg folding and processing. This ultimately led to the work presented in Chapter 3. This first in class method, time-resolved interactome profiling (TRIP), allows for the temporal characterization of de novo protein-protein interactions at an organelle wide level. This allowed us to characterize the Tg interactome in native thyroid tissue using Fischer rat

thyroid (FRT) cells, identifying and temporally characterizing several new interactors compared to the data found in Chapter 2. Furthermore, this allowed us to identify the altered timing associated with mutant Tg processing through the secretory pathway, providing further detail into CH dyshormonogenesis. As we hope to see the continued utilization of TRIP across other proteomic studies, there are already areas for further improvement and new directions for this methodology. The TRIP methodology requires extensive sample handling, which inherently increases the variability of the proteomic measurements. Implementing the TRIP workflow with automated liquid handling robotics could greatly improve this area of variability and further strengthen the utilization of TRIP<sup>13</sup>. Because of the extensive sample handling involved in TRIP, this directly affects the temporal resolution that can be achieved. Amine-reactive in-situ crosslinking, and quenching are two steps that add more time and thus decrease the resolving power of the method. Faster crosslinking with ultraviolet (UV)-activated crosslinkers could improve this step. The two-stage enrichment strategy for TRIP inherently limits the amount of protein(s) that can be enriched, and further contributes to variability in proteomic measurements. Using a more direct method for protein labeling, and subsequent enrichment could alleviate this two-stage enrichment requirement. Methodologies capable of this, such as Halo-tags or stabilizing degradation-domain technology are already being explored within the Plate lab for such applications<sup>14-17</sup>. Moreover, if these more-direct protein labeling technologies can be coupled with UV activated crosslinking this would further improve the temporal resolution of these methodologies. Photocaged unnatural amino acids have been used to selectively “turn on” engineered proteins at

specific loci or times within cells, similar approaches may be fruitful with this time-resolved methodology<sup>18,19</sup>. Finally, Chapter 3 utilizes this TRIP methodology in a limited manner, utilizing a luminal, slow-folding, secreted protein-of-interest, Tg. Beyond the work presented here in this dissertation, I have had the pleasure of collaborating on other projects investigating PQC mechanisms and associated pathologies. These include the characterization of interactions involved in the folding and processing of peripheral myelin protein 22 (PMP22) and the pathological implications of mutant PMP22 in Charcot-Marie-Tooth disease, PDIA3 functional implications in amyotrophic lateral sclerosis (ALS), and the pathological implications of an enzymatically deficient PDIA3 mutant in intellectual disability<sup>20-22</sup>. Utilizing TRIP to further explore the temporal dynamics of protein-protein interactions implicated in protein misfolding disease states such as these would reveal fruitful insights and aid in the further utilization of this methodology across the field of PQC.

To understand the mechanisms associated with cellular processes, it is paramount to comprehend the functional implications genes or other components have within these processes. This is especially the case in the context of PQC mechanisms, as they often contain several layers of redundancy and crosstalk. In Chapter 4, we presented a nanoluciferase (NLuc)-based screening platform that allowed us to investigate the functional implications of Tg interactors and other PN components on Tg processing and secretion<sup>23</sup>. The largest discovery from this study was differential mechanisms associated with mutant Tg degradation compared to WT involving Vcp and Tex264 in FRT cells.

Wherein siRNA silencing of Vcp or Tex264 was found to rescue C1264R secretion under steady-state, but was difficult to observe via <sup>35</sup>S pulse-chase assay. The discrepancy between our steady-state and <sup>35</sup>S pulse-chase data with Vcp and Tex264 silencing is enigmatic. This led us to seek further validation with pharmacological Vcp inhibition and Tex264 co-immunoprecipitation experiments, and highlights areas worth further investigation. As we discovered that pharmacological Vcp inhibition can rescue C1264R secretion yet is detrimental for WT processing it is unclear what role Vcp plays in these cases. The crosstalk between proteasomal and lysosomal degradation, and the implications of Vcp in both emphasizes this point. Furthermore, it may be the case that the involvement of Vcp in other areas outside of protein degradation may be at play<sup>24-26</sup>. Similarly, Tex264 function in both protein degradation and DNA damage repair further complicates these siRNA based investigations<sup>27</sup>. Next, as we showed A2234D and C1264R Tg are preferentially enriched with Tex264 compared to WT. The luminal domain of Tex264 is likely too small to sequester client proteins directly<sup>28,29</sup>. Yet, it is unclear what other accessory proteins may be necessary for the recognition of Tex264 clients. Differential interactomics studies utilizing affinity purification – mass spectrometry (AP-MS) with co-immunoprecipitation of Tex264 could help identify these accessory proteins that are necessary for Tex264-dependent engagement and degradation. It is interesting to note that RTN3 siRNA silencing in our initial screen with HEK293 cells rescued C1264R secretion, yet in FRT cells decreased C1264R secretion. To speculate, this may highlight the influence that different Rtn3 isoforms have on ER dynamics as only the long isoform is involved in ER-phagy<sup>30</sup>. Nonetheless, this provides another area worth further



investigation. Beyond the investigations into PQC mechanisms this NLuc-based screening platform could similarly be used to discover molecules that may modulate Tg processing and rescue secretion, with the potential to serve as therapeutic interventions beyond the traditional hormone replacement therapies.

To conclude, the body of work put forth within this dissertation has broad implications across several fields. It has served to advance our fundamental understanding around CH pathology and thyroid dysmorphogenesis. Implications on PQC found from these studies will likely find applicability and relevancy in other protein misfolding disease states. Outside of fundamental biology, the development of our TRIP workflow has provided an adaptable method that was desperately needed within the mass spectrometry field and should find broad applicability across several proteomic investigations.

## References

1. Citterio, C. E., Rivolta, C. M. & Targovnik, H. M. Structure and genetic variants of thyroglobulin: Pathophysiological implications. *Molecular and Cellular Endocrinology* **528**, (2021).
2. Targovnik, H. M., Citterio, C. E. & Rivolta, C. M. Thyroglobulin gene mutations in congenital hypothyroidism. *Hormone Research in Paediatrics* **75**, 311–321 (2011).
3. Kim, P. S., Bole, D. & Arvan, P. Transient aggregation of nascent thyroglobulin in the endoplasmic reticulum: relationship to the molecular chaperone, BiP. *The Journal of Cell Biology* **118**, 541–549 (1992).
4. Kim, P. S. & Arvan, P. Calnexin and BiP act as sequential molecular chaperones during thyroglobulin folding in the endoplasmic reticulum. *J Cell Biol* **128**, 29–38 (1995).

5. Citterio, C. E., Targovnik, H. M. & Arvan, P. The role of thyroglobulin in thyroid hormonogenesis. *Nature Reviews Endocrinology* **15**, 323–338 (2019).
6. Ronin, C., Fenouillet, E., Hovsepian, S., Fayet, G. & Fournet, B. Regulation of thyroglobulin glycosylation. A comparative study of the thyroglobulins from porcine thyroid glands and follicles in serum-free culture. *Journal of Biological Chemistry* **261**, 7287–7293 (1986).
7. Ushioda, R. & Nagata, K. Redox-Mediated Regulatory Mechanisms of Endoplasmic Reticulum Homeostasis. *Cold Spring Harb Perspect Biol* **11**, a033910 (2018).
8. Braakman, I. & Hebert, D. N. Protein Folding in the Endoplasmic Reticulum. *Cold Spring Harbor Perspectives in Biology* **5**, a013201–a013201 (2013).
9. Pankow, S., Bamberger, C. & Yates, J. R. A posttranslational modification code for CFTR maturation is altered in cystic fibrosis. *Science Signaling* (2019).
10. Pankow, S. *et al.*  $\Delta$ F508 CFTR interactome remodelling promotes rescue of cystic fibrosis. *Nature* **528**, 510–516 (2015).
11. Cha-Molstad, H. *et al.* Amino-terminal arginylation targets endoplasmic reticulum chaperone BiP for autophagy through p62 binding. *Nature Cell Biology* **17**, 917–929 (2015).
12. Yu, J. *et al.* Phosphorylation switches protein disulfide isomerase activity to maintain proteostasis and attenuate ER stress. *The EMBO Journal* e103841 (2020).
13. Müller, T. *et al.* Automated sample preparation with SP3 for low-input clinical proteomics. *Molecular Systems Biology* **16**, e9111 (2020).
14. Miller, L. W., Cai, Y., Sheetz, M. P. & Cornish, V. W. In vivo protein labeling with trimethoprim conjugates: a flexible chemical tag. *Nature Methods* **2005 2:4 2**, 255–257 (2005).
15. Murrey, H. E. *et al.* Systematic Evaluation of Bioorthogonal Reactions in Live Cells with Clickable HaloTag Ligands: Implications for Intracellular Imaging. *J Am Chem Soc* **137**, 11461–11475 (2015).
16. Lang, K. & Chin, J. W. Cellular Incorporation of Unnatural Amino Acids and Bioorthogonal Labeling of Proteins. *Chemical Reviews* **114**, 4764–4806 (2014).
17. Elliott, T. S., Bianco, A., Townsley, F. M., Fried, S. D. & Chin, J. W. Tagging and Enriching Proteins Enables Cell-Specific Proteomics. *Cell Chemical Biology* **23**, 805–815 (2016).
18. Hemphill, J., Chou, C., Chin, J. W. & Deiters, A. Genetically encoded light-activated transcription for spatiotemporal control of gene expression and gene silencing in mammalian cells. *J Am Chem Soc* **135**, 13433–13439 (2013).
19. Lemke, E. A., Summerer, D., Geierstanger, B. H., Brittain, S. M. & Schultz, P. G. Control of protein phosphorylation with a genetically encoded photocaged amino acid. *Nature Chemical Biology* **2007 3:12 3**, 769–772 (2007).
20. Marinko, J. T. *et al.* Glycosylation limits forward trafficking of the tetraspan membrane protein PMP22. *Journal of Biological Chemistry* **296**, (2021).
21. Rozas, P. *et al.* Protein disulfide isomerase ERp57 protects early muscle denervation in experimental ALS. *Acta Neuropathologica Communications* **9**, (2021).

22. Medinas, D. B. *et al.* Mutation in protein disulfide isomerase A3 causes neurodevelopmental defects by disturbing endoplasmic reticulum proteostasis. *The EMBO Journal* **41**, (2022).
23. England, C. G., Ehlerding, E. B. & Cai, W. NanoLuc: A Small Luciferase Is Brightening Up the Field of Bioluminescence. *Bioconjugate Chemistry* **27**, 1175–1187 (2016).
24. Pohl, C. & Dikic, I. Cellular quality control by the ubiquitin-proteasome system and autophagy. *Science (1979)* **366**, 818–822 (2019).
25. Twomey, E. C. *et al.* Substrate processing by the Cdc48 ATPase complex is initiated by ubiquitin unfolding. *Science (1979)* **365**, (2019).
26. DeLaBarre, B. & Brunger, A. T. Complete structure of p97/valosin-containing protein reveals communication between nucleotide domains. *Nature Structural & Molecular Biology* **2003 10:10 10**, 856–863 (2003).
27. Fielden, J., Popović, M. & Ramadan, K. TEX264 at the intersection of autophagy and DNA repair. *Autophagy* **18**, 40 (2022).
28. Chino, H., Hatta, T., Natsume, T. & Mizushima, N. Intrinsically Disordered Protein TEX264 Mediates ER-phagy. *Molecular Cell* **74**, 909-921.e6 (2019).
29. An, H. *et al.* TEX264 Is an Endoplasmic Reticulum-Resident ATG8-Interacting Protein Critical for ER Remodeling during Nutrient Stress. *Molecular Cell* **74**, 891-908.e10 (2019).
30. Grumati, P. *et al.* Full length RTN3 regulates turnover of tubular endoplasmic reticulum via selective autophagy. *Elife* **6**, e25555 (2017).

## Appendix

Appendix A

Supplementary Materials for Chapter 2

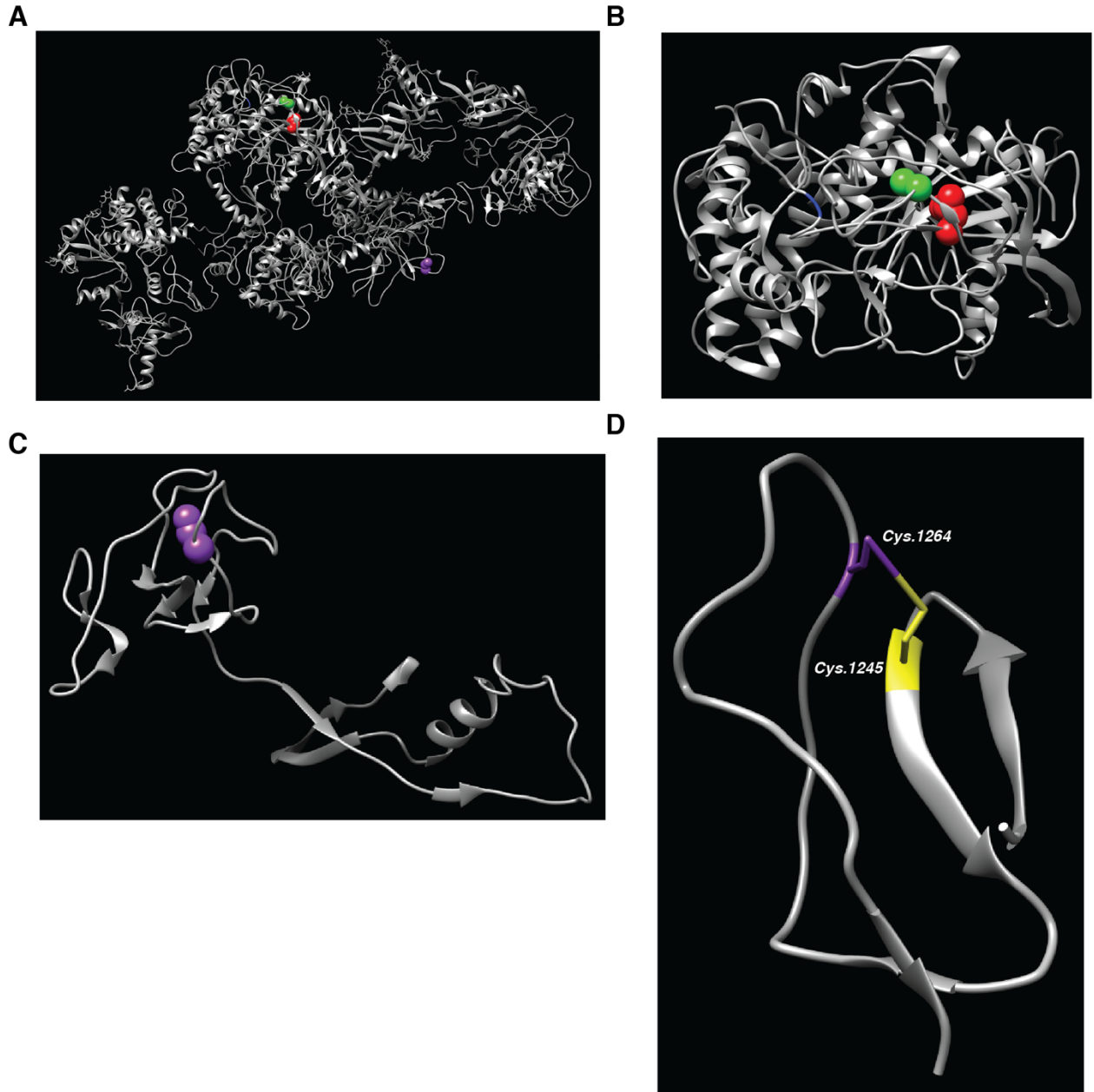


**Figure A.1. Structure of thyroglobulin and localization of missense mutations**

(A) Cryo-electron microscopy structure of Tg monomer (PDB ID: 6SCJ). Missense mutations are annotated: G2341R (Blue), L2284P (Red), A2234D (Green), and C1264R (Purple).

(B) Tg Cholinesterase (ChEL)/CTD domain. ChEL/CTD mutations share close proximity with one another.

(C) Tg Hinge/Flap region with C1264R mutation.

(D) Tg disulfide bridge formed by C1264 and C1245.

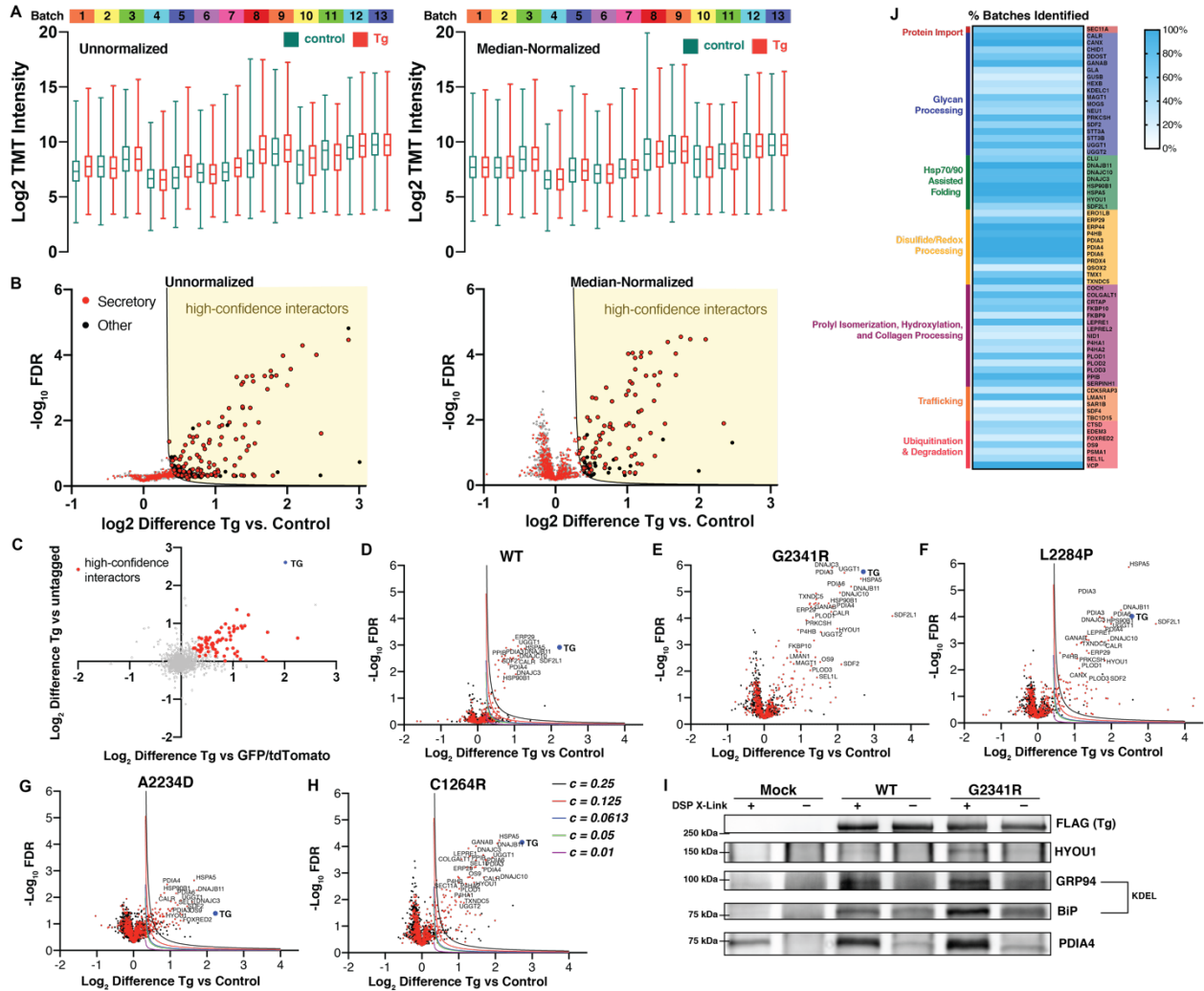


## Figure A.2. Processing of quantitative mass spectrometry data to filter high confidence interactors

(A) Distribution of TMT reporter ion intensities of all quantified proteins for the Tg (red) and control channels (green). Raw data unnormalized and transformed data based on median-normalization is shown.

(B) Volcano plot for comparison of protein abundances in Tg vs control channels to identify high-confidence interactors using unnormalized TMT intensities or median-normalized TMT intensities.

(C) Correlation plot comparing enrichment of Tg and confident interactors between untagged WT Tg or GFP/tdTomato controls.

(D-H) Volcano plots displaying the optimization of cut-off parameters for identification of high-confidence interactors for each Tg variant (WT, G2341R, L2284P, A2234D, C1264R).

(I) Immunoblot from co-immunoprecipitations with and without DSP crosslinking.

(J) Heatmap indicating the frequency of mass spectrometry batches in which confident Tg interactors were identified.

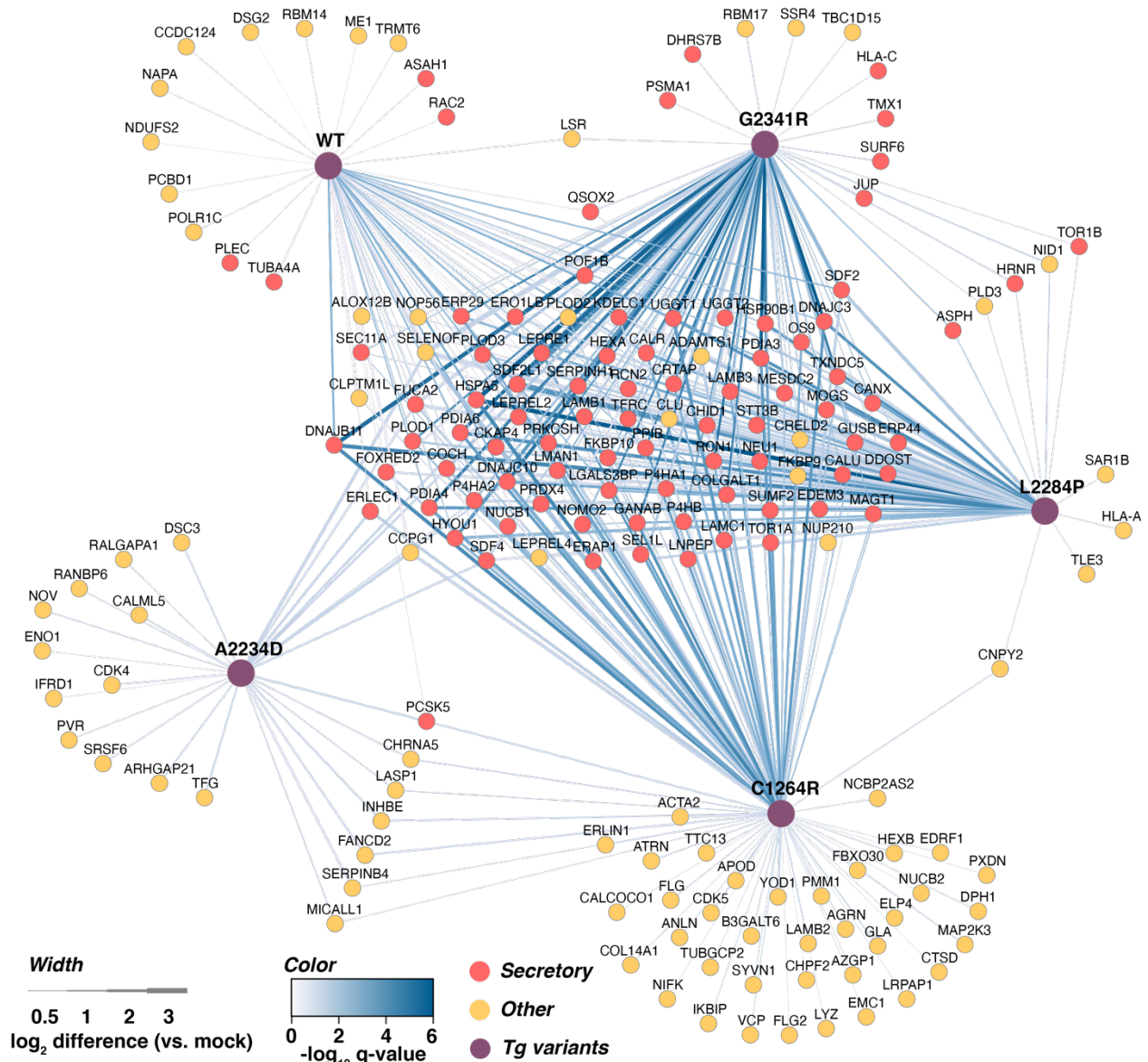


**Figure A.3. Network plot of Tg interactions with WT and mutant variants.**



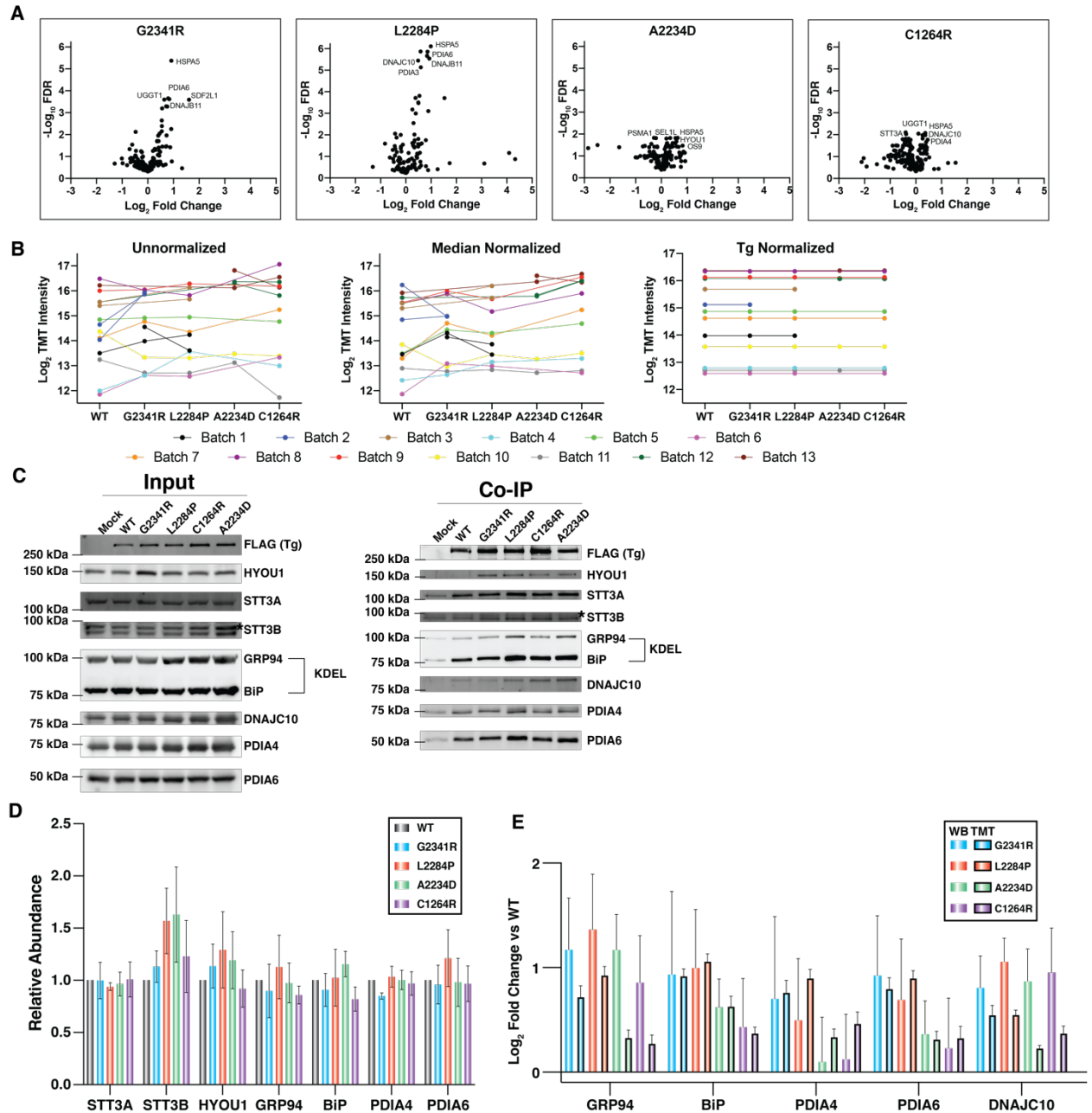


**Figure A.4. Comparison of interaction changes between mutant Tg variants and WT Tg**

(A) Volcano plot showing the interaction changes of interactors between individual mutant Tg variants and WT.

(B) TMT intensities of Tg variants across the individuals mass spectrometry batches.

(C) Representative immunoblots from co-immunoprecipitations confirming select interaction changes between Tg and proteostasis factors.

(D) Quantification of the inputs from the Co-IP experiments from (C).

(E) Quantification of the Co-IP experiments from (C).

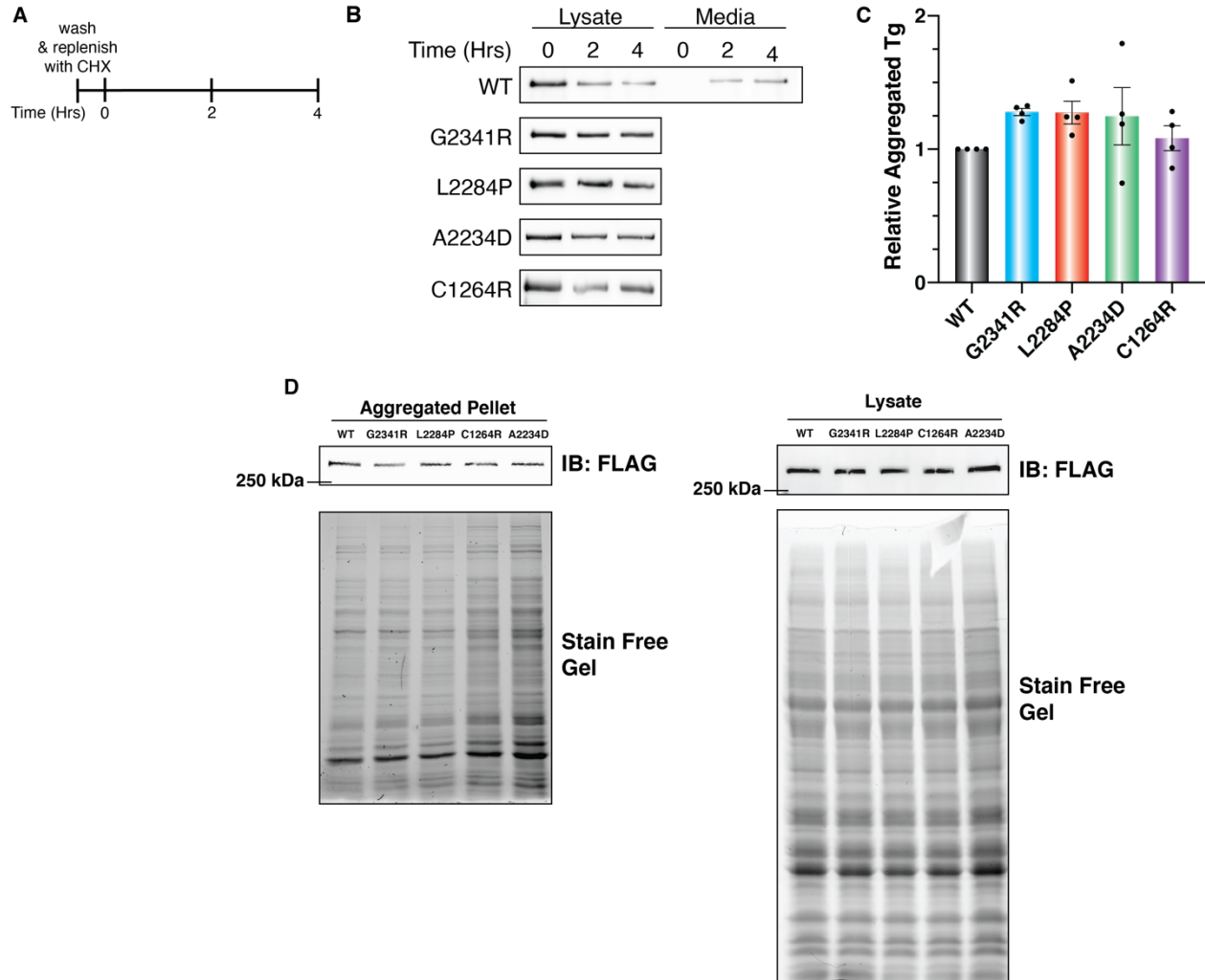


**Figure A.5. Cycloheximide chase and aggregation analysis of Tg.**

(A) Treatment scheme for cycloheximide (CHX) chase assay.

(B) Representative immunoblots from CHX chase assays to measure degradation rates of Tg variants.

(C) Relative quantification of Tg aggregation.

(D) Representative immunoblots and corresponding gels from solubilized aggregates and cell lysates.

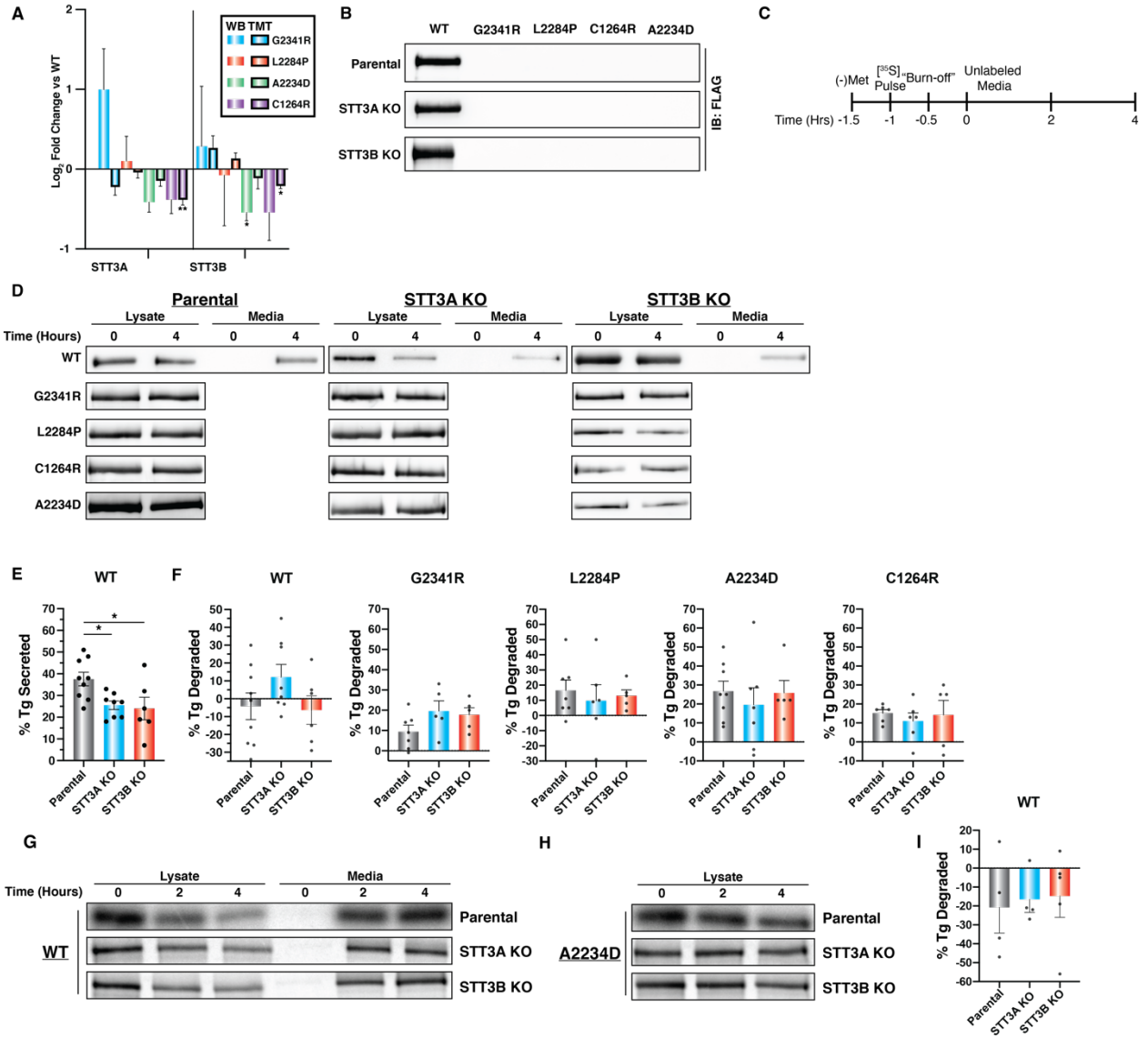


**Figure A.6. Cycloheximide chase and pulse-chase assays to measure Tg processing in STT3A and STT3B KO cells.**

(A) Confirmation of decreased protein interactions with the OST subunits STT3A and STT3B by Co-IP.

(B) Immunoblots of immunoprecipiated media samples from cells transiently transfected with respective FLAG-tagged Tg plasmid constructs.

(C) Representative immunoblots from CHX chase assays performed using STT3A and STT3B KO cells.

(D) Workflow for <sup>35</sup>S-metabolic labeling and pulse-chase assay.

(E) Plot showing the quantified changes in secretion for WT Tg as measured by CHX chase assay in parental, STT3A or STT3B KO cells.

(F) Plots showing the quantified changes in Tg degradation as measured by CHX chase assay in parental, STT3A or STT3B KO cells.

(G and H) Representative autoradiograms of <sup>35</sup>S-pulse chase experiment to measure Tg secretion and degradation.

(I) Plot showing the quantified changes in WT Tg degradation as measured by <sup>35</sup>S-pulse chase experiments.

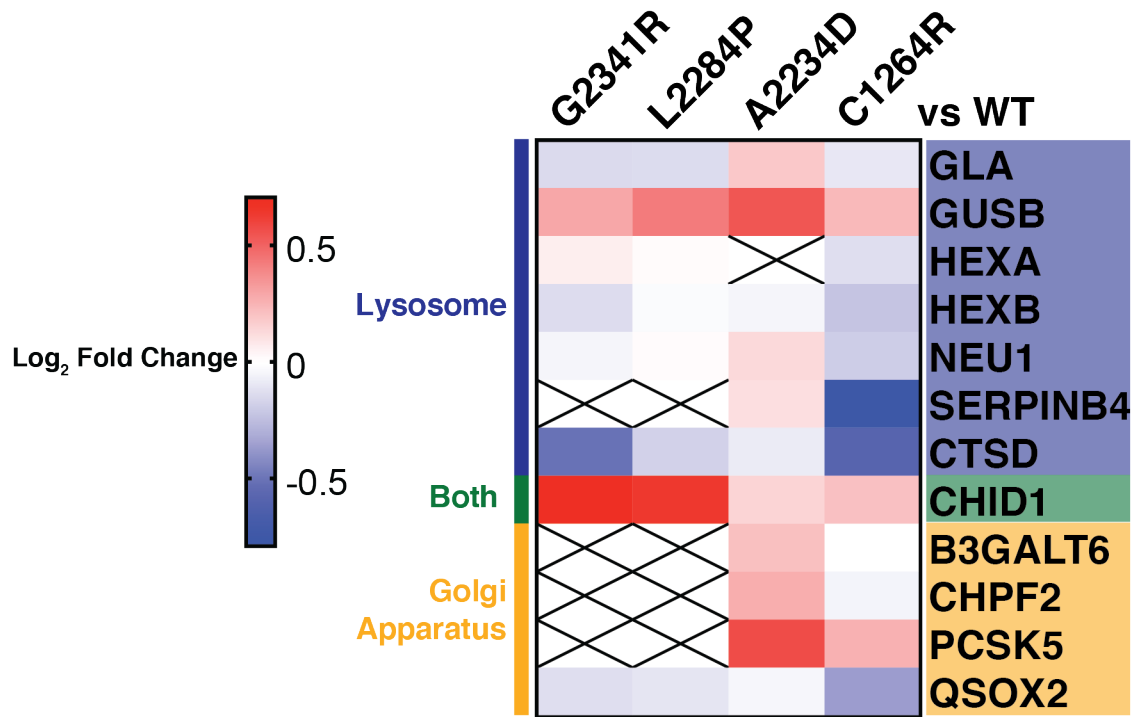


Figure A.7. Heatmap of lysosomal and Golgi interaction changes between mutant Tg variants and WT Tg.

**Table A.1 Construct Specific Interactors**

<b>Accession</b>	<b>Gene</b>	<b>WT</b>	<b>G2341R</b>	<b>L2284P</b>	<b>A2234D</b>	<b>C1264R</b>
P01266	TG	x	x	x	x	x
P62736	ACTA2					x
Q9UHI8	ADAMTS1	x	x	x		
O00468	AGRN					x
O75342	ALOX12B	x		x		
Q9NQW6	ANLN					x
P05090	APOD					x
Q5T5U3	ARHGAP21				x	
Q13510	ASAH1	x				
Q12797	ASPH		x	x		
O75882	ATRN					x
P25311	AZGP1					x
Q96L58	B3GALT6					x
Q9P1Z2	CALCOCO1					x
Q9NZT1	CALML5				x	
P27797	CALR*	x	x	x		x
O43852	CALU		x	x		x
P27824	CANX*		x	x		x
Q96CT7	CCDC124	x				
Q9ULG6	CCPG1	x			x	x
P11802	CDK4				x	
Q00535	CDK5					x
Q9BWS9	CHID1	x	x	x		x
Q9P2E5	CHPF2					x
P30532	CHRNA5				x	x
Q07065	CKAP4	x	x	x		x
Q96KA5	CLPTM1L	x				x
P10909	CLU		x	x		x
Q9Y2B0	CNPY2			x		x
O43405	COCH	x	x	x	x	x
Q05707	COL14A1					x
Q8NBJ5	COLGALT1	x	x	x		x
Q6UXH1	CRELD2		x	x		x
O75718	CRTAP	x	x	x		x
P07339	CTSD*					x
P39656	DDOST*		x	x		x

Q6IAN0	DHRS7B		x			
Q9UBS4	DNAJB11*	x	x	x		x
Q8IXB1	DNAJC10	x	x	x	x	x
Q13217	DNAJC3	x	x	x		x
Q9BZG8	DPH1					x
Q14574	DSC3				x	
Q14126	DSG2	x				
Q9BZQ6	EDEM3*		x	x		x
Q3B7T1	EDRF1					x
Q96EB1	ELP4					x
Q8N766	EMC1					x
P06733	ENO1				x	
Q9NZ08	ERAP1	x				x
Q96DZ1	ERLEC1	x			x	x
O75477	ERLIN1					x
Q86YB8	ERO1LB	x	x	x		x
P30040	ERP29*	x	x	x		x
Q9BS26	ERP44		x	x		x
Q9BXW9	FANCD2				x	x
Q8TB52	FBXO30					x
Q96AY3	FKBP10	x	x	x		x
O95302	FKBP9		x	x		x
P20930	FLG					x
Q5D862	FLG2					x
Q8IWF2	FOXRED2	x	x	x		x
Q9BTY2	FUCA2	x	x	x	x	x
Q14697	GANAB	x	x	x		x
P06280	GLA					x
P08236	GUSB		x	x		x
P06865	HEXA	x	x	x		x
P07686	HEXB					x
P16190	HLA-A			x		
P10321	HLA-C		x			
Q86YZ3	HRNR		x	x		
P14625	HSP90B1*	x	x	x		x
P11021	HSPA5*	x	x	x		x
Q9Y4L1	HYOU1*	x	x	x		x
O00458	IFRD1				x	
Q70UQ0	IKBIP					x

P58166	INHBE				x	x
P14923	JUP		x			
Q6UW63	KDELC1*	x	x	x		x
P13645	KRT10					x
P35908	KRT2	x				x
Q9C075	KRT23		x	x		
Q15323	KRT31			x		x
Q14525	KRT33B			x		
Q92764	KRT35			x		x
O76013	KRT36			x		
P19013	KRT4					x
P48668	KRT6C				x	
Q86Y46	KRT73		x			x
Q01546	KRT76	x				
Q7Z794	KRT77					x
Q5XKE5	KRT79	x			x	
P78385	KRT83			x		x
Q9NSB2	KRT84			x		
P07942	LAMB1	x	x	x		x
P55268	LAMB2					x
Q13751	LAMB3	x	x	x		x
P11047	LAMC1		x			x
Q14847	LASP1				x	x
Q32P28	LEPRE1	x	x	x		x
Q8IVL6	LEPREL2	x	x	x		x
Q92791	LEPREL4	x	x	x		x
Q08380	LGALS3BP	x	x	x		x
P49257	LMAN1	x	x	x		x
Q9UIQ6	LNPEP		x			x
P30533	LRPAP1					x
Q86X29	LSR	x	x			
P61626	LYZ					x
Q9H0U3	MAGT1*		x	x		x
P46734	MAP2K3					x
P48163	ME1	x				
Q14696	MESDC2	x	x	x		x
Q8N3F8	MICALL1				x	x
Q13724	MOGS*		x	x		x
P54920	NAPA	x				



Q69YL0	NCBP2AS2					X
O75306	NDUFS2	x				
Q99519	NEU1		x	x		x
P14543	NID1		x	x		
Q9BYG3	NIFK					x
Q5JPE7	NOMO2	x	x	x		x
O00567	NOP56		x	x		
P48745	NOV				x	
Q02818	NUCB1	x				x
P80303	NUCB2					x
Q8TEM1	NUP210		x			x
Q13438	OS9*	x	x	x		x
P13674	P4HA1	x	x	x		x
O15460	P4HA2	x	x	x	x	x
P07237	P4HB*	x	x	x		x
P61457	PCBD1	x				
Q92824	PCSK5	x			x	x
P30101	PDIA3*	x	x	x		x
P13667	PDIA4*	x	x	x		x
Q15084	PDIA6*	x	x	x		x
Q8IV08	PLD3		x	x		
Q15149	PLEC	x				
Q02809	PLOD1	x	x	x		x
O00469	PLOD2	x	x	x		x
O60568	PLOD3	x	x	x		x
Q92871	PMM1					x
Q8WVV4	POF1B	x		x		
O15160	POLR1C	x				
P23284	PPIB	x	x	x		x
Q13162	PRDX4	x	x	x		x
P14314	PRKCSH	x	x	x		x
P25786	PSMA1*		x			
P15151	PVR				x	
Q92626	PXDN					x
Q6ZRP7	QSOX2	x	x	x		
P15153	RAC2*	x				
Q6GYQ0	RALGAPA1				x	
O60518	RANBP6				x	
Q96PK6	RBM14	x				

Q96I25	RBM17		x			
Q15293	RCN1	x	x	x		x
Q14257	RCN2	x	x	x		x
Q9Y6B6	SAR1B			x		
Q99470	SDF2	x	x	x		x
Q9HCN8	SDF2L1	x	x	x	x	x
Q9BRK5	SDF4	x	x	x	x	x
P67812	SEC11A*	x	x	x		x
Q9UBV2	SEL1L	x	x	x		x
O60613	SELENOF	x	x	x	x	x
P48594	SERPINB4				x	x
P50454	SERPINH1	x	x	x		x
Q13247	SRSF6				x	
P51571	SSR4*		x			
Q8TCJ2	STT3B*		x	x		x
Q8NBJ7	SUMF2	x	x	x		x
O75683	SURF6		x			
Q86TM6	SYVN1*					x
Q8TC07	TBC1D15		x			
Q92734	TFG				x	
P02786	TFRC	x	x	x		x
Q04726	TLE3			x		
Q9H3N1	TMX1		x			
O14656	TOR1A		x	x		x
O14657	TOR1B		x	x		
Q9UJA5	TRMT6	x				
Q8NBP0	TTC13					x
P68366	TUBA4A	x				
Q9BSJ2	TUBGCP2					x
Q8NBS9	TXNDC5	x	x	x		x
Q9NYU2	UGGT1*	x	x	x		x
Q9NYU1	UGGT2	x	x	x		x
P55072	VCP*					x
Q5VVQ6	YOD1					x

\*Previously identified interactor

**Table A.2 Pathway Enrichment Analysis for Tg Interactors**

<b>Import</b>	<b>Glycan Processing</b>	<b>Hsp70/90 Assisted Folding</b>	<b>Disulfide Processing</b>	<b>Collagen Processing</b>	<b>Trafficking</b>	<b>Degradation</b>	<b>Miscellaneous</b>
SEC11A	MAGT1	CLU	PDIA3	COL14A1	LRPA P1	VCP	TOR1A
SSR4	STT3B	HSP90B1	ERP44	SERPINH1	CDK5	SYVN1	TOR1B
	DDOST	SDF2L1	TMX1	PPIB	CDK4	ERAP1	SELENOF
	CHID1	HYOU1	P4HB	NID1	SDF4	LNPEP	SUMF2
	NEU1	DNAJC10	QSOX2	COCH	LMAN1	PSMA1	LAMB3
	MOGS	DNAJC3	PDIA6	PLOD3	SAR1B	ADAMTS1	NOMO2
	GUSB	HSPA5	PDIA4	FKBP10	RAC2	PCSK5	RCN2
	KDEL1C1	DNAJB11	TXNDC5	FKBP9	MICALL1	NDUFS2	CKAP4
	B3GALT6		DNAJC10	LEPREL4	TBC1D15	YOD1	TFRC
	HEXB		ERP29	COLGALT1	NAPA	NEU1	LAMB1
	HEXA		EROLB	LEPREL2		SERPINB4	RCN1
	UGGT2		PRDX4	P4HA1		CTSD	MESDC2
	UGGT1			PLOD1		FOXRED2	COCH
	SDF2			P4HA2		FBXO30	CHID1
	GLA			CRTAP		ERLIN1	SDF4
	PMM1			LEPRE1		OS9	ASPH
	CHPF2			PLOD2		SEL1L	CALU
	CALR					EDEM3	LAMC1
	STT3A						DHRS7B

	GANAB						
	PRKCSH						
	CANX						
	PDIA3						
	LMAN1						

**Table A.3 Biological Significance for Tg Mutations**

Missense Mutation	Tg Region	Biological Significance	References (First Author, Year, Ref.)
G2341R	ChEL Domain	Novel mutation first presented here, exhibits trafficking phenotype similar to that of L2284P Tg	N/A
L2284P	ChEL Domain	Originally discovered in cog/cog mice resulting in congenital hypothyroidism with goiter; expression known to activate the unfolded protein response (UPR); thyrocytes shown to survive under chronic stress due to expression of the misfolded construct; protein-protein interaction partners and associated changes are uncharacterized	Kim, 1996, 9. Medeiros-Neto, 1996, 10. Kim, 1998, 39. Park, 2004, 16.
A2234D	ChEL Domain	Originally discovered in human patients resulting in congenital hypothyroidism with goiter; low levels of secretion may be present to produce sufficient thyroid hormones for proper embryonic development, protein-protein interaction partners and associated changes are uncharacterized	Caputo, 2007, 40. Pardo, 2008, 78. Pardo, 2009, 43.
C1264R	Hinge/Flap Region	Originally discovered in human patients resulting in congenital hypothyroidism with goiter; expression linked to the activation of the unfolded protein response (UPR); expression of this construct in patients is correlated with increased D2 activity (D2, deiodinase enzyme responsible for the conversion of T4 to T3);	Hishinuma, 1999, 17. Kanou, 2007, 66.

**Table A.4 Oligos Sequences**

<b>Target</b>	<b>Forward</b>	<b>Reverse</b>	<b>Purpose</b>
G2341R Tg-FT	GAGTGGGTGTCTTCC GCTTCCTGAGTTC	GAACTCAGGAAG CGGAAGACACCC ACTC	Site Directed Mutagenesis of WT Tg-FT
L2284P Tg-FT	GAAGATTGTTTGTAT CCCAATGTGTTTCATC CCTC	GAGGGATGAACA CATTGGGATACAA ACAATCTTC	Site Directed Mutagenesis of WT Tg-FT
A2234D Tg-FT	AGTTCCATATGATGC CCCGCCCC	GAAGCAAGTGGA CCAGTTCCTTGG	Site Directed Mutagenesis of WT Tg-FT
C1264R Tg-FT	CAGGGCCATTGATAC GTAGCCTGGAGAGC	GCTCTCCAGGCTA CGTATCAATGGCC CTG	Site Directed Mutagenesis of WT Tg-FT
D2769X Tg (Untagged WT)	GCTCTAAGACCTACA GCAAGTGATACAAGG ATGACGACGATAAG	CTTATCGTCGTCA TCCTTGTATCACT TGCTGTAGGTCTT AGAGC	Site Directed Mutagenesis of WT Tg-FT

**File A.1: Raw TMT data used for processing and figure generation**

## Appendix B

### Supplementary Materials for Chapter 3

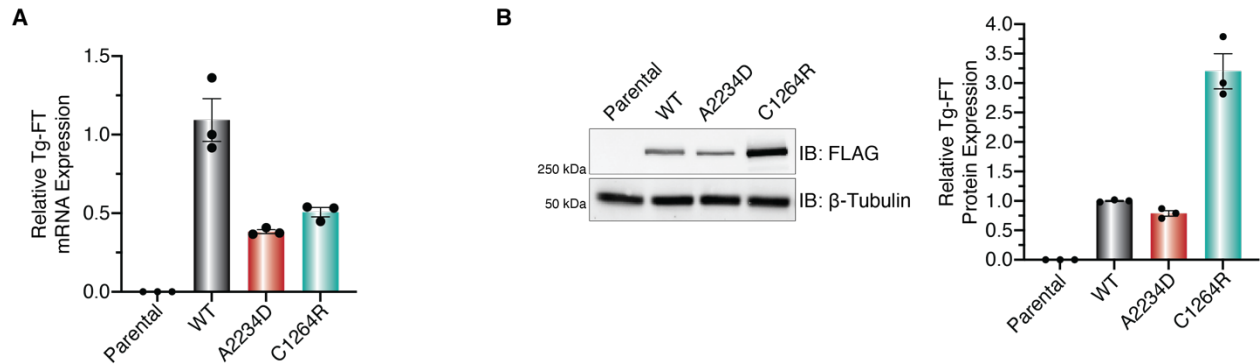


#### Figure B.1 Validation of Stable Cell Lines

(A) Relative expression of Tg-FT RNA in engineered FRT cells measured by qRT-PCR. Data is median normalized to WT Tg-FT expression and represented as mean  $\pm$  SEM.

(B) Relative expression of Tg-FT in engineered FRT cells measured by western blot analysis. Data is median normalized to WT Tg-FT expression and represented as mean  $\pm$  SEM.



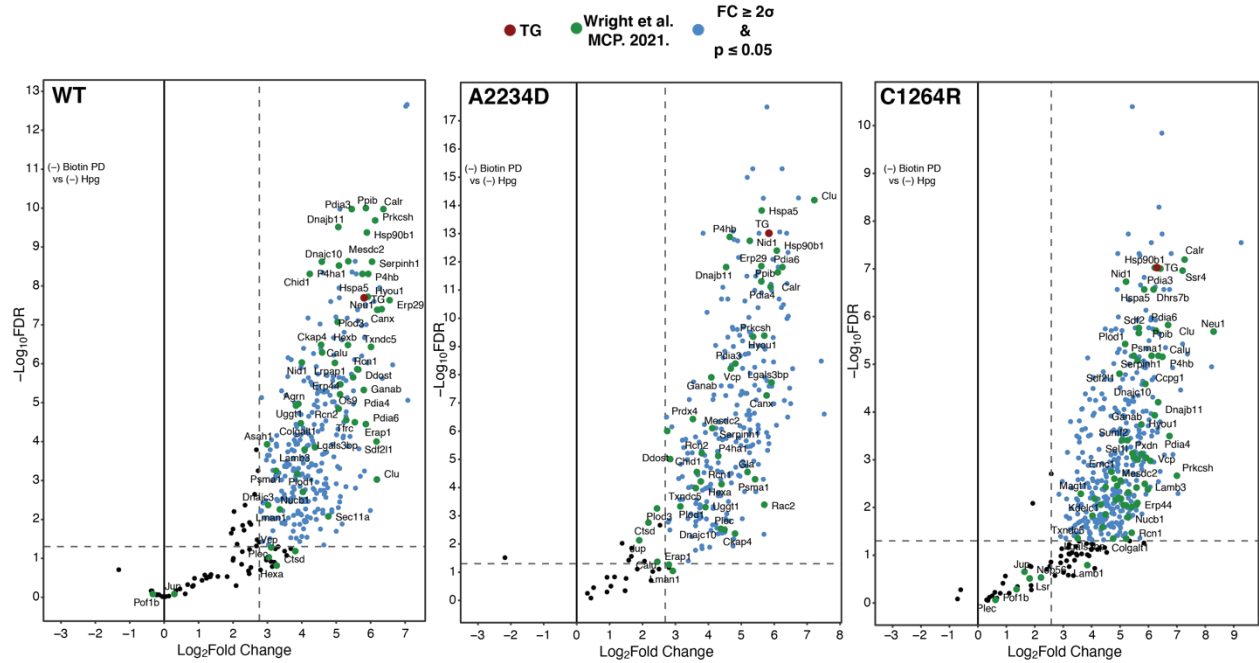


**Figure B.2. (-) Biotin Pulldown Carrier Samples Allow for Identification of Tg Interactors**

Volcano plots for the comparison of (-) biotin pulldown vs (-) Hpg samples to identify Tg interactors in FRT cells. Plots show the average log<sub>2</sub> difference vs FDR estimation (benjamini-hochberg).

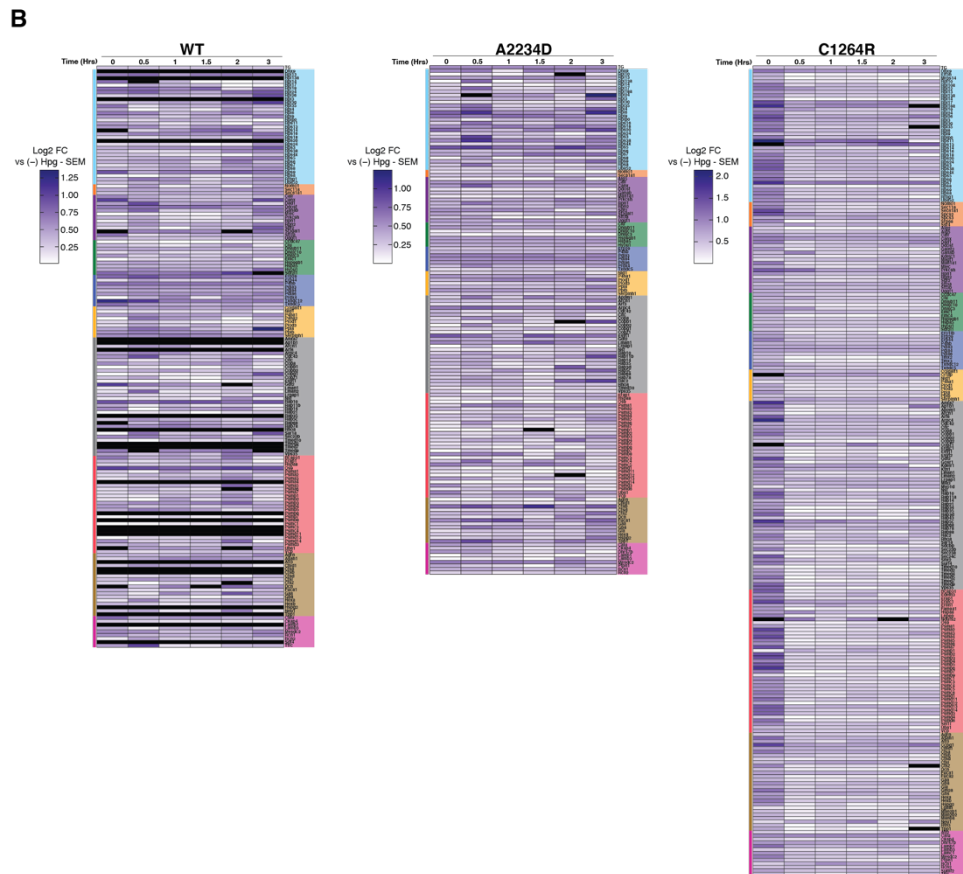
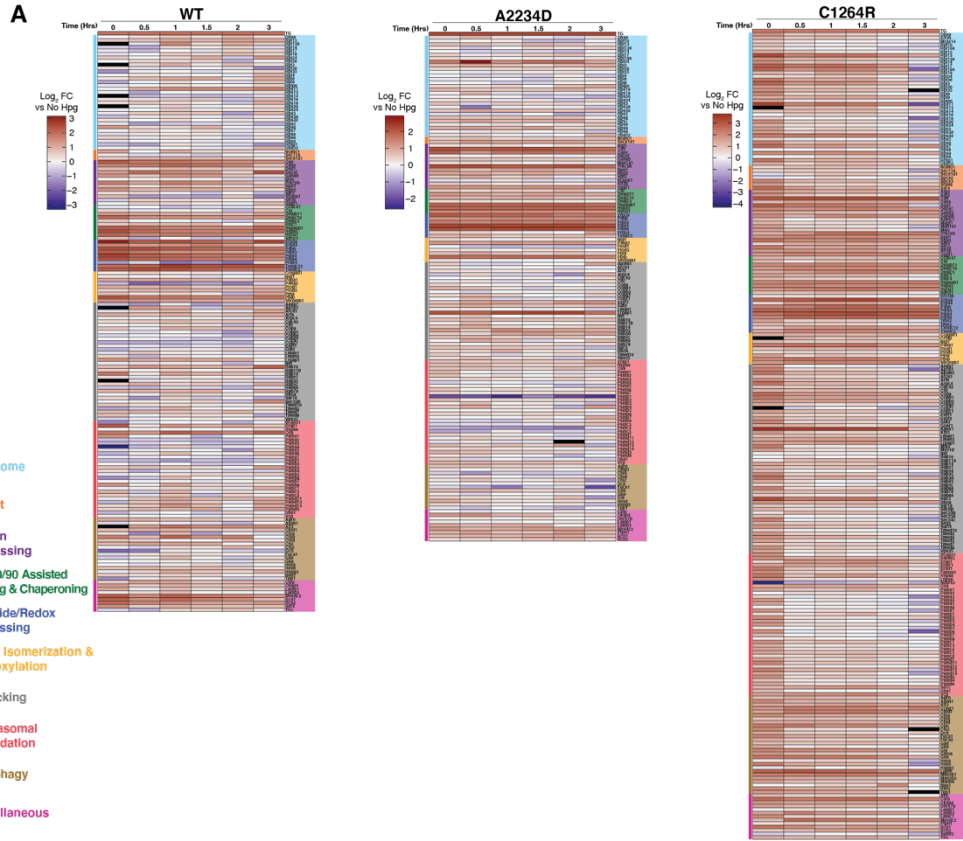


**Figure B.3. Summary of Tg TRIP Data – Heatmaps**

(A) Analysis showing the  $\log_2$  fold change enrichment of Tg interactors measured by TRIP.

(B) Analysis showing the SEM of  $\log_2$  fold change enrichment of Tg interactors measured by TRIP.



**Figure B.4. Tg TRIP Data – Scaled Heatmap**

Analysis showing the scaled  $\log_2$  fold change enrichment of Tg interactors measured by TRIP for time-resolved analysis.

**Table B.1 Pathway Enrichment Analysis for Tg Interactors**

Ribosome	Import	Glycosylation	Hsp40/70/90 & Other Chaperoning Activity	Disulfide Bond Formation	Proline Isomerization, Hydroxylation, & Collagen Processing	Trafficking	Protein Ubiquitination & Proteasomal Degradation	Autophagy & Lysosomal Processing	Miscellaneous
Dhx9	Nomo1	Alg2	Ccdc47	Ero1lb	Col14a1	Anxa7	Adamts1	Agrn	Asph
Eif3h	Sec11a	Alg5	Clu	Erp29	Colgalt1	Ap1b1	Bcap31	Asah1	Atl2
Mrps14	Sec61a1	B3galt6	Dnajb11	Erp44	Crtap	Ap2m1	Edem3	Ati3	Calu
Rpl10	Spcs2	Calr	Dnajc10	P4hb	Fkbp10	Arcn1	Erap1	Ccpg1	Ckap4
Rpl10a	Spcs3	Canx	Dnajc3	Pdia3	Fkbp9	Arf3	Erlec1	Chid1	Coch
Rpl12	Srp68	Chpf2	Emc1	Pdia4	Lepre1	Arf6	Erlin1	Ctsa	Dhrs7b
Rpl13	Ssr4	Dad1	Emc4	Pdia6	Leprel2	Arpc4	Fam8a1	Ctsb	Lamb1
Rpl13a		Ddost	Hsp90b1	Prdx4	Leprel4	Cdc42	Fbxo30	Ctsd	Lamb3
Rpl14		Galnt2	Hspa5	Qsox2	Nid1	Cdk4	Foxred2	Ctsl	Lamc1
Rpl17		Ganab	Hyou1	Selenof	P4ha1	Cdk5	Hspa8	Ctsz	Mesdc2
Rpl18a		Kdelc1	Sdf211	Tmx1	P4ha2	Citc	Lnpep	Dcn	Nomo2
Rpl19		Magt1		Tmx2	Plod1	Copa	Ndufs2	Fuca1	Ptpn1
Rpl24		Man1a1		Tmx3	Plod2	Copb1	Os9	Fuca2	Rcn1
Rpl26		Mlec		Txndc12	Plod3	Copb2	Pcsk5	Gaa	Rcn2
Rpl3		Mogs		Txndc5	Ppia	Copg1	Psma1	Gba	Sdf4
Rpl30		Pmm1			Ppib	Copg2	Psma2	Gla	Sumf2
Rpl35		Prkcs h			Serpinh1	Copz1	Psma3	Gm2a	Tfrc
Rpl4		Rpn1				Ergic1	Psma4	Gns	
Rpl6		Rpn2				Esyt1	Psma5	Gusb	
Rpl9		Sdf2				Esyt2	Psma6	Hexa	
Rplp0		St3gal1				Gdi2	Psma7	Hexb	
Rps11		Stt3a				Gosr1	Psmb1	Hspg2	
Rps13		Stt3b				Kdelr1	Psmb2	Lgmn	
Rps14		Uggt1				Ktn1	Psmb3	Man2b1	

Rps16		Uggt2				Lman1	Psmb4	Man2b 2	
Rps18						Lman2	Psmb5	Manba	
Rps20						Lrpap1	Psmb6	Neu1	
Rps24						Mia3	Psmb7	Rtn3	
Rps3						Micall1	Psmb8	Tpp1	
Rps3a						Myo1d	Psmb9		
Rps4x						Napa	Psmc1		
Rps5						Nsf	Psmc3		
Rps6						Pdcd6lp	Psmc4		
Rps7						Rab1	Psmc5		
Rps8						Rab10	Psmc6		
Rps9						Rab11a	Psmc1		
Rpsa						Rab11b	Psmc11		
Rrbp1						Rab14	Psmc12		
Uba5 2						Rab21	Psmc13		
						Rab34	Psmc14		
						Rab35	Psmc3		
						Rab3d	Psmc4		
						Rab43	Psmc6		
						Rab5c	Sel1l		
						Rab6a	Serpinb4		
						Rab7a	Syvn1		
						Rab8a	Uba1		
						Rac2	Vcp		
						Rhoa	Yod1		
						Sar1a			
						Sar1b			
						Sdcbp			
						Sec22b			
						Sec23a			
						Sec24c			
						Snx2			
						Surf4			
						Tbc1d1 5			
						Tmed10			
						Tmed2			
						Tmed4			

						Tmed5			
						Tmed7			
						Tmed9			
						Vps35			

**Table B.2 Oligos Sequences**

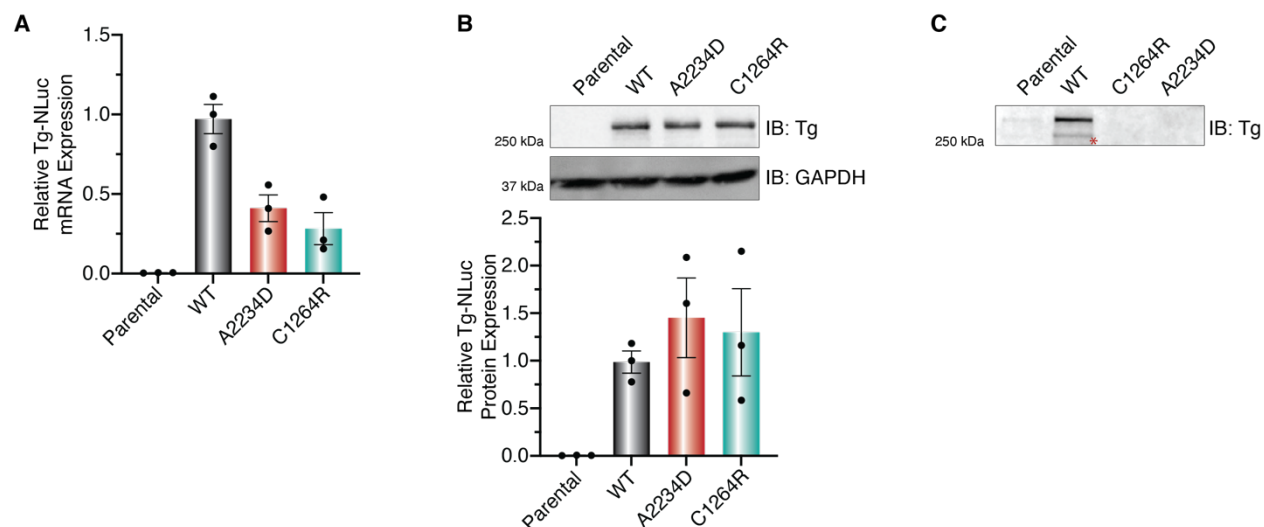
<b>Target</b>	<b>Forward</b>	<b>Reverse</b>	<b>Purpose</b>
pcDNA3.1_Tg-FT	TTAATACGACTCACTATA GGGAGACCCAAGCTGGC TAG	ACTAGAAGGCACAGTCGA GGCTGATCAGCGGTTTAT CAC	amplification of WT Tg-FT from pcDNA3.1 plasmid
pcDNA5/FRT_Tg-FT	TTAATACGACTCACTATA GGGAGACCCAAGCTGGC TAG	CTTGCTGTAGGTCTTAGAG CCT	amplification of WT Tg from pcDNA5/FRT-Tg-FLAG
pcDNA5/FRT	CCTCGACTGTGCCTTCTA G	CCTATAGTGAGTCGTATTA ATTTCCG	amplification of empty pcDNA5/FRT expression vector
C1264R Tg-FT	CATTGATACGTAGCCTGG AGAGCGGACG	GCCCTGGTGGAAACACGTC	Site-Directed Mutagenesis of WT Tg-FT
A2234D Tg-FT	AGTTCCATATGATGCCCC GCCCC	CCAAGGAACTGGTCCACTT GCTTC	Site-Directed Mutagenesis of WT Tg-FT



**File B.1: Output from data processing using DEP package**

**File B.2: Raw TMT data used for processing and figure generation**

## Supplementary Materials for Chapter 4

**Figure C.1. Validation of Stable Cell Lines**

(A) Relative expression of Tg-NLuc RNA in engineered HEK293 cells measured by qRT-PCR. Data is median normalized to WT Tg-NLuc expression and represented as mean  $\pm$  SEM.

(B) Relative expression of Tg-NLuc in lysate engineered HEK293 cells measured by western blot analysis. Data is median normalized to WT Tg-NLuc expression and represented as mean  $\pm$  SEM.

(C) Western blot of analysis of media aliquots from HEK293 expressing Tg-NLuc constructs. WT Tg secretion is maintained, and mutant Tg secretion deficiency is not altered.



**Figure C.2. Summary of siRNA Screening Data**

(A) Analysis showing the relative Tg-NLuc abundance changes in lysate with siRNA silencing of select genes. Genes identified as hits are annotated within the heatmap.

(B) Analysis showing the relative Tg-NLuc abundance changes in media with siRNA silencing of select genes. Genes identified as hits are annotated within the heatmap.

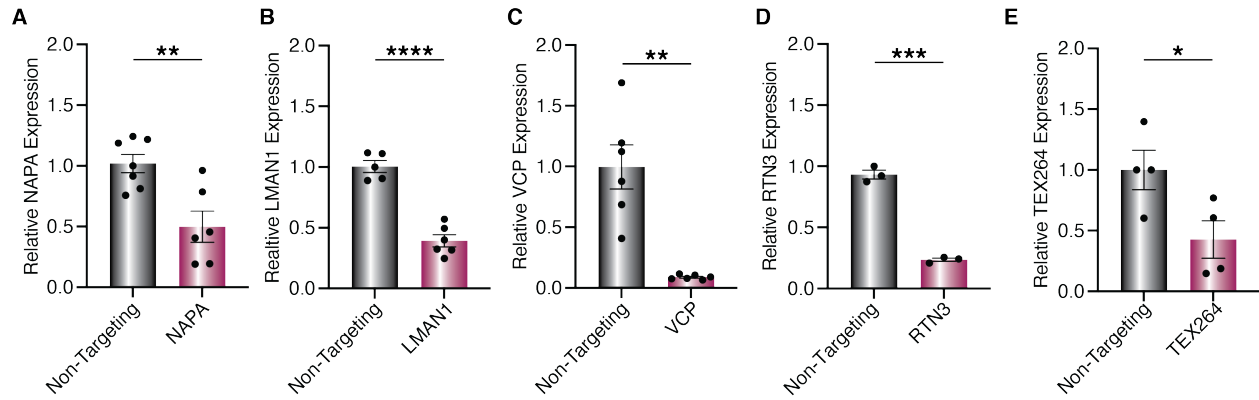


### Figure C.3. Validation of siRNA Screening Hits in FRT Cells

(A) Relative expression of NAPA ( $\alpha$ -SNAP) RNA in engineered WT Tg-FT FRT cells measured by qRT-PCR. Data is median normalized to Non-Targeting siRNA treated cells and represented as mean  $\pm$  SEM.

(B) Relative expression of LMAN1 RNA in engineered WT Tg-FT FRT cells measured by qRT-PCR. Data is median normalized to Non-Targeting siRNA treated cells and represented as mean  $\pm$  SEM.

(C) Relative expression of VCP RNA in engineered C1264R Tg-FT FRT cells measured by qRT-PCR. Data is median normalized to Non-Targeting siRNA treated cells and represented as mean  $\pm$  SEM.

(D) Relative expression of TEX264 RNA in engineered C1264R Tg-FT FRT cells measured by qRT-PCR. Data is median normalized to Non-Targeting siRNA treated cells and represented as mean  $\pm$  SEM.

(E) Relative expression of RTN3 RNA in engineered C1264R Tg-FT FRT cells measured by qRT-PCR. Data is median normalized to Non-Targeting siRNA treated cells and represented as mean  $\pm$  SEM.

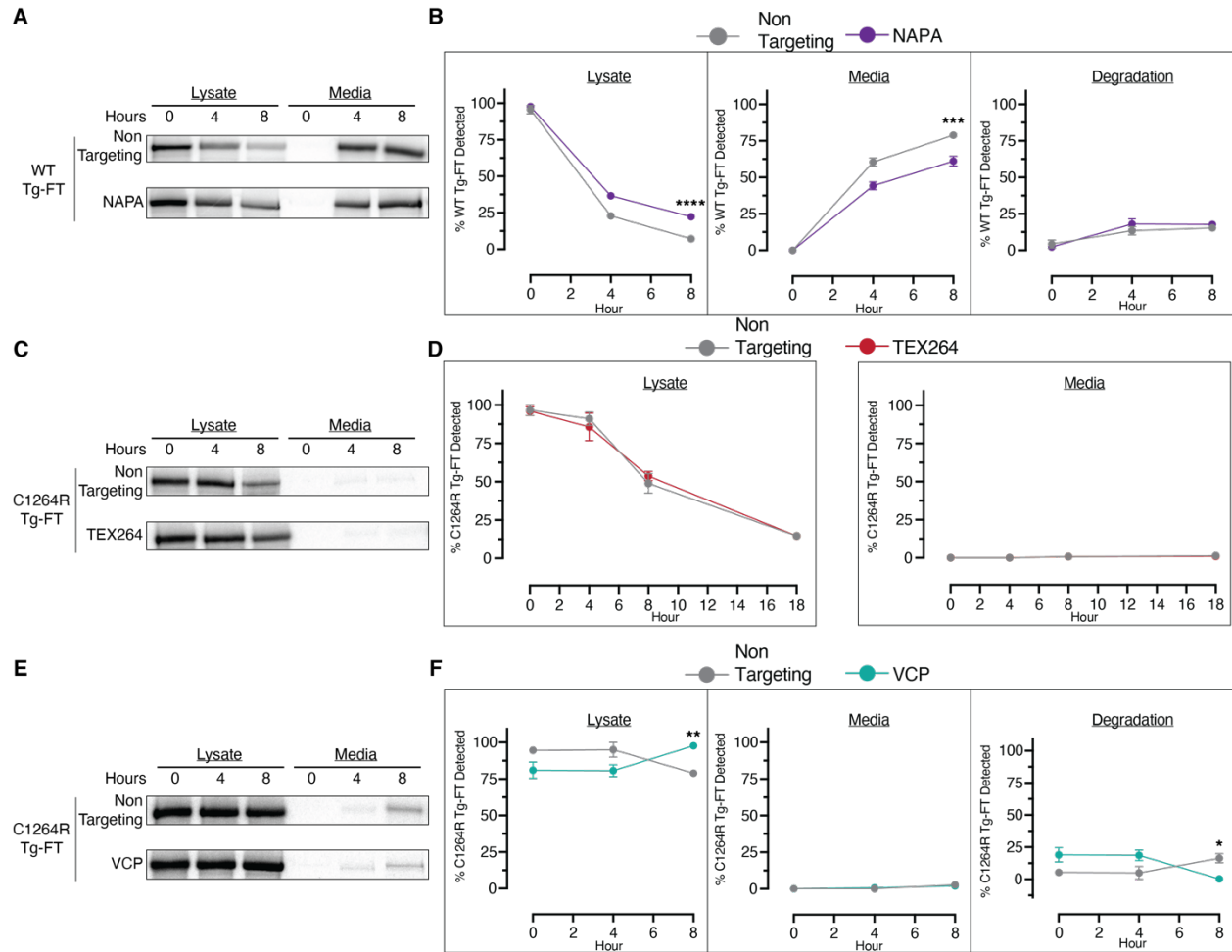
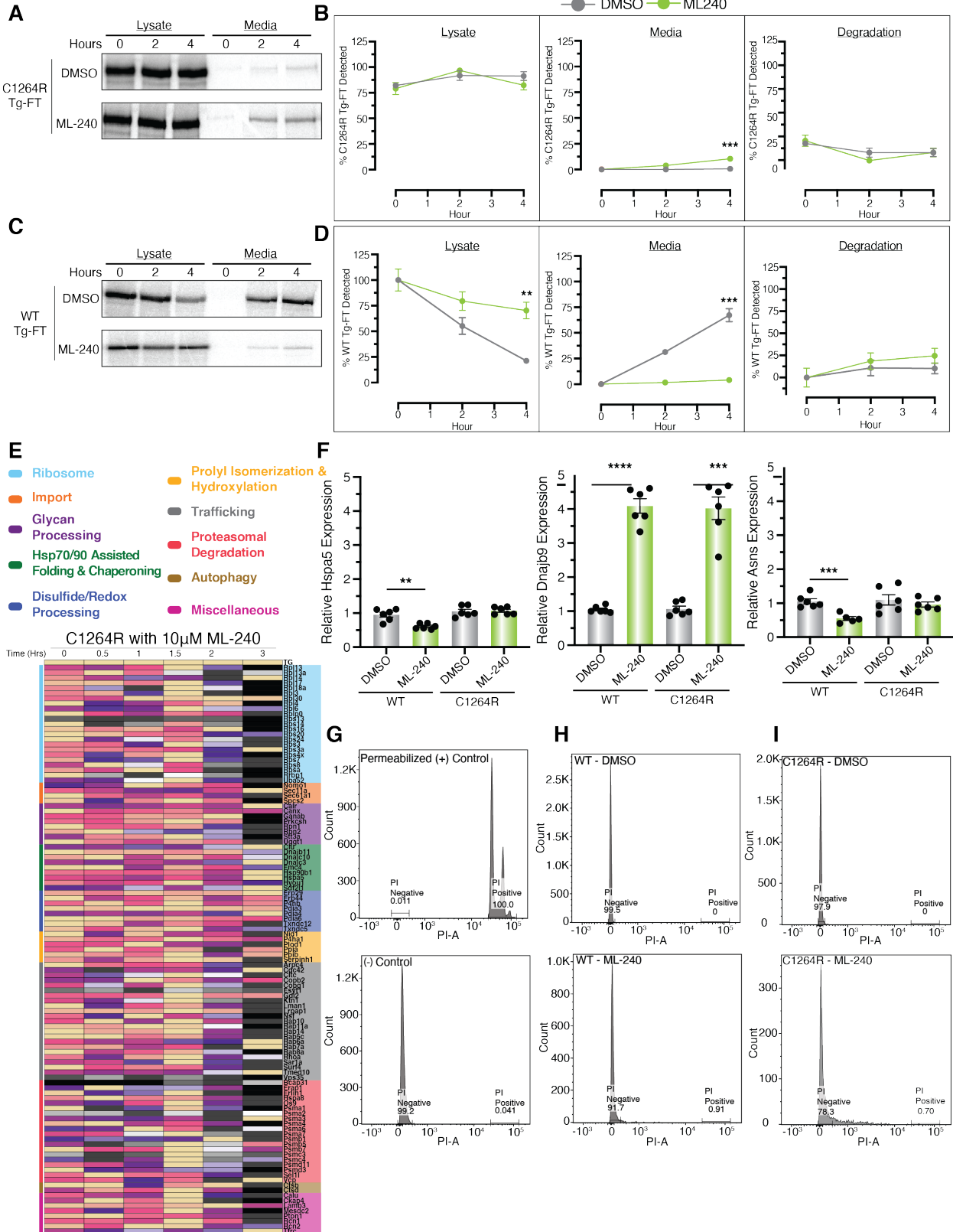


Figure C.4. Pulse Chase Analysis of WT and C1264R Tg-FT with siRNA Silencing (A and B) Pulse-chase analysis of WT Tg-FT in FRT cells with NAPA ( $\alpha$ -SNAP) siRNA silencing. Data is median normalized to Non-Targeting siRNA treated cells and represented as mean  $\pm$  SEM. (C and D) Pulse-chase analysis of C1264R Tg-FT in FRT cells with TEX264 siRNA silencing. Data is median normalized to Non-Targeting siRNA treated cells and represented as mean  $\pm$  SEM. (E and F) Pulse-chase analysis of C1264R Tg-FT in FRT cells with VCP siRNA knockdown. Data is median normalized to Non-Targeting siRNA treated cells and represented as mean  $\pm$  SEM.



**Figure C.5. Pharmacological VCP Inhibition with WT and C1264R Tg-FT FRT Cells**

(A and B) Pulse-chase analysis of C1264R Tg-FT in FRT cells with ML-240 treatment. Data is represented as mean  $\pm$  SEM.

(C and D) Pulse-chase analysis of WT Tg-FT in FRT cells with ML-240 treatment. Data is represented as mean  $\pm$  SEM.

(E) Analysis showing the scaled Log<sub>2</sub> FC enrichment of Tg interactors measured by TRIP for C1264R in the presence of ML-240 treatment.

(F) Assessment of UPR up regulation with ML-240 treatment. Only Dnajb9 shows a significant increase in transcript levels while, Hspa5 and Asns remain largely unchanged, and decreased in the case of WT Tg.

(G) Propidium iodide control samples showing propidium iodide positive and propidium iodide negative populations used for viability staining.

(H) Propidium iodide viability staining of WT Tg-FT FRT cells with ML-240 treatment.

(I) Propidium iodide viability staining of C1264R Tg-FT FRT cells with ML-240 treatment.



**Table C.1 Oligos Sequences**

<b>Target</b>	<b>Forward</b>	<b>Reverse</b>	<b>Purpose</b>
rat_GA PDH	CAAGTTCAACGGCACAGTCAAG	ACATACTCAGCACC AGCATCAC	qRT-PCR
human_ GAPDH	GTCGGAGTCAACGGATT	AAGCTTCCCGTTCT CAG	qRT-PCR
rat_VC P	CCAAGGCTCGTGGTGGTAAT	TTAGGATGGCAACA CGGGAC	qRT-PCR
rat_TEX 264	GAGCTGATACAAGTGACGCG	CTGTAGCTGTGCTC GCTGCG	qRT-PCR
rat_NA PA	GCCAACAAGTGTCTGCTGAA	AGCATGTTCGATGCA GAAGTG	qRT-PCR
rat_LM AN1	GAAAAACCAAATGCCCAGA	CAAAGCAAACGAG ACCATT	qRT-PCR
rat_RT N3	TGAGGACCACTGAGCCCCACTG	TGACTCCAAGCAGC TGCATGCC	qRT-PCR
pcDNA 5/FRT_ Tg-FT	TTAATACGACTCACTATAGGGAG ACCCAAGCTGGCTAG	CTTGCTGTAGGTCT TAGAGCCT	amplification of WT Tg from pcDNA5/FR T-Tg-FLAG
C1264R Tg-FT	CATTGATACGTAGCCTGGAGAG CGGACG	GCCCTGGTGGAAC ACGTC	Site- Directed Mutagenesis of WT Tg- NLuc
A2234D Tg-FT	AGTTCCATATGATGCCCCGCC C	CCAAGGAACTGGTC CACTTGCTTC	Site- Directed Mutagenesis of WT Tg- NLuc
Nluc	GCTCTAAGACCTACAGCAAGCTCGGCTCGAGCGGCGT CTTCACACTCGAAGATTTTCGTTGGGGACTGGCGACAGA CAGCCGGCTACAACCTGGACCAAGTCCCTTGAACAGGG AGGTGTGTCCAGTTTGTTCAGAATCTCGGGGTGTCCG TAACTCCGATCCAAAGGATTGTCCTGAGCGGTGAAAAT GGGCTGAAGATCGACATCCATGTCATCATCCCGTATGA AGGTCTGAGCGGCGACCAAATGGGCCAGATCGAAAAA ATTTTAAAGGTGGTGTACCCTGTGGATGATCATCACTTT AAGGTGATCCTGCACTATGGCACACTGGTAATCGACGG GGTTACGCCGAACATGATCGACTATTTTCGGACGGCCGT ATGAAGGCATCGCCGTGTTTCGACGGCAAAAAGATCACT GTAACAGGGACCCTGTGGAACGGCAACAAAATTATCGA		Assembly of NLuc with Tg to generate Tg- NLuc fusion constructs

	CGAGCGCCTGATCAACCCCGACGGCTCCCTGCTGTTC CGAGTAACCATCAACGGAGTGACCGGCTGGCGGCTGT GCGAACGCATTCTGGCGTAATAAACCCGCTGATCAGCC TCGACTGTGCCTTCTAGT	
--	--	--

**File C.1: siRNA Screening Data for figure generation**

**File C.2: Raw TMT data used for processing and figure generation**

## Appendix D

### Curriculum Vitae

**Madison Taylor Wright**  
Doctoral Candidate  
Department of Chemistry  
Vanderbilt University  
1234 Stevenson Center Lane  
Nashville, TN 37212  
Office: 615-343-5372  
Cell: 205-807-5539  
madison.t.wright@vanderbilt.edu

---

#### Education

**Vanderbilt University** - Nashville, TN August 2017 – August 2022  
*Doctor of Philosophy in Chemistry*  
Thesis: “Investigations Into Time-Resolved Secretary Protein Quality Control Dynamics”  
Advisor: Dr. Lars Plate  
GPA: 3.76

**Jacksonville State University** – Jacksonville, AL August 2013 – December 2016  
*Bachelor of Science in Chemistry*  
Minor in Forensic Investigations  
Summa Cum Laude  
GPA: 3.94

#### Research & Professional Experience

Partner, S Phase BioFund March 2022 – Current  
*Vanderbilt University* – Nashville, TN

Graduate Research Assistant, Department of Chemistry January 2018 – August 2022  
*Vanderbilt University* - Nashville, TN

Quality Control Lab Technician February 2017 – July 2017  
*Evonik Industries* – Birmingham, AL

Undergraduate Research Assistant August 2016 - December 2016  
Department of Chemistry  
*Jacksonville State University* – Jacksonville, AL  
Principal Investigator: Nixon Mwebi, PhD

Undergraduate Research Assistant August 2016 – December 2016  
Department of Chemistry  
*Jacksonville State University* – Jacksonville, AL  
Principal Investigator: Jan Gryko, PhD

UAB - Partnership Research Summer Training Program May 2016 – July 2016  
*University of Alabama at Birmingham* – Birmingham, AL  
Principal Investigator: Sooryanarayana Varambally, PhD

### **Teaching Experience**

Graduate Teaching Assistant, Department of Chemistry August 2017 – December 2017  
General Chemistry Lab  
*Vanderbilt University* – Nashville, TN

Chemistry Tutor, Academic Center for Excellence February 2016 – May 2016  
General Chemistry  
*Jacksonville State University* – Jacksonville, AL

### **Grants and Fellowships**

National Institute of General Medical Sciences 2019 – September 2022  
(1R35GM133552)

National Science Foundation 2019 – September 2022  
Graduate Research Fellowship Training Program

National Institute of General Medical Sciences 2018 – 2019  
Chemistry-Biology Interface Training Grant  
(5T32GM065086-04)

Vanderbilt Institute of Chemical Biology Research Fellowship 2018

### **Honors and Awards**

Vanderbilt Institute of Chemical Biology Richard Armstrong Prize for Research Excellence 2021

Summa Cum Laude – Jacksonville State University 2016

Jacksonville State University Jazz Scholarship 2013 – 2016

Jacksonville State University Marching Southerners Scholarship 2013 – 2016

Jacksonville State University Faculty Academic Scholarship 2013 – 2016

### **Professional Memberships**

American Society for Mass Spectrometry 2019 – Present

United States Human Proteome Organization 2019 – Present

### **Professional Activities**

Chemical Biology Association of Students 2018 – Present

- ◇ Secretary (2020 – 2021)
- ◇ Executive Board Member (2019 – 2020)

Vanderbilt Mitchum E. Warren Fellowship Committee 2019 – 2021

Vanderbilt Chemistry Forum Committee 2018 – 2019

### **Presentations**

Temporally resolved protein-protein interactions to guide therapeutic intervention in protein misfolding diseases – Poster. United States Human Proteome Organization Annual Conference. Charleston, South Carolina. March 2022.

Developing a method to temporally resolve protein-protein interactions – Oral. Pfizer Chemistry Connect Symposium. Virtual Meeting. November 2021.

Developing a method to temporally resolve protein-protein interactions – Invited Oral. American Chemical Society – Rocky Mountain Regional Meeting. Tucson, Arizona. October 2021.

Protein-Protein Interactions in Quality Control: From Steady-State Interactions to Time-Resolved Dynamics – Invited Oral - Vanderbilt Institute of Chemical Biology Richard Armstrong Prize for Research Excellence. Vanderbilt Institute of Chemical Biology Student Research Symposium. Nashville, TN. August 2021.

Investigating Protein Quality Control Mechanisms of Thyroglobulin Folding and Secretion - Poster. Cold Spring Harbor: Protein Homeostasis in Health and Disease. Cold Spring Harbor, New York. November 2020.\*

Thyroglobulin interactome profiling defines altered proteostasis topology associated with thyroid dysmorphogenesis – Invited Oral. Sanford Burnham Prebys Medical Discovery Institute - ER Stress Club. Virtual Meeting. October 2020.

Thyroglobulin interactome profiling defines altered proteostasis topology associated with thyroid dysgenesis – Poster (3<sup>rd</sup> Place Poster Presentation). National Organization for the Professional Advancement of Black Chemist and Chemical Engineers (NOBCChE) Annual Conference. Orlando, FL. September 2020.\*

Investigating Protein Quality Control Mechanisms of an Endocrine Protein Misfolding Disorder – Poster. United States Human Proteome Organization Annual Conference. Seattle, Washington. March 2020.\*\*

Insights into The Protein Quality Control Mechanisms Dictating Thyroglobulin Folding and Secretion – Invited Oral. Vanderbilt University Protein Trafficking Symposium 2020. Vanderbilt University. Nashville, Tennessee. March 2020.

Quantitative Interactome Proteomics Reveals Proteostasis Network Remodeling Dictating Thyroglobulin Secretion – Poster. Vanderbilt Institute of Chemical Biology Student Research Symposium. Nashville, TN. August 2019.

Thyroglobulin as a model for analysis of protein quality control dynamics – Poster. 67<sup>th</sup> American Society for Mass Spectrometry Conference on Mass Spectrometry and Allied Topics. Atlanta, Georgia. June 2019.

Quantitative interactomics to determine protein quality control mechanisms dictating thyroglobulin secretion – Poster. 15<sup>th</sup> Annual United States Human Proteome Organization Conference. Rockville, Maryland. March 2019.

Expression and Functional Role of Collagen Modifying Enzyme P4HA1 in Colon Adenocarcinoma – Poster (1<sup>st</sup> Place Poster Presentation). – Partnership Research Summer Training Program Symposium. Atlanta, GA. July 2016.

\* - conference held virtually due to COVID19 pandemic

\*\* - conference cancelled due to COVID19 pandemic

## **Publications**

Munden, A., **Wright, MT.**, Han, D., Tirgar, R., Plate, L., Nordman, JT. Identification of replisome-associated proteins in *Drosophila* embryos and cultured cells using iPOND coupled to quantitative mass spectrometry. *Scientific Reports*. 2022.

DOI:10.1038/s41598-022-10821-9

Medinas, D., Malik, S., Yildiz-Bölükbaşı, E., Borgonovo, J., Saaranen, M., Urra, H., Pulgar, E., Afzal, M., Contreras, D., **Wright, MT.**, Bodaleo, F., Quiroz, G., Rozas, P., Mumtaz, S., Díaz, R., Rozas, C., Cabral-Miranda, F., Piña, R., Valenzuela, V., Uyan, O., Reardon, C., Woehlbier, U., Brown, R., Sena-Esteves, M., Gonzalez-Billault, Bernardo Morales, C., Plate, L., Ruddock, L., Concha, M., Hetz, C., & Tolun, A. Mutations in PDIA3 links altered ER proteostasis to neurodevelopmental impairment. *The EMBO Journal*. 2021, e105531. DOI: 10.15252/embj.2020105531

Reisman, BJ., Guo, H., Ramsey, HE., **Wright, MT.**, Reinfeld, BI., Ferrell, PB., Sulikowski, GA., Rathmell, WK., Savona, MR., Plate, L., Rubinstein, JL., Bachmann, BO. A Family of Glycosylated Macrolides Selectively Target Energetic Vulnerabilities in Leukemia. *Nature Chemical Biology*. 2021. DOI: 10.1038/s41589-021-00900-9.

Marinko, JT., **Wright, MT.**, Heintzman, DR., Plate, L., & Sanders, CR. Glycosylation limits forward trafficking of the tetraspan membrane protein PMP22. *Journal of Biological Chemistry*. 2021, 296, 100719. DOI: 10.1016/j.jbc.2021.100719.

**Wright, MT.**, & Plate, L. Revealing Functional Insights into ER Proteostasis through Proteomics and Interactomics. *Experimental Cell Research*. 2021, 399(1). DOI: 10.1016/j.yexcr.2020.112417 \*Invited Review Article\*

Rozas, P., Pinto, C., Traub, FM., Díaz, R., Pérez, V., Becerra, D., Ojeda, J., **Wright, MT.**, Mella, J., Plate, L., Henriquez, JP., Medinas, DB., & Hetz, C. Protein disulfide isomerase ERp57 protects early muscle denervation in experimental ALS. *Acta Neuropathologica Communications*. 2021, 9(21). DOI: 10.1186/s40478-020-01116-z

**Wright, MT.**, Kouba, L., & Plate, L. Thyroglobulin interactome profiling defines altered proteostasis topology associated with thyroid dysmorphogenesis. *Molecular & Cellular Proteomics*. 2021, 20, 100008. DOI: 10.1074/mcp.RA120.002168